RADIATION PRESSURE COOLING OF A SILICA OPTOMECHANICAL RESONATOR

by

YOUNG-SHIN PARK

A DISSERTATION

Presented to the Department of Physics
and the Graduate School of the University of Oregon
in partial fulfillment of the requirements
for the degree of
Doctor of Philosophy

December 2009

University of Oregon Graduate School

Confirmation of Approval and Acceptance of Dissertation prepared by:

Young-Shin Park

Title:

"Radiation Pressure Cooling of a Silica Optomechanical Resonator"

This dissertation has been accepted and approved in partial fulfillment of the requirements for the Doctor of Philosophy degree in the Department of Physics by:

Michael Raymer, Chairperson, Physics
Jens Noeckel, Member, Physics
Hailin Wang, Member, Physics
Paul Csonka, Member, Physics
Jeffrey Cina, Outside Member, Chemistry

and Richard Linton, Vice President for Research and Graduate Studies/Dean of the Graduate School for the University of Oregon.

December 12, 2009

Original approval signatures are on file with the Graduate School and the University of Oregon Libraries.

An Abstract of the Dissertation of

Young-Shin Park for the degree of Doctor of Philosophy
in the Department of Physics to be taken December 2009

Title: RADIATION PRESSURE COOLING OF A SILICA
OPTOMECHANICAL RESONATOR

Approved: ______________________________
Dr. Hailin Wang, Adviser

This dissertation presents experimental and theoretical studies of radiation pressure cooling in silica optomechanical microresonators where whispering gallery modes (WGMs) are coupled to thermal mechanical vibrations. In an optomechanical system, circulating optical fields couple to mechanical vibrations via radiation pressure, inducing Stokes and anti-Stokes scattering of photons. In analogy to laser cooling of trapped ions, the mechanical motion can in principle be cooled to its ground state via the anti-Stokes process in the resolved-sideband limit, in which the cavity photon lifetime far exceeds the mechanical oscillation period.

Our optomechanical system is a slightly deformed silica microsphere (with a diameter $25 - 30\ \mu m$), featuring extremely high Q-factors for both optical ($Q_o \sim 10^8$) and mechanical ($Q_m \sim 10^4$) systems. Exploiting the unique property of directional evanescent escape in the deformed resonator, we have developed a free-space configuration for the excitation of WGMs and for the interferometric detection of mechanical displacement, for which the part of input laser that is not coupled into the microsphere serves as a local oscillator. Measurement sensitivity better than $5 \times 10^{-18} m/\sqrt{\text{Hz}}$ has been achieved. The three optically active mechanical modes observed in the displacement power spectrum are well described by finite element analysis.

Both radiation pressure cooling and parametric instabilities have been observed in our experiments. The dependence of the mechanical resonator frequency and linewidth on the detuning as well as the intensity of the input laser show excellent agreement with theoretical calculations with no adjustable parameters.

The free-space excitation technique has enabled us to combine resolved sideband cooling with cryogenic cooling. At a cryogenic temperature of 1.4 K, the sideband cooling leads to an effective temperature as low as 210 mK for a 110 MHz mechanical oscillator, corresponding to an average phonon occupation of 37, which is one of the three lowest phonon occupations achieved thus far for optomechanical systems. The cooling process is limited by ultrasonic attenuation in fused silica, which should diminish when bath temperature is further lowered, with a ^{3}He cryostat, to a few hundred millikelvin. Our experimental studies thus indicate that we are tantalizingly close to realizing the ground-state cooling for the exploration of quantum effects in an otherwise macroscopic mechanical system.

CURRICULUM VITAE

NAME OF AUTHOR: Young-Shin Park

PLACE OF BIRTH: Seoul, Republic of Korea

DATE OF BIRTH: September 19, 1972

GRADUATE AND UNDERGRADUATE SCHOOLS ATTENDED:

University of Oregon

Seoul National University

DEGREES AWARDED:

Doctor of Philosophy in Physics, 2009, University of Oregon

Master of Science in Physics, 1998, Seoul National University

Bachelor of Science in Physics Education, 1996, Seoul National University

ACADEMIC INTERESTS

Quantum Optics of Optomechanical Systems

Cavity Quantum Electrodynamics

Applications of Silica Microsphere Resonators

PROFESSIONAL EXPERIENCE:

Research Assistant, Department of Physics,
University of Oregon, Eugene, Oregon, 2003-2009

Teaching Assistant, Department of Physics,
University of Oregon, Eugene, Oregon, 2002-2009

Instructor, Department of Physics,
Rep. of Korea AirForce Academy, Chungbuk, Rep. of Korea, 1999-2002

Research/Teaching Assistant, Department of Physics,
Seoul National University, Seoul, Rep. of Korea, 1996-1998

GRANTS, AWARDS AND HONORS:

Fundamental Optical Processes in Semiconductors, Student Travel Grant, 2007

First Prize Winner in Ph.D. Qualification Exam, 2003

First Prize Winner in Master's Degree Qualification Exam, 2003

Obtained a Teacher's Certificate (Physics) from Ministry of Education & Human Resource Development, Rep. of Korea, 1996

Merit-Based Scholarships for all semesters in undergraduate school, Seoul National University, Rep. of Korea, 1992-1995

PUBLICATIONS:

Y.-S. Park and H. Wang, "Resolved-sideband and cryogenic cooling of an optomechanical resonator," Nature Phys. **5**, 489 (2009).

Y.-S. Park and H. Wang, "Radiation pressure driven mechanical oscillation in deformed silica microspheres via free-space evanescent excitation," Opt. Express **15**, 16471 (2007).

Y.-S. Park and H. Wang, "Regenerative pulsation in silica microspheres," Opt. Lett. **32**, 3104 (2007).

Y.F. Xiao, C.H. Dong, Z.F. Han, G.C. Guo, and Y.-S. Park, "Directional escape from a high-Q deformed microsphere induced by short CO2 laser pulses," Opt. Lett. **32**, 644 (2007).

Y.-S. Park, A. Cook, and H. Wang, "Cavity QED with Diamond Nanocrystals and Silica Microspheres," Nano Lett. **6**, 2075 (2006).

S. Tavenner-Kruger, Y.-S. Park, M. Lonergan, U. Woogon, and H. Wang, "Zero-Phonon Linewidth in CdSe/ZnS Core/Shell Nanorods," Nano Lett. **6**, 2154 (2006).

Y.-S. Park, Y.C. Noh, W.K. Lee, J.H. Lee, and J.S. Change, "Transverse spatial beam patterns spontaneously formed in the feedback system with a liquid crystal," J. Opt. Soc. Kor. **3**, 15 (1999).

ACKNOWLEDGMENTS

I would like to thank my adviser, Hailin Wang, for his guidance, support and encouragement throughout my doctoral research period. I believe that his critical insight into physics and his optimistic enthusiasm for pursuing the frontier of physics are most valuable lessons and will continue to guide me.

I would like to thank Dr. Michael Raymer, Dr. Jens Nöckel, Dr. Jeffrey Cina and Dr. Paul Csonka for their support on my doctoral research.

I express my gratitude to Kris Johnson. Without his expertise in cryogenic systems, I wouldn't have competed my experimental studies in time.

I give my sincere thanks to all my colleagues old and new in the Wang lab who gave me generous helps. I especially and deeply thank my former officemate Shannon. I also thank Nima, Carey and Tim not only for helping me with transferring liquid helium, but also for cheering me up in frustrating moments. I also appreciate Susanta, Yumin, Yan, Sasha, and Tao. I wish best of luck to all of you.

I also express my thanks to OCO and Physics Administration, especially Bonnie, Patty, Jani, and Brandy.

I thank Jinwoo, Jinsoo, and Gwangrim and their families, who made a life being a Ph.D in Eugene more richer and enjoyable.

I thank my mother and my brother in Korea for their constant love and encouragement.

And I always thank my wife Kyunghee for her endless support and love, and thank my son Yeanwoo for his ingenuous smile.

TABLE OF CONTENTS

Chapter Page

I INTRODUCTION 1

1.1 Laser Cooling of Atoms 1
1.2 Cooling of a Macroscopic Object 3
1.3 Overview of the Dissertation 13

II SILICA MICROSPHERE OPTOMECHANICAL RESONATORS 15

2.1 Whispering Gallery Modes in Silica Microspheres 17
2.2 Mechanical Vibration Modes of Silica Microspheres 23
2.3 Finite Element Analysis of a Microsphere-Stem System 25
2.4 Effective Mass 29

III THEORETICAL BACKGROUND OF OPTOMECHANICAL COOLING 32

3.1 1D Harmonic Oscillator in Thermal Equilibrium 34
3.2 Equipartition Theorem 35
3.3 Classical Theory of Optomechanical Cooling in a Microsphere . . 36
3.4 Quantum Mechanical Description of Optomechanical Cooling . . 43
3.5 Resolved-Sideband Cooling 46

IV EXPERIMENTAL TECHNIQUES AND CHARACTERIZATION . . . 49

4.1 Free-Space Excitation of WGMs 51
4.2 Homodyne Interferometric Detection of Mechanical Vibrations . . 65
4.3 Observations of Optomechanical Coupling 79
4.4 Mechanical Quality Factors 85

V OPTICAL BISTABILITY OF WGMS AT LOW TEMPERATURE . . . 93

5.1 Thermal Bistability of WGMs in a Silica Microsphere 94
5.2 Regenerative Pulsation 97

Chapter | Page

VI RESOLVED-SIDEBAND COOLING OF A SILICA MICROSPHERE 103

6.1 Resolved-Sideband Cooling at Room Temperature 104
6.2 Cryogenic Precooling 106
6.3 Resolved-Sideband Cooling at Cryogenic Temperature 108
6.4 Discussion of Cooling Limit 113

VII SUMMARY AND FUTURE WORK 115

7.1 Dissertation Summary 115
7.2 Future Work 118

BIBLIOGRAPHY 121

LIST OF FIGURES

Figure Page

1.1 Schematic of the resolved-sideband cooling of a trapped ion and the Doppler cooling of an atom 2
1.2 Temperature dependence of phonon occupation 5
1.3 Illustration of optomechanical coupling 7
1.4 Optomechanical parametric process 10
1.5 Schematic of resolved-sideband cooling 11

2.1 Total internal reflection in a microsphere resonator 16
2.2 Effective potential of WGM 20
2.3 Spheroidal vibration modes of a silica microsphere 25
2.4 Finite element simulation of mechanical vibration modes 27
2.5 Degeneracy of the $(1, 2)$ mechanical vibration mode 28
2.6 Effective mass coefficient for the $(1, 0)$ and $(1, 2)$ radial breathing modes simulated with finite element analysis 30

3.1 One-dimensional harmonic oscillator 33
3.2 Radiation pressure force in a microsphere 37
3.3 Theoretical calculations of the effective linewidth and frequency 40
3.4 Input power dependence of the effective linewidth and frequency 42
3.5 Schematic of the displacement spectrum upon cooling or heating 44
3.6 Average phonon occupation achievable by radiation pressure cooling . . 47

4.1 Excitation of the WGM in a microsphere 52
4.2 Scanning electron microscope images of a deformed microsphere 54
4.3 Experimental setup 56
4.4 Free-space evanescent excitation of the WGM 59
4.5 Transmission spectrum via free-space excitation 60
4.6 WGM structure of a deformed microsphere 62
4.7 Fabrication of a deformed microsphere 64
4.8 Schematic of homodyne detection in free-space excitation 66
4.9 Theoretical calculations of the AC amplitude 70
4.10 Power spectrum of optical transmission 72
4.11 Size dependence of the mechanical vibrations 73
4.12 Homodyne detection in free-space excitation 74

Figure Page

4.13 Theoretic calculation of AC amplitude normalized to the input power for phase-modulated excitation 78
4.14 Calibration of mechanical displacement 80
4.15 Measured optical transmission spectra for red and blue detuning 81
4.16 Power dependence of the measured effective linewidth 83
4.17 Measured parametric oscillation of mechanical vibration 84
4.18 Measured high mechanical quality factor 87
4.19 The effects of a fiber stem on the mechanical quality factor 88
4.20 Deformation dependence of the mechanical quality factor 89
4.21 Measured mechanical linewidth of a $(1, 2)$ vibration mode as a function of bath temperature 91

5.1 Thermal bistability of a WGM resonance 95
5.2 Solid squares show the relative frequency of a WGM resonance as a function of temperature 96
5.3 Optical transmission as a function of time at $T = 18.5$ K 98
5.4 Schematic illustration of regenerative pulsation 100

6.1 Resolved-sideband cooling at room temperature 106
6.2 Measured mechanical frequency and mechanical quality factor of a $(1, 2)$ vibration mode as a function of bath temperature 108
6.3 Displacement spectrum obtained at $T_{bath} = 20$ K 109
6.4 Resolved-sideband cooling at cryogenic temperature 110
6.5 Spectrally integrated area of the $(1, 2)$ mode 112

7.1 A mechanical oscillation coupled to a spin excitation 120

CHAPTER I

INTRODUCTION

Optomechanical cooling of a microresonator has recently attracted a great deal of attention in the optics community because it can provide a promising avenue to cool a macroscopic mechanical oscillator to its quantum ground state. In an analogue to laser trapping or cooling of an ion, in optomechanical cooling the mechanical energy of a macroscopic oscillator is extracted through the viscous radiation pressure force when the laser beam is red-detuned from the cavity resonance by the oscillator's vibration frequency. However, instead of cooling a single atom, the radiation pressure in a microresonator cools the collective vibrational motion of the macroscopic oscillator, which consists of much more than 10^{10} atoms. The ability to reach the quantum ground state of a macroscopic oscillator enables us to explore the quantum nature of an otherwise classical system.

1.1 Laser Cooling of Atoms

Laser cooling of ions and atoms is a powerful and well-established technique in atomic physics [1–3]. For an ion trapped in a harmonic potential, a photon can couple to the mechanical motion of the ion through Stokes as well as anti-Stokes processes, as illustrated in Fig. 1.1(a). The anti-Stokes process leads to the absorption

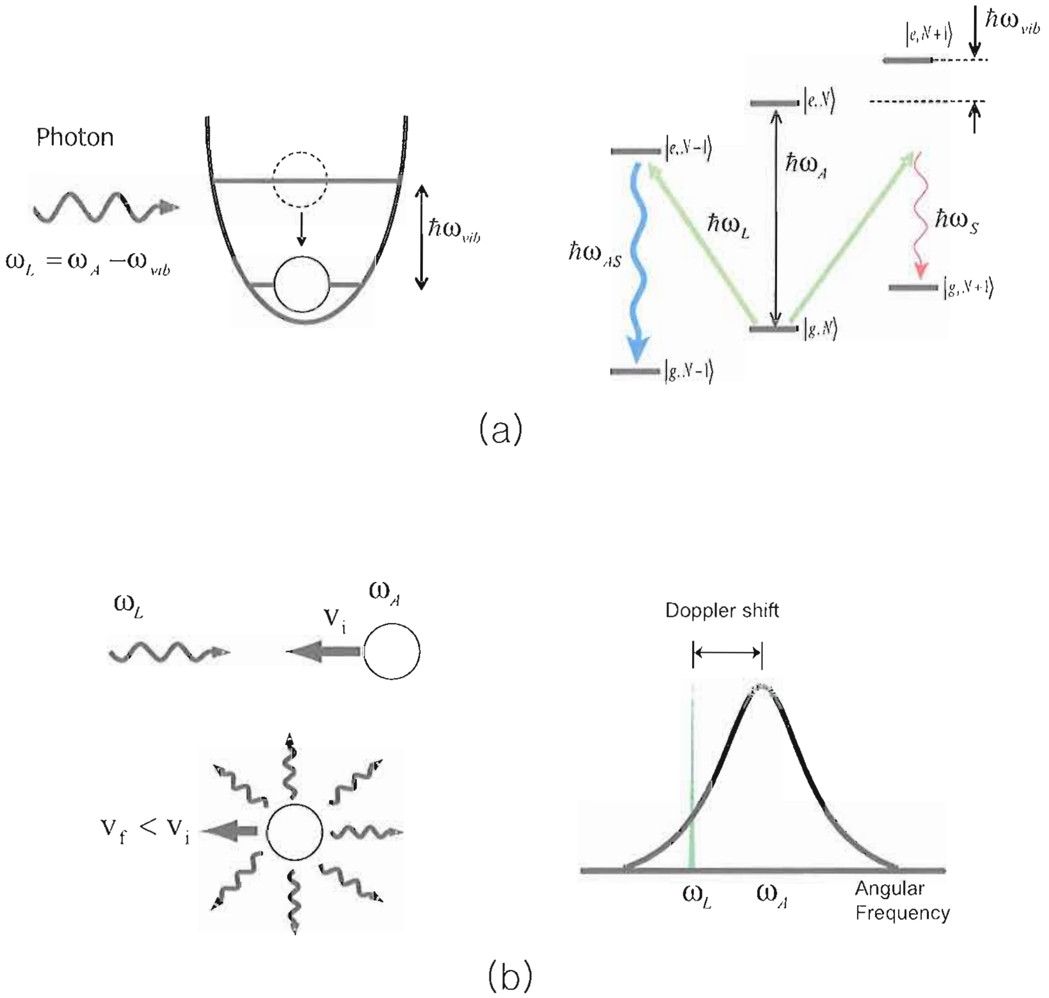
Photon
ω_L = ω_A − ω_vib
ħω_vib
|e,N+1⟩
ħω_vib
|e,N⟩
|e,N−1⟩
ħω_A
ħω_L
ħω_S
ħω_AS
|g,N+1⟩
|g,N⟩
|g,N−1⟩
(a)
ω_L
ω_A
V_i
V_f < V_i
Doppler shift
ω_L
ω_A
Angular Frequency
(b)

Figure 1.1: Schematic of (a) the resolved-sideband cooling of a trapped ion and (b) the Doppler cooling of an atom. In (a), the phonon occupation of the ion's vibration motion is lowered by the resonant anti-Stokes process with negligible Stokes process when $\omega_L = \omega_A - \omega_{vib}$, in the limit where ω_{vib} is larger than the atomic transition linewidth. In (b), the net momentum transfer involved in the photon absorption followed by spontaneous emission results in the slowdown of the atomic motion. In this case, the laser is red-detuned in order to compensate the blue Doppler shift seen by the moving atom. ω_{vib}, ω_L and ω_A are the angular frequency of the phonon, the laser and the atomic transition, respectively. $|g(e), N\rangle = |ground\ state(excited\ state), phonon\rangle$

of phonons and cools down the mechanical motion of the ion, while the Stokes process leads to the emission of phonons and amplifies the mechanical motion of the ion. In the resolved-sideband limit, the mechanical (or phonon) frequency is large compared with the optical transition linewidth. As a result, the resonant anti-Stokes process can take place with negligible contribution from the Stokes process. In this limit, the anti-Stokes process can in principle cool the trapped ion to its motional ground state.

For Doppler cooling of neutral atoms, a laser beam is slightly red-detuned from the incoming atoms. Optical absorption followed by spontaneous emission along a random direction damps the atomic motion and leads to a viscous radiation pressure force, as illustrated in Fig. 1.1(b). Here, the red detuning compensates for the blue Doppler shift experienced by the atom.

After theoretical predictions of Doppler cooling in 1975 [4, 5], the radiation pressure cooling of Mg^+ ions to the effective temperature of < 40 K was first demonstrated in 1978 by D. Wineland [6], followed by the laser deceleration of Na atoms in 1982 by W. Phillips [7]. By combining three pairs of counterpropagating lasers in three orthogonal directions, a number of ions were cooled, and at the same time, trapped in small region [8, 9]. This is so called Optical Molasses. Cooling below the single photon recoil, the Doppler cooling limit, was also demonstrated in 1988 by achieving $\sim 2\ \mu$K for He atoms [10, 11]. In 1989 by F. Diedrich, through the resolved-sideband cooling scheme, a single Hg^+ ion initially trapped in potential well was cooled to the ground state, approximately 95 % of the time [12].

1.2 Cooling of a Macroscopic Object

The idea of cooling a macroscopic object originates from the issue of thermal noise at the laser interferometer gravitational wave observatory (LIGO). Gravitational wave predicted by A. Einstein in his theory of general relativity has long been sought, but not observed yet. For the detection of this extremely weak signal, a lot of effort has been made in order to improve the measurement sensitivity. One of the major obstacles is the thermal vibrations, or Brownian motion, of the mirrors that constitute the laser interferometer [13, 14]. These thermal mechanical fluctuations induce a random noise in the phase sensitive measurement, obscuring the signal of the gravitational wave. As predicted by Braginsky [15], the circulating laser power can induce the parametric instability in the thermal motion of the laser mirrors. Because the measurement noise comes from the thermal motion, one straightforward solution to this issue will be the cooling of the entire mechanical components of the LIGO system [16].

Not only for its applications to the ultrasensitive measurement in force and displacement [17], the cooling of macroscopic objects is intrinsically attractive also for the fundamental studies in a new quantum system, a macroscopic quantum state, that has never been explored before. The interesting, but challenging topics include, for examples, the quantum mechanical entanglement between a mirror and single photons [18, 19], the transition in the boundary between quantum and classical mechanics and cavity quantum optomechanics [20–22].

The final average phonon occupation number depends not only on the bath temperature, but also the mechanical vibration frequency as shown in Fig. 1.2. With an assumption of a bosonic behavior of phonons, when a mechanical oscillator is in thermal equilibrium at temperature T, the average phonon occupation, $\langle N \rangle$ is given by,

$$\langle N \rangle = \frac{1}{e^{\hbar\omega_m/k_B T} - 1} \tag{1.1}$$

where $\hbar$ and k_B are the Planck constant and the Boltzmann constant, respectively, and

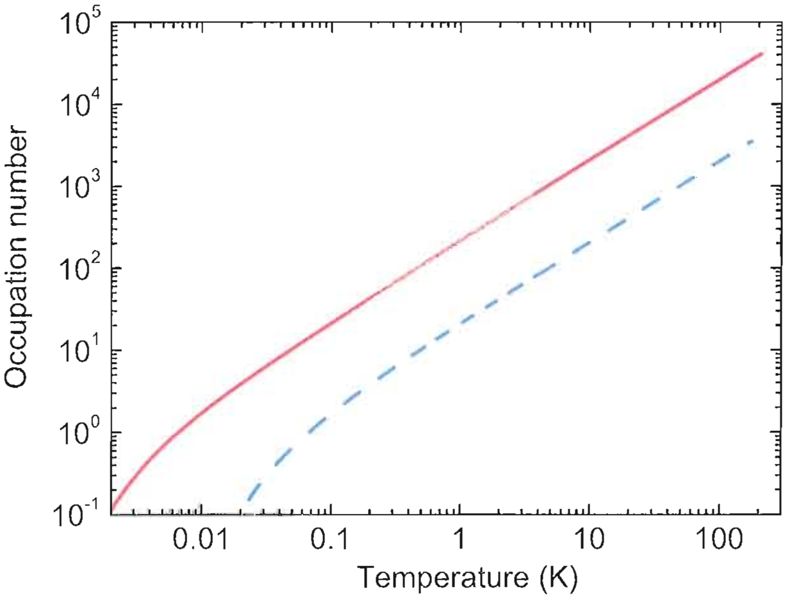

Figure 1.2: Temperature dependence of average phonon occupation number of a mechanical oscillator for 100 MHz in red solid curve and 1 GHz in blue dashed curve.

$\omega_m/2\pi$ is the mechanical vibration frequency. Figure 1.2 shows the average phonon occupation as a function of temperature for two different oscillator frequencies. If $k_BT \gg \hbar\omega_m$, the average phonon occupation yields to the classical limit, $\langle N\rangle \simeq k_BT/\hbar\omega_m$, which is proportional to the temperature as expected from the equipartition theorem. If $k_BT \ll \hbar\omega_m$, $\langle N\rangle$ approached to 0, indicating the quantum ground state. The temperatures for $\langle N\rangle = 1$ are approximately 9 mK for a 100 MHz vibration and 90 mK for a 1 GHz vibration, respectively.

The cooling of macroscopic objects has been intensively pursued in two different directions; Cryogenic cooling of nano- or micro-electromechanical system (MEMS or NEMS) [17, 23] and the optomechanical cooling of a microresonator [20–22]. In the former case, the entire mechanical oscillator is cooled in a cryogenic chamber, such as a dilute gas refrigerator. Therefore, in thermal equilibrium with the bath temperature, the final temperature and the corresponding phonon occupation of the mechanical oscillator are determined by bath temperature, but cannot go further below. From cryogenic cooling of a 21.8 MHz nanomechanical oscillator, a phonon occupation as low as 25 was observed at $\sim 50\ m$K bath temperature [24]. The design and the fabrication of mechanical oscillators with a frequency above GHz could lead to the quantum ground state within temperatures available in current cryogenic systems. On the other hand, the optomechanical cooling utilizes the dynamical backaction of the radiation pressure force, which can either damp or heat the resonator's thermal motion, depending on the laser detuning. In this case, the temperature of a mechanical oscillator is effectively lowered from bath temperature while increasing the circulating power. In radiation pressure cooling, only a particular vibration mode is selectively cooled due to the resonant mechanism in optomechanical cooling.

In order to see how optomechanical cooling works in a microresonator, consider a Fabry-Perot resonator consisting of two end mirrors. We assume that one end mirror is not movable while the other mirror is allowed to vibrate. As shown in Fig. 1.3(a), this mirror's vibration can be modeled as a simple harmonic oscillator with an effective mass m. A real mirror has a number of vibration modes with discrete eigenfrequencies, but for simplicity, we consider only a single vibrational frequency, $\omega_m/2\pi$. This assumption is reasonable as long as the coupling between the different mechanical vibration modes is negligible for high mechanical quality factors, or small damping rates. The effective mass is defined by accounting optomechanical coupling, i.e. the changes in the optical path length induced by the mechanical vibrations [14, 25]. Thus, each vibration mode has a different effective mass [26].

The cavity round trip length determines the resonant condition for the optical modes in a microresonator at a given frequency. The mechanical vibration of an end mirror directly changes this resonance condition, leading to an oscillation of the optical resonances with a vibration frequency and in turn a modulation of the

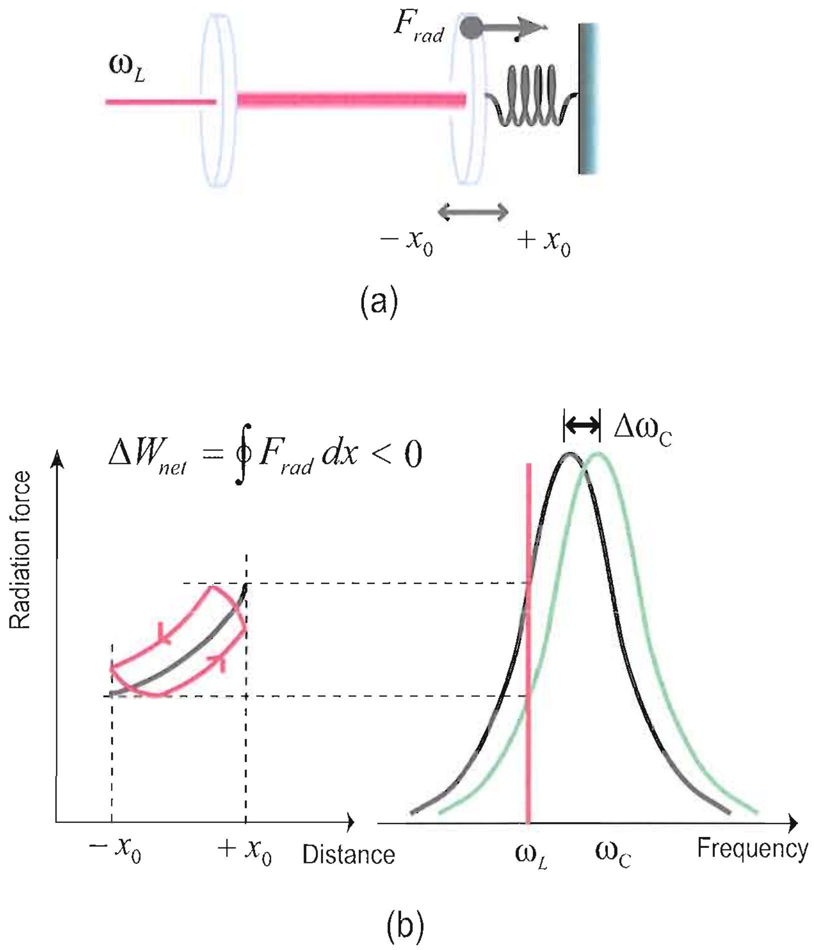
F_{rad}
ω_L
$-x_0$
$+x_0$
(a)
$\Delta W_{net} = \oint F_{rad}\, dx < 0$
$\Delta\omega_C$
Radiation force
$-x_0$
$+x_0$
Distance
ω_L
ω_C
Frequency
(b)

Figure 1.3: Illustration of optomechanical coupling in terms of energy exchange. (a) One end mirror in Fabry-Perot resonator is modeled as a mechanical oscillator with $\omega_m/2\pi$ (b) A force-distance diagram of one end mirror. The path integral gives the net work done by the radiation pressure force on the mirror. For red detuning ($\omega_L - \omega_c < 0$), the net work can be negative, meaning the cooling of the mechanical motion as denoted in a red line. ω_L and ω_c are the angular frequency of the excitation laser and the cavity resonance, respectively.

intracavity power. The shift in the optical resonance frequency, $\Delta\omega_c$, is,

$$\Delta\omega_c = -\frac{x}{L}\omega_c \tag{1.2}$$

where x is the vibration amplitude and L is the cavity length, which corresponds to the radius for a microsphere resonator. For a 30 μm microsphere with an optical Q-factor of $\sim 10^7$, the resonance frequency shift by the mechanical vibration is approximately 0.4 MHz, which induces about one percent of circulating power modulation with a laser detuned on the half maximum. The radiation pressure force arising from the reflections of single photons at the end mirror is proportional to the intracavity power. Therefore, the modulation of the intracavity power directly leads to the change in the radiation pressure force.

The build-up or decay time of the intracavity field is not instantaneous, but finite due to the cavity loss. This fact makes the effect of radiation pressure force on the vibrating mirror more dramatic. Consider a force-displacement diagram of a mirror's motion in Fig. 1.3(b), provided a laser is detuned on the red side of cavity resonance. In the case where the cavity lifetime is shorter than the vibration period, the position-dependent radiation pressure force immediately changes along with the mirror's position. In this adiabatic limit, the radiation force and the position are nearly in phase. The integral over the adiabatic path denoted in a black line implies that the net work done by the radiation pressure on the mirror per cycle is equal to zero, meaning no optomechanical energy transfer. However, when the cavity lifetime is comparable to or longer than the vibration period, the radiation pressure force is not instantaneous, but delayed with respect to the mirror's motion. In this limit, $\omega_m \geq \kappa$, the radiation force and the mirror's position are no longer in phase. This delayed response of radiation pressure force is drawn in the force-displacement diagram, showing a counterclockwise loop in a red line in Fig. 1.3(b). The path integral over the red loop leads to the negative net work, and the mechanical vibration energy is lowered, indicating the cooling of the mechanical motion. In contrast, for blue detuning, the path integral leads to the positive net work, indicating an increase in the mechanical energy, the heating of the mechanical motion. In this way, the optomechanical coupling can either cool or enhance the mechanical motion of the mirror, depending on the laser detuning.

The cooling and heating of the mechanical vibration of a microresonator can be also understood by an optomechanical parametric process that generates Stokes ($\omega_S = \omega_L - \omega_m$) and anti-Stokes photons ($\omega_{AS} = \omega_L + \omega_m$) into the relevant cavity mode as shown in Fig. 1.4. Each Stokes process increases the mechanical energy by $\hbar\omega_m$, while each anti-Stokes process decreases the mechanical energy by $\hbar\omega_m$. The optomechanical coupling intrinsically induces both the Stokes and the anti-Stokes photons, but the rates of each process strongly depend on the laser detuning. For red detuning, the Stokes is dominant because it is close to the optical resonance. In contrast, the anti-Stokes is dominant for blue detuning. Optimal cooling or heating is obtained by adjusting the laser detuning such that the anti-Stokes or the Stokes falls exactly onto the cavity resonance.

The resolved-sideband scheme used to cool a trapped ion can be adapted for the cooling of the mechanical vibration of a microresonator [27]. As explained in optomechanical parametric process, the net cooling rate is determined by the difference between the anti-Stokes (cooling) and the Stokes (heating) processes. Suppose the laser is detuned such that the anti-Stokes emission is on the cavity resonance as depicted in Fig. 1.5. In the adiabatic limit $\omega_m \ll \kappa$ as in Fig. 1.5(a), the residual Stokes emission contributes to reduce the cooling rate induced by the anti-Stokes process. However, in the resolved-sideband limit $\omega_m \gg \kappa$ as in Fig. 1.5(b),

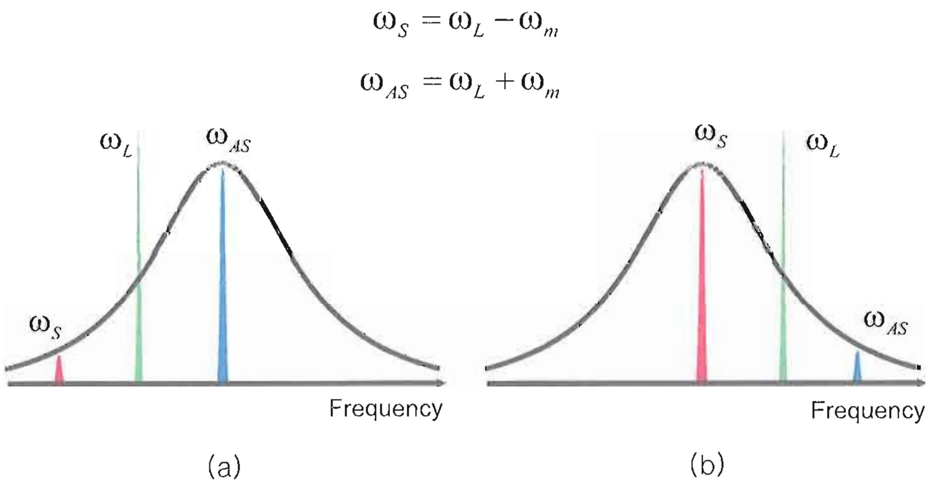

(a) (b)

Figure 1.4: Optomechanical parametric process generates the Stokes $\omega_s = \omega_L - \omega_m$ and the anti-Stokes $\omega_{as} = \omega_L + \omega_m$ where ω_L is an angular laser frequency. Depending on the laser detuning, the asymmetry of the Stokes and the anti-Stokes leads to (a) the cooling and (b) the heating of mechanical vibrations.

the Stokes emission is profoundly suppressed, while the anti-Stokes emission is still resonantly enhanced. In this limit, the radiation pressure cooling will be more efficient.

In addition, the quantum theory of the optomechanical cooling addresses the importance of the resolved-sideband condition of the optomechanical system. The radiation pressure cooling, which increases with increasing the intracavity intensity, will be eventually limited by the random fluctuation of the intracavity intensity, i.e. the shot noise. However, in the resolved-sideband limit, the heating due to the fluctuation of the radiation pressure force can be significantly reduced because the laser is detuned far away from the cavity resonance. Theoretical work predicts that the ground-state cooling is, in principle, possible in this limit [28–30].

Radiation pressure cooling was first demonstrated in 1999 by P. Cohadon in an active feedback system of controlling the thermal motion, showing about 20 times reduction in the vibration amplitude of an end mirror in a Fabry-Perot cavity [31].

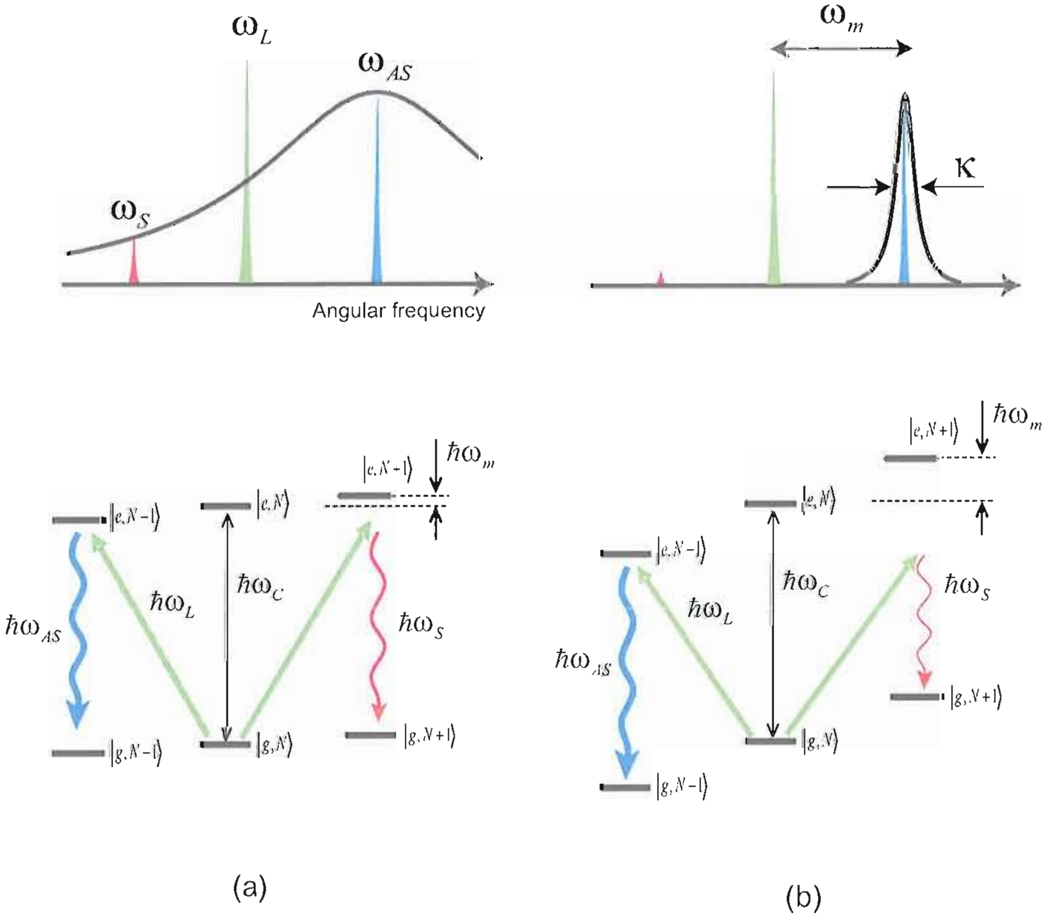
ω_L
ω_AS
ω_S
Angular frequency
ω_m
κ
|e,N-1⟩
|e,N⟩
|e,N-1⟩
ħω_m
ħω_L
ħω_C
ħω_AS
ħω_S
|g,N-1⟩
|g,N⟩
|g,N+1⟩
|e,N+1⟩
ħω_m
|e,N⟩
|e,N-1⟩
ħω_L
ħω_C
ħω_S
ħω_AS
|g,N+1⟩
|g,N⟩
|g,N-1⟩
(a)
(b)

Figure 1.5: Schematic of optomechanical cooling and the energy diagram in (a) the adiabatic limit $\omega_m \ll \kappa$ and in (b) the resolved-sideband limit $\omega_m \gg \kappa$, where ω_m and κ are angular frequencies of the mechanical vibration and the cavity linewidth, respectively. The cooling laser is detuned such that the anti-Stokes falls exactly on the cavity resonance. In the resolved-sideband limit, the Stokes is profoundly suppressed, leading to the significant reduction in the phonon occupation. $|g(e), N\rangle$ denotes the energy level where N is a phonon occupation, and g and e mean no-excitation and excitation of the cavity mode, respectively.

Self-cooling and self-heating of a cantilever by the delayed bolometric force was demonstrated [32], proving the key role of dynamical backaction on the optomechanical cooling. The dynamical backaction cooling of the radiation pressure force was realized in several types of optomechanical systems [33–36]. Significant suppression of the thermal vibration motion of a microresonator leads to the effective temperature as low as sub-Kelvin. Optomechanical cooling experiments have been also carried out at low temperature [37–39], demonstrating the effective temperature in the range of milli-Kelvin for a 3.8 kHz mechanical oscillator [37]. Reminding of the frequency dependence of the average phonon occupation, in spite of the considerable reduction in the effective temperature, the average phonon occupation numbers that have been attained thus far, however, still remain above $1,000$.

Resolved-sideband cooling was also demonstrated in a silica microresonator with a high optical finesse, achieving $\langle N \rangle \sim 4,000$ at room temperature [27]. The resolved-sideband cooling can be combined with the cryogenic precooling to lower the thermal dissipation determined by the bath temperature. In this case, the challenges and technical difficulties lie not only in the implementation and the control of a high finesse optical resonator in a cryogenic environment [40], but also in achieving an extremely high measurement sensitivity [41]. Recently, experimental studies of the resolved-sideband and cryogenic cooling from three different groups [42–44], including our silica microsphere optomechanical resonator, have achieved the average phonon occupation below 60. These results indicate that we are just a few steps away toward the ground-state cooling of an otherwise macroscopic mechanical system.

1.3 Overview of the Dissertation

This dissertation presents the experimental studies of radiation pressure cooling of a silica microresonator in a cryogenic environment. We begin with an introduction to the optical whispering gallery modes and the mechanical vibration modes in silica optomechanical microsphere resonator in Chapter II. The physical insight of ultrahigh Q-factor WGMs is discussed based on the effective radial potential as analogue to the one dimensional quantum well. We simulate the mechanical vibrations of a silica microsphere with finite element analysis, providing the eigenfrequencies along with the spatial shapes for each normal vibration mode. We show that the radial breathing mechanical modes, which induce changes in the cavity path length of a WGM, can be coupled with the WGM.

In Chapter III, we provide the theoretical background of the radiation pressure induced optomechanical cooling. Considering the Stokes and anti-Stokes fields in the parametric optomechanical process, we derive the analytic forms of the effective damping rates and the effective mechanical frequencies under the influence of the radiation pressure force. A quantum description of the optomechanical cooling is discussed to explain the ultimate limit of radiation pressure cooling. Ground-state cooling with the radiation pressure is in principle possible only in the resolved-sideband limit, where the cavity lifetime is longer than the mechanical vibration period.

We discuss the experimental techniques for the radiation pressure cooling in Chapter IV. By utilizing the directional escape in deformed microspheres, we are able to excite the WGMs in free space, demonstrating the transmission dip more than 50%. The free-space evanescent excitation scheme provides not only a convenient way to access a silica microresonator in a cryogenic environment, but also interferometric homodyne detection of the mechanical displacement with the measurement sensitivity below 5×10^{-18} $m/\sqrt{\text{Hz}}$. We show the experimental observations of the thermal mechanical vibration of silica microspheres, which show excellent agreements with the finite element analysis. Under the influence of the radiation pressure force, which is proportional to the circulation power, we observe also the significant heating and cooling of the mechanical vibration, including the parametric oscillation. The calibration of the observed mechanical displacement is performed with the phase modulated excitation laser, which mimics the phase shift induced by the mechanical vibrations.

Thermal bistability of the WGMs is studied both at room and low temperatures in Chapter VI. We observe the WGM resonance shift goes to zero near 20 K where the effect of the negative thermal expansion and the thermo-optic effect are canceled out. We also observe the pulsation in the optical transmission upon continuous laser input, which is attributed to the competition between the diminishing thermal effect and the Kerr effect.

In Chapter VII, we present the resolved-sideband cooling carried out at both room and cryogenic temperatures. At room temperature we achieve an effective temperature of 11 K, limited mainly by the thermal dissipation. As lowering the temperature, we first confirm the cryogenic precooling of a silica microsphere by observing the linear dependence of the spectral area on the bath temperature. At low temperature, we show the dependence of the mechanical vibration frequency and the mechanical linewidth on the detuning as well as the input power of the excitation laser, which show excellent agreements with the theoretical calculation. At 1.4 K bath temperature, we achieve an average phonon occupation as low as 37 for a 110 MHz mechanical vibration, which is limited by the ultrasonic attenuation of fused silica.

In Chapter VIII, we will provide an overall summary and the future work.

CHAPTER II

SILICA MICROSPHERE OPTOMECHANICAL RESONATORS

When light travels between two different media, the light is partially reflected and partially refracted at the boundary surface. If light crosses the boundary from a higher refractive index medium to a lower one, light will be totally reflected with no transmission when the angle of incidence is equal to or greater than a certain angle, called the critical angle. In a ring type dielectric resonator, such as a microsphere or a microtoroid, light can travel along the circumference by successive total internal reflections. When the round trip distance is an integer number of wavelengths in the resonator, a resonant optical mode is formed in the ring resonator (See Fig. 2.1). These modes are so called whispering gallery modes (WGMs), named after, the whispering gallery where a person standing near the wall can clearly hear whispering from the opposite side of the gallery since the sound can travel along the wall. The WGMs in optical resonators [45] were first experimentally observed in 1908 by G. Mie [46].

In fused silica microresonators, WGMs feature ultrahigh optical quality factors due to extremely high material purity and nanometer scale surface uniformity. Optical Q-factor as high as $\sim 0.8 \times 10^{10}$ was demonstrated in a 100 μm silica microsphere [47]. When the angle of incidence is close to 90 degrees, a WGM is tightly confined within a wavelength of the microsphere surface, and its volumes can be as small as $\sim 1/1000$

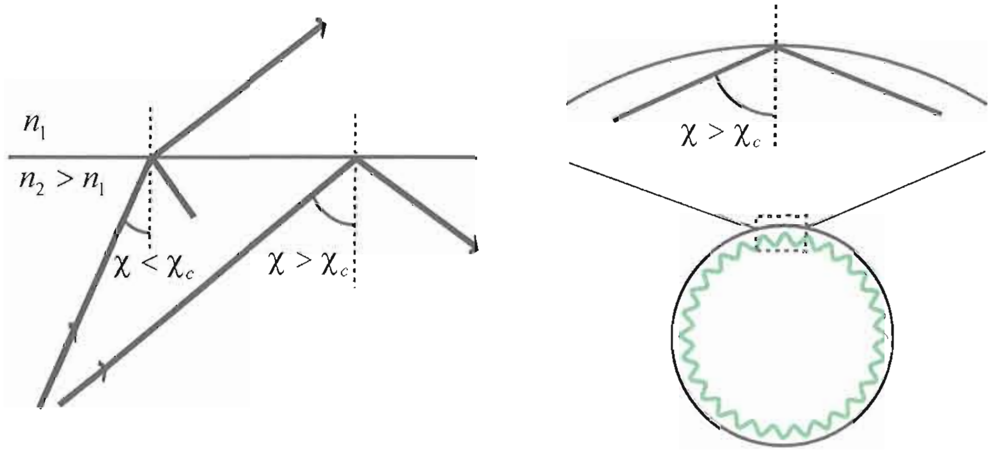

Figure 2.1: When light travels from a higher refractive index material to a lower index, total internal reflection occurs at an angle of incidence, χ, equal to or greater than the critical angle, χ_c. Whispering gallery modes are formed by total internal reflection in a microsphere resonator.

of the whole resonator volume. These unique optical properties make the silica resonators suitable in a variety of experimental studies [48], including cavity-QED [49, 50], ultralow threshold lasing [51], and cavity optomechanics [43, 44, 52].

A silica microsphere is also an elastic mechanical resonator. Vibrational modes of a microsphere are determined by the boundary conditions as well as the mechanical properties, such as the mass density and Young's modulus. Resonance frequency, which is inversely proportional to the size, ranges in ultrasonic band, from above 100 MHz for a 30 μm diameter. On the other hand, the spatial pattern of the vibration is of special importance in view of optomechanical coupling. Assuming that WGMs lie near the equatorial plane, the vibrational modes which can induce changes in the radial amplitude in that plane are effectively coupled with WGMs. In this case, phases of the circulating fields features an oscillation at the mechanical vibration frequency. These radial breathing modes can also have extremely high elasticity with mechanical quality factors $Q_m \geq 10,000$.

In this chapter, we will discuss the optical WGMs and the mechanical vibrations of a silica microsphere resonator. The realistic model of a microsphere-stem system will be simulated with finite element analysis to characterize the frequency and the spatial pattern of mechanical vibration modes.

2.1 Whispering Gallery Modes in Silica Microspheres

From Maxwell's equations, the electric field of WGMs formed in a dielectric microsphere is described by a Helmholtz equation,

$$\nabla^2\mathbf{E} + n^2k^2\mathbf{E}^2 = 0 \tag{2.1}$$

where n is the refractive index of a microsphere and k is the wavevector in vacuum. For simplicity, here we consider only a TE-wave whose polarization is perpendicular to the propagation direction in the tangential plane of the equator. Using separation of variables, the solution of the TE-wave in Eq.(2.1) can be written as,

$$E(\mathbf{r}) = R_{lm}(r)X_{lm}(\theta,\phi) \tag{2.2}$$

$$X_{lm}(\theta,\phi) = \frac{\mathbf{r}\times i\nabla Y_{lm}}{\sqrt{l(l+1)}} \tag{2.3}$$

where R_{lm} and X_{lm} are the radial and the angular part solutions, respectively, and Y_{lm} are spherical harmonics.

Considering the momentum of a photon traveling at near-glancing incidence, the integer l is identified as the angular momentum. It is approximately the same as the total number of reflections,

$$l \approx \frac{2\pi R}{\lambda/n} \tag{2.4}$$

for a large sphere $R \gg \lambda$ where λ is a wavelength in vacuum and R is the microsphere radius. The integer $m = -l, \ldots, 0, \ldots, l$ is the azimuthal mode number, and $|l-m|$ describes the number of nodes along the polar angle. These mode numbers, along with a radial mode number, p, consist of three mode numbers characterizing the spatial distribution of the WGMs in the spherical microsphere resonator, in analogue to three quantum numbers describing the wavefunctions in a hydrogen atom.

From Eq.(2.1) $\sim$ Eq.(2.3), the radial equation of R_{lm} has the form

$$\frac{d^2 R_{lm}}{dr^2} + \frac{2}{r}\frac{dR_{lm}}{dr} + \left(n^2 k^2 - \frac{l(l+1)}{r^2}\right) R_{lm} = 0 \tag{2.5}$$

This is a Bessel equation of order $l + 1/2$. Then, the solutions of the radial equation are,

$$R_{lm}(r) = \begin{cases} j_l(nkr) & \text{for } r \leq R \\ n_l^{(1)}(kr) & \text{for } r > R \end{cases} \tag{2.6}$$

where j_l is a spherical Bessel function and $n_l^{(1)}$ is a spherical Hankel function of the first kind. The boundary conditions are that the radial solution and its derivative should be continuous at $r = R$, which yields,

$$\begin{aligned} nlj_{l-1}(nkR) &- n(l+1)j_{l+1}(nkR) \\ &- \frac{j_l(nkR)}{n_l^{(1)}(kR)}(ln_{l-1}^{(1)}(kR) - (l+1)n_{l+1}^{(1)}(kR) = 0 \end{aligned} \tag{2.7}$$

By numerically solving this equation for a given value of l, a series of k_p, with $p = 1, 2, \ldots$, are obtained. The radial mode number, p, denotes $p-1$ nodes of the electric field of WGMs in the radial direction. Figure 2.2 shows the intensity distribution of the radial functions for $p = 1$ and $p = 2$ modes. The peaks are located within one wavelength of the surface, and the intensity decays exponentially beyond the microsphere. The skin depth is given as,

$$\delta = \frac{\lambda}{2\pi\sqrt{n^2 - 1}} \tag{2.8}$$

for $l - m = 0$. The skin depth is approximately 110 nm at $\lambda = 800$ nm for a silica microsphere.

The radial equation gives more insight about the WGMs when this equation is compared with the Schrödinger equation in quantum mechanics. The radial equation of the WGMs can be rewritten as,

$$\frac{d^2 R_{lm}}{dr^2} + \frac{2}{r}\frac{dR_{lm}}{dr} + (k^2 - V_{eff})R_{lm} = 0 \tag{2.9}$$

where V_{eff}, the effective potential, is defined as,

$$V_{eff} = \frac{l(l+1)}{r^2} + k^2(1 - n^2) \tag{2.10}$$

Eq.(2.9) is the same as the Schrödinger equation if we consider a WGM as the wavefunction of a particle that is confined in a radial potential well. In this analogue, k^2 corresponds to the total energy of the particle, and the effective potential depends on the wavevector as well as on the radius. Due to the step-like change in the refractive index, the effective potential discontinues at $r = R$ as schematically drawn in Fig. 2.2. In the same way that a particle with total energy smaller than a potential barrier can be bounded in the potential well, the optical fields with k^2 smaller than the effective potential barrier are allowed to form the WGMs in a microsphere. In order to have nontrivial solutions for a given effective potential, k should lie in the ranges of,

$$\frac{l + 1/2}{R\,n} \leq k \leq \frac{l + 1/2}{R} \tag{2.11}$$

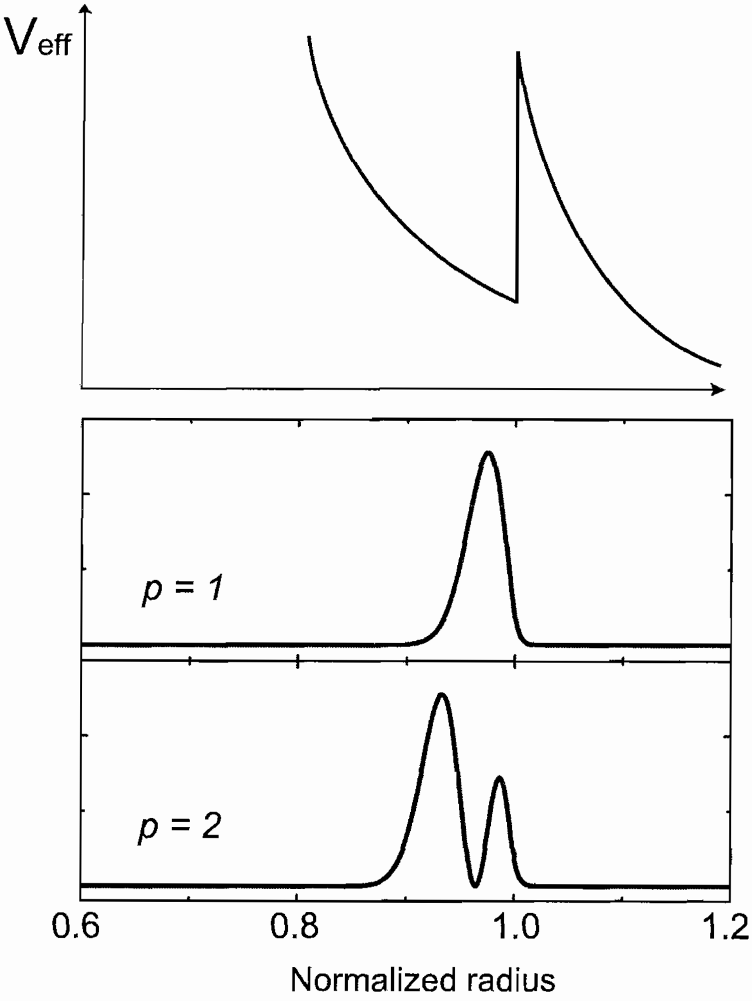

Figure 2.2: Effective potential barrier for the radial part of WGMs in a microsphere resonator. The discontinuity at $r = R$ is due to the change of refractive index. Radial part solutions of WGMs are displayed for $p = 1$ and 2 modes with $R = 15\ \mu m$ and $l = 173$. We use $n = 1.457$ for $r \leq R$ and $n = 1$ for $r > R$ for fused silica.

where we used $l(l + 1) \approx (1 + 1/2)^2$ for large l. Eq.(2.11) together with Eq.(2.7) determines the allowed discrete mode numbers for the WGMs in a microsphere. The value of k is also closely related to the angle of incidence of the WGMs. For the lowest k, which corresponds to the $p = 1$ radial mode, a WGM is tightly confined within a wavelength from the microsphere surface with a small mode volume, as shown in Fig. 2.2. In this case, the angle of incidence is nearly 90 degrees, the glancing incidence. For the higher radial modes, the angle of incidence decreases and approaches the critical angle for $k \sim k_{max}$.

Similar to the tunneling phenomenon in quantum mechanics, a WGM can evanescently escape beyond the potential barrier. As k increases, the potential barrier gets smaller. Therefore, the evanescent escape grows exponentially as the angle of incidence approaches the critical angle. This fact is closely related to free-space evanescent excitation of WGMs in deformed microspheres.

The optical energy in WGMs in a silica microsphere resonator decays with time. The light can be scattered due to surface roughness or particles on the surface, and can be absorbed by the material. WGMs can also leak outside through evanescent escape across the potential barrier. In order to characterize the energy loss in WGMs, we commonly use the optical Q-factor defined as,

$$Q \equiv 2\pi \frac{\text{total energy}}{\text{energy loss for one cycle}} \tag{2.12}$$

For fused silica microspheres, a Q-factor as high as 8×10^9 was demonstrated [47]. It is well known that water vapor deposited on the microsphere surface significantly spoils the Q-factors of WGMs. For use of silica microspheres in experiments, silica microspheres are usually kept in a chamber filled with an inert gas such as N_2 or He gas, in order to prevent Q-spoiling from possible contaminations. Experimentally the optical Q-factor is determined by,

$$Q = \frac{\omega_c}{\kappa} \tag{2.13}$$

where $\omega_c/2\pi$ and $\kappa/2\pi$ are the resonance frequency and the full width of half maximum of the measured WGM spectrum, respectively.

The sharpness of the spectral peak is also characterized in terms of optical finesse, which is defined as,

$$F \equiv \frac{\omega_{FSR}}{\kappa} \tag{2.14}$$

where ω_{FRS} is the free spectral range, the mode spacing between two successive azimuthal mode numbers, given by,

$$\omega_{FSR} = \frac{c}{nR} \qquad \text{or} \qquad \lambda_{FSR} = \frac{\lambda_c^2}{2n\pi R} \tag{2.15}$$

in a microsphere with a radius R. Here, λ_c is the resonance wavelength. The free spectral range can give an alternative, accurate measure of the microsphere size by using Eq.(2.15). The optical finesse in a microsphere can now be rewritten as $F = \frac{c}{n\kappa R}$, which is independent of the cavity resonant frequencies or wavelengths.

Another important parameter describing optical resonators is the mode volume that the electromagnetic field spatially occupies in the resonator. The mode volume of the WGMs in microsphere is,

$$V \simeq 3.4\pi^{3/2}(\frac{\lambda}{2\pi n})^3 l^{11/6}\sqrt{l-m+1} \tag{2.16}$$

for the lowest radial mode [53]. Assuming the $l = m$ mode, with a radius $R = 15$ μm and a wavelength $\lambda = 800$ nm, the mode volume is approximately 150 μm^3, which is only ~ 1 % of the whole microsphere volume. The small size of the WGM mode volume leads to strong electromagnetic fields, which are tightly confined just under the microsphere surface.

2.2 Mechanical Vibration Modes of Silica Microspheres

The mechanical vibration modes in a homogeneous and isotropic elastic sphere with free surface boundary conditions can be calculated with a well established theory, first developed back in 1878 by H. Lamb [54]. The wave equation governing the elastic mechanical motions is given by [55, 56],

$$\rho\, \ddot{\mathbf{u}} = (\lambda + 2\mu)\nabla(\nabla \cdot \mathbf{u}) - \mu\nabla \times (\nabla \times \mathbf{u}) \tag{2.17}$$

where $\mathbf{u}(\mathbf{r})$ is the displacement vector and ρ is the mass density. $\lambda = \dfrac{\sigma E}{(1+\sigma)(1-2\sigma)}$ and $\mu = \dfrac{E}{2(1+\sigma)}$ are Lamb constants. E is Young's modulus and σ is Poisson's ratio. The solution of this equation for a particular geometry can be obtained with proper boundary conditions. In case of a silica microsphere-stem geometry, the resonator is hung at the end of a tapered optical fiber with a diameter of one tenth of the microsphere diameter. Thus, only a small fraction less than 1% of the microsphere surface is constrained to the fiber stem. Under this circumstance, the microsphere-stem system can be reasonably approximated by a free microsphere with stress-free-surface boundary conditions. More detailed analysis in a microsphere-stem structure will be given with finite element simulations.

The general solution of Eq.(2.17) for an elastic sphere under the free-surface boundary condition has the form,

$$\Psi_i(\mathbf{x}, t) = \sum_{l,m} A_i^{(l,m)} j_l\left(\frac{\omega_{l,m} r}{V_i}\right) Y_l^m(\theta, \phi) e^{-i\omega_{l,m} t} \tag{2.18}$$

where j_l and Y_l^m are the spherical Bessel function and the spherical harmonics, respectively. $\omega_{l,m}/2\pi$ is the mechanical vibration frequency of a (l,m) mode where l and m are the mode numbers. V_i denotes the longitudinal sound velocity for $i = 1, 2$ and the transverse sound velocity for $i = 3$, respectively. These velocities are also expressed as $V_1 = V_2 = V_L = \sqrt{\frac{\mu}{\rho}}$ and $V_3 = V_T = \sqrt{\frac{\lambda + 2\mu}{\rho}}$ in terms of Lamb constants. For fused silica with $\rho = 2.2\ g/cm^3$, $E = 73.1$ GPa, and $\sigma = 0.17$, we obtain $V_L = 3766\ m/s$ and $V_T = 5970\ m/s$.

The mechanical vibration modes of a microsphere fall into two categories, namely, the torsional and the spheroidal modes. While torsional modes are purely rotational without dilatation, the spheroidal modes involve dilatation without any rotation. In optomechanical coupling, we are more interested in the spheroidal modes because these modes can change the optical path length and in turn the optical resonances in a microsphere resonator. The eigenvalues of the spheroidal modes of an elastic sphere are determined by [56],

$$\begin{aligned} &2\left[\eta^2 + (l-1)(l+2)\left(\frac{\eta j_{l+1}(\eta)}{j_l(\eta)} - (l+1)\right)\right]\frac{\xi j_{l+1}(\xi)}{j_l(\xi)} \\ &- \frac{1}{2}\eta^4 + (l-1)(2l+1)\eta^2 + [\eta^2 - 2l(l-1)(l+2)]\frac{\eta j_{l+1}(\eta)}{j_l(\eta)} = 0 \end{aligned} \tag{2.19}$$

where η and ξ are the dimensionless eigenvalues, which can be rewritten as,

$$\xi_{nl} = \frac{\omega_{nl} R}{V_L} \tag{2.20}$$

$$\eta_{nl} = \frac{\omega_{nl} R}{V_T} \tag{2.21}$$

where R is the microsphere radius and n is the radial mode number that is assigned to the n-th zero of ω's satisfying the boundary conditions. For a given l, Eq.(2.19) can be numerically solved for a parameter $\chi_{nl} \equiv \frac{R\omega_{nl}}{2\pi}$. In Fig. 2.3 the values of χ_{nl} for

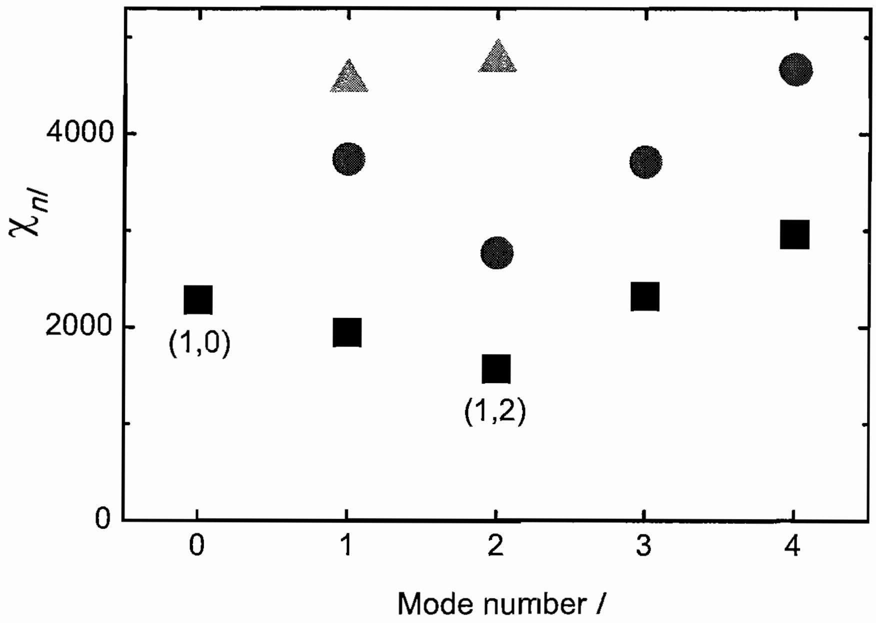

Figure 2.3: Spheroidal vibration modes of a silica microsphere. The value of the parameter χ_{nl} is plotted for the mode number l. Square, circle and triangle represent the mode numbers $n = 1$, 2 and 3, respectively.

$n = 1, 2$ and $l = 0, 1, 2, 3,$ and 4 for the spheroidal modes are plotted. It is interesting to note that the $(1, 2)$ mode has the lowest vibration frequency. For vibration shape, n indicates $(n - 1)$ nodes in the radial direction. The eigenvalue equation does not involve the mode number m, indicating $2l + 1$ degeneracy in the spheroidal modes for each l mode. Although the vibration frequencies for the same l mode are degenerate, the spatial vibration shapes are distinct for different $m = - l, ..., + l$ as will be analyzed with finite element analysis.

2.3 Finite Element Analysis of a Microsphere-Stem System

The mechanical vibration modes of a silica microsphere are simulated and characterized with finite element analysis using a commercial program, COMSOL Multiphysics. Finite element simulation not only gives the vibration frequencies, but also displays the corresponding spatial patterns, which are more important in view of optomechanical coupling. For simulations, we have modeled a microsphere-stem system as a sphere attached to the end of a cylindrical stem whose diameter is set to one tenth of a microsphere diameter. The other end of the stem is smoothly connected to a tapered cone whose height and base diameter are set to 200 μm for both. The whole structure is assigned as fused silica and all surfaces are set to be free-stress except for a fixed cone base. In experimental studies of optomechanical cooling, the microsphere is slightly deformed for the free-space excitation of WGMs, which will be discussed in detail in Chapter IV. The deformed microsphere is modeled as an ellipsoid where one axis on the equatorial plane is longer than other two perpendicular axes of the same length.

Fig. 2.4 shows fundamental spheroidal modes of mechanical vibration of a stem-microsphere system for the $n = 1$ mode number. $D = 30$ μm microsphere diameter, 30 μm stem length, and $\epsilon = 2$ % deformation are used in this simulation. The radial breathing modes, in which average radial displacement in the equatorial plane changes with mechanical vibration, are displayed for $(1,0)$, $(1,2)$ and $(1,4)$ modes in Fig. 2.4(a). The existence of the fiber stem slightly deforms the vibration shape in the proximity of the microsphere-stem joint. For the $(1,0)$ mode, the vibration frequency is 152 MHz and the overall sphere shrinks and expands with the same phase for all points in the microsphere. In the $(1,2)$ mode with 105 MHz vibration frequency, the microsphere is elongated along the fiber stem direction. This mode, named the American football mode, has the lowest vibration frequency and shows out of phase vibration motion between the pole and the equator of the microsphere. The radial breathing mode in the $(1,4)$ mode, vibrating at 199 MHz, shows vibration nodes along the polar angle with a cylindrical symmetry. For the $(1,1)$ mode with 128 MHz and the $(1,3)$ mode with 153 MHz shown in Fig. 2.4(b), the

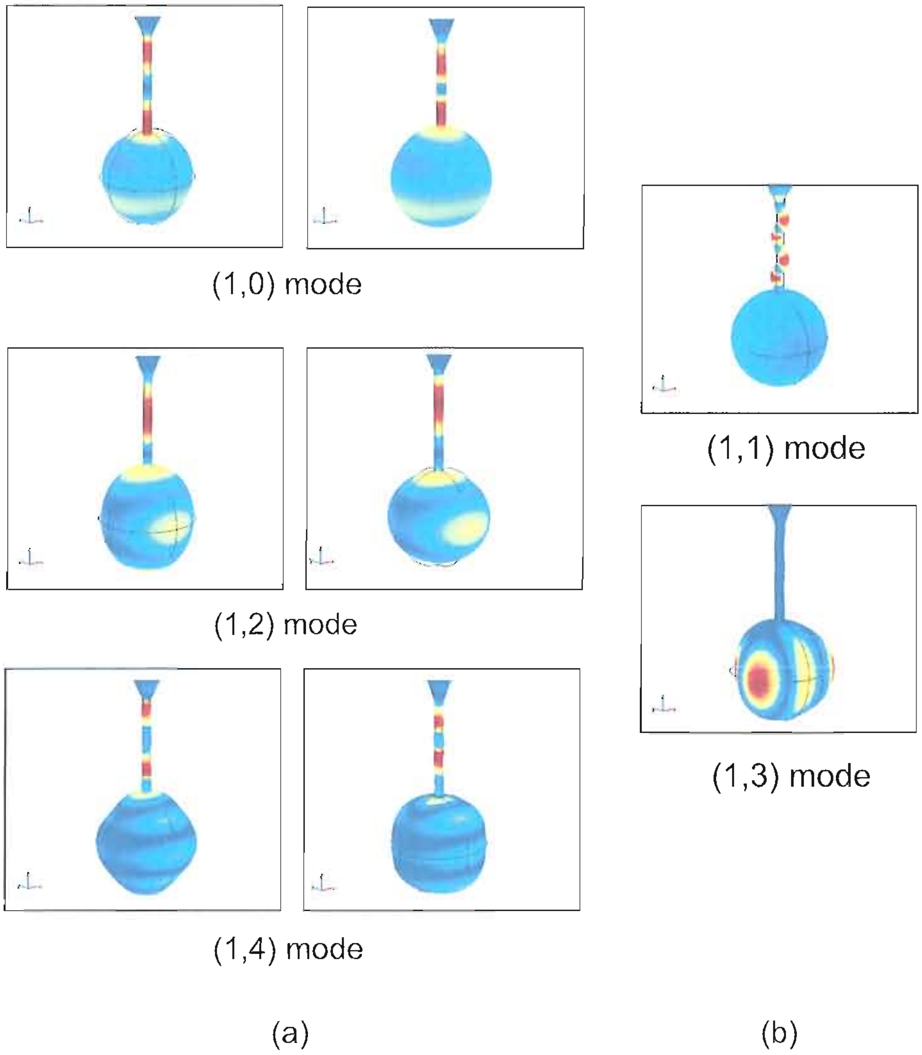

(1,0) mode

(1,2) mode

(1,4) mode

(1,1) mode

(1,3) mode

(a)

(b)

Figure 2.4: Finite element simulation of mechanical vibration modes of a microsphere-stem system. Fundamental spheroidal modes are shown for the $(n, l) = (1, 0)$, $(1, 1)$, $(1, 2)$, $(1, 3)$ and $(1, 4)$ modes. For radial breathing modes in (a), two spacial mode patterns in opposite phases are displayed to show the radial displacement. In (b), non-radial spheroidal modes are shown. In this simulation, the deformation is $\epsilon = 2$ %, and the diameter of the fiber stem is equal to one tenth of the microsphere diameter, 30 μm.

change in the average radial displacement is negligible, resulting in no optomechanical coupling.

Due to the fiber stem and the microsphere deformation, the degeneracy of higher l modes is lifted. For example, Fig. 2.5 shows the breaking of the fivefold degeneracy in the $(1, 2)$ mode, resulting in five different frequencies within a few MHz range for different m mode numbers. For the other four modes, except for the radial breathing mode, the average radial displacement remains nearly constant during vibration in spite of their dynamical change in shape. These modes are optically invisible.

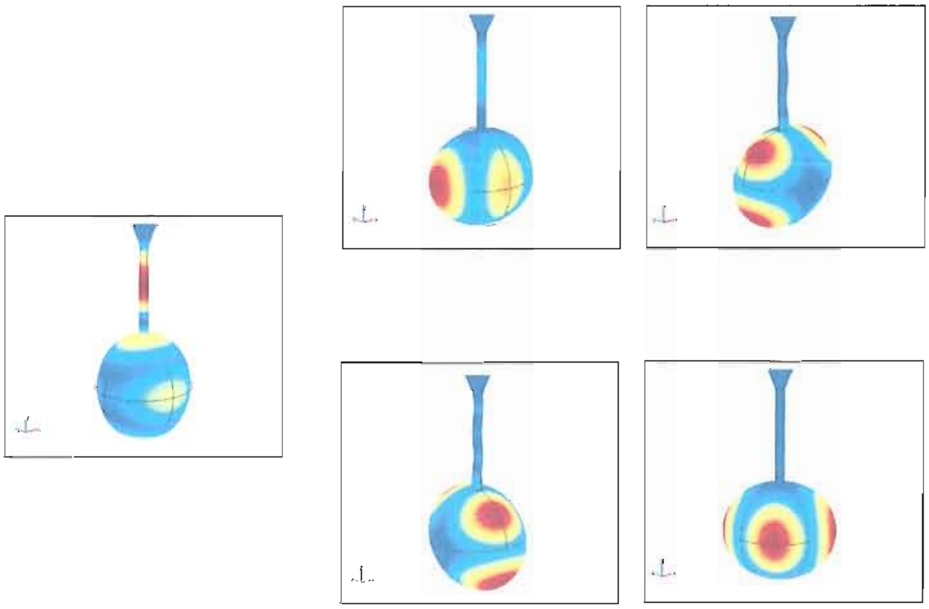

(a) (b)

Figure 2.5: Degeneracy of a $(1, 2)$ mechanical vibration mode. A five-fold degeneracy in the vibration frequency is split due to the fiber stem and the deformation. Only the radial breathing mode in (a) that can change cavity path length is optically visible. In (b), non-radial breathing modes are shown.

2.4 Effective Mass

With finite element analysis, we have shown that each mechanical mode has its own distinct vibration shape. In view of optomechanical coupling, even though the maximal deformation is greatly different from an equilibrium shape, the optical resonance shift will be negligible if there is no cavity path change in the equatorial plane of mechanical vibration. For example, see the non-radial breathing modes in Fig. 2.5(b). Considering mechanically induced cavity path length change, the mechanical oscillator can be characterized by introducing the effective mass, m_{eff}, which is defined as [57],

$$m_{eff} = \frac{2E_m}{\omega_m^2 A^2} \tag{2.22}$$

where E_m is the total mechanical energy, ω_m is the angular vibration frequency, and A is the average radial amplitude in the equatorial plane. The effective mass is interpreted as the mass of a one-dimensional equivalent harmonic oscillator whose amplitude is equal to the average radial amplitude. From this definition, it is straightforward to see that the effective mass is infinite for non-breathing modes due to their negligible radial amplitude. However, for the radial breathing modes, the effective mass can be larger or smaller than the physical mass, depending on vibration shape. As a mass is considered an inertia of the kinetic motion subject to an external force, the effective mass acts as an inertia of the mechanical vibration motion subject to the radiation pressure force in optomechanical coupling.

The effective mass of mechanical vibration modes in a deformed microsphere is simulated with finite element analysis as shown in Fig. 2.6. Since the microspheres are usually fabricated in different sizes, it is convenient to define the effective mass coefficient, α, as,

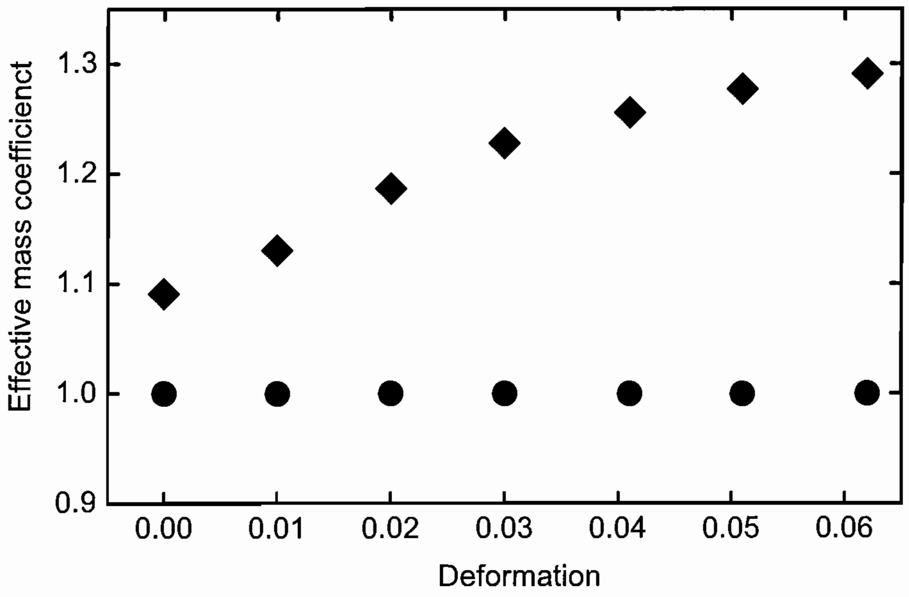

Figure 2.6: Effective mass coefficient for the $(1,0)$ and $(1,2)$ radial breathing modes simulated with finite element analysis. In this simulation, the microsphere diameter with $\epsilon = 0$ is 30 μm and the long axis length in the equatorial plane is changed in order to impose a deformation.

$$\alpha = \frac{m_{eff}}{m} \tag{2.23}$$

where m is the whole microsphere mass. For each mode, the radial displacement in the equatorial plane is averaged over a circumference, and the total mechanical energy or the elastic energy is calculated at the average radial amplitude. Microsphere deformation is applied by changing the long axis length in the equatorial plane and $\epsilon = 0$ corresponds to a 30 μm diameter spherical microsphere. Figure 2.6 shows the simulated effective mass coefficients of the $(1,0)$ and $(1,2)$ radial breathing modes as a function of deformation. While the coefficient for the $(1,2)$ mode increases slightly with increasing deformation, the coefficient for the $(1,0)$ mode remains nearly constant for differing deformation. At $\epsilon = 2$ %, the effective mass coefficients are found as $\alpha_{(1,0)} = 1.01$ for the $(1,0)$ mode and $\alpha_{(1,2)} = 1.19$ for the radial breathing

$(1, 2)$ mode. These correspond to the effective masses of 32 ng for the $(1, 0)$ mode and 38 ng for the $(1, 2)$ mode. We also find that the effective mass coefficient of each mode remains nearly the same irrespective of the microsphere diameter.

Effective mass can be used to calibrate the measured mechanical displacement spectrum. According to the equipartition theorem, the peak amplitude of the displacement spectrum depends only on the effective mass for a given bath temperature. For example, with $D = 30\ \mu m$, $\epsilon = 2\ \%$ and $\mathrm{T} = 300$ K, we simulate the average radial amplitude of $1.56 \times 10^{-14}\ m$ of the radial breathing $(1, 2)$ mode, which results in the peak value of $1.25 \times 10^{-16}\ m/\sqrt{\mathrm{Hz}}$ in the mechanical displacement spectral density for a mechanical quality factor $Q_m = 10{,}000$ and a 100 MHz vibration frequency.

CHAPTER III

THEORETICAL BACKGROUND OF OPTOMECHANICAL COOLING

In a theoretical description of optomechanical cooling, a radial breathing mechanical mode can be approximated as a one-dimensional harmonic oscillator [35] (See Fig. 3.1). This equivalent harmonic oscillator, which is in thermal equilibrium with bath temperature, is subject to the radiation pressure force arising from the circulating optical power. The fact that thermal mechanical vibrations of the resonator induce changes in optical resonances and that the radiation pressure force is delayed due to a finite cavity lifetime [32] yields two coupled differential equations governing the mechanical motion and the intracavity optical field. The forced harmonic motion is characterized by the effective mechanical frequency and the effective mechanical linewidth. A position-dependent and time-delayed radiation pressure force leads to the shift of mechanical resonance (i.e. optical spring effect [58]) and the change in the damping rate, respectively. Interestingly, the radiation pressure induced damping rate can be either positive, meaning heating of the mechanical motion, or negative, meaning cooling of the mechanical motion, depending on the laser detuning.

According to the equipartition theorem, the change in temperature of the vibration motion is given simply by the ratio between the effective damping rate and an intrinsic damping rate. Classically the effective temperature would be arbitrarily small with increasing circulating power and, accordingly, the effective damping rate

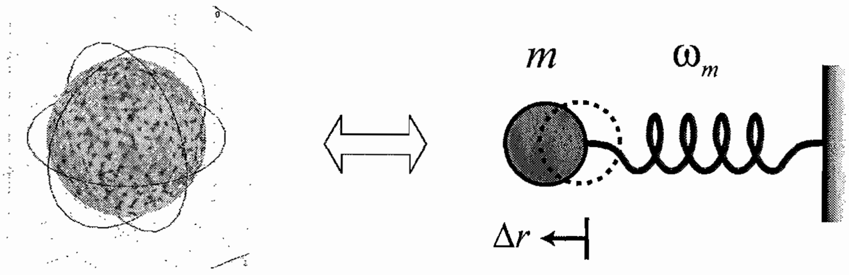

Figure 3.1: One-dimensional harmonic oscillator equivalent to the (1, 0) radial breathing mode of a microsphere resonator with the assumption of same vibration frequency and total mechanical energy. The amplitude is assigned to be the same as the radial amplitude (Δr) in the equatorial plane, and m is the effective mass.

would be arbitrarily large. The effective temperature needs to be below 5 mK in order to reach the ground state of a 100 MHz mechanical oscillator.

However, quantum theory predicts that the radiation pressure cooling will be ultimately limited by quantum backaction, the fluctuation of the radiation pressure force arising from the shot noise of circulating power. The ground-state cooling of mechanical motion with phonon occupation far below one can in principle be achieved only in the resolved-sideband limit, where the cavity photon lifetime is comparable to or larger than the mechanical vibration period [28–30, 59].

In this chapter, we will first discuss a one-dimensional harmonic oscillator in thermal equilibrium. Theoretical calculations of optomechanical coupling in a silica optomechanical resonator will be presented to derive analytic forms of the effective frequency and damping rate. We will also discuss the cooling limit imposed by quantum backaction, emphasizing the importance of the resolved-sideband condition.

3.1 1D Harmonic Oscillator in Thermal Equilibrium

Consider a one-dimensional harmonic oscillator with mass m subject to thermal random force F_{th} [13]. Assuming velocity dependent friction, the equation of motion is,

$$m\ddot{x} + \gamma\dot{x} + kx = F_{th} \tag{3.1}$$

where γ is the damping rate and k is the stiffness. F_{th} is given in the frequency domain as,

$$F_{th}^2 = 4m\gamma k_B T \tag{3.2}$$

where k_B is the Boltzman constant and T is the bath temperature. Note that F_{th} is independent of the resonant frequency. This fluctuation force, which is also called Langevin force, is responsible for the random driving force as well as the frictional force as stated in fluctuation-dissipation theorem [60]. The equation of motion of a harmonic oscillator in Eq.(3.1) is solved in the frequency domain by replacing $x(t)$ with $x(\omega)e^{i\omega t}$, and the solution reads,

$$x^2(\omega) = \frac{4k_B T}{m} \frac{\gamma}{(\omega^2 - \omega_0^2)^2 + \gamma^2\omega^2} \tag{3.3}$$

where $\omega_0/2\pi$ is the resonance frequency. This is the power spectral density of vibration displacement and has units of $[m^2/\text{Hz}]$. The amplitude on resonance is linear with temperature as expected from the thermally excited motion. When the damping rate is small, the response is sharply peaked near the resonance and approximately given by a Lorentz shape. Its sharpness is quantified by the mechanical quality factor, defined as,

$$Q_m = \frac{\omega_0}{\gamma} \tag{3.4}$$

The amplitude variance of a harmonic oscillator subject to thermal forces can be calculated by integrating the power spectral density over all frequencies as,

$$\Delta x^2 = \int_0^{\infty} x^2(\omega)\frac{d\omega}{2\pi} = \frac{k_B T}{m\omega_0^2} \tag{3.5}$$

3.2 Equipartition Theorem

In classical statistical mechanics, the equipartition theorem states that, in thermal equilibrium, the total average energy is equally distributed over the various forms in quadrature of, for example, position or velocity. The average energy of $\frac{1}{2}k_B T$ is assigned to each degree of freedom. For a one-dimensional harmonic oscillator in thermal equilibrium, the total energy is the sum of the kinetic energy and the elastic energy. And each energy is quadratic in the respective variable. Thus, the mean total mechanical energy is given by,

$$\bar{E}_m = \frac{1}{2}m\dot{x}^2 + \frac{1}{2}kx^2 = \frac{1}{2}k_B T + \frac{1}{2}k_B T = k_B T \tag{3.6}$$

The mean kinetic energy is equal to the mean elastic energy.

The average amplitude of the mechanical oscillator is calculated through the equipartition theorem, as,

$$\Delta x = \sqrt{\frac{k_B T}{m\omega_0^2}} \tag{3.7}$$

This expression is exactly the same result as Eq.(3.5). By rewriting this equation, we obtain,

$$T = \frac{m\omega_0^2}{k_B}\Delta x^2 \tag{3.8}$$

This equation says that the average amplitude is a direct measure of the temperature of the vibration motion.

3.3 Classical Theory of Optomechanical Cooling in a Microsphere

The radiation pressure force in a microsphere, which is exerted on the boundary due to multiple reflections of photons, is,

$$F_{rad} = \frac{2\pi n}{c} P_{cav} \tag{3.9}$$

where P_{cav} is the intracavity power, c is the speed of light in vacuum and n is the refractive index of silica. This force is in radial direction in the equatorial plane as shown in Fig. 3.2, and acts as a driving force to the radial vibration motion of a microsphere. For simplicity, we consider only a single mechanical mode which is approximated as a one-dimensional harmonic oscillator. The equation of motion of the radial displacement, $r(t)$ can be written as [61],

$$\ddot{r}(t) + \gamma_m \, \dot{r}(t) + \omega_m^2 r(t) = \frac{F_{rad}}{m} \tag{3.10}$$

where m is an effective mass, and ω_m and γ_m are a mechanical vibration angular frequency and damping rate, respectively.

On the other hand, the equation of the intracavity electric field follows [62],

$$\dot{\mathrm{E}}_{cav}(t) = \left(-\frac{\kappa}{2} + i\Delta\omega_R\right) \mathrm{E}_{cav}(t) + \frac{it}{T_{rt}} \Gamma \mathrm{E}_{in} \tag{3.11}$$

where it is the transmission coefficient, T_{rt} is the round trip time and Γ is the mode-matching coefficient. The frequency change is given by,

$$\Delta\omega_R = \Delta\omega + \omega_0 \frac{r(t)}{R} \tag{3.12}$$

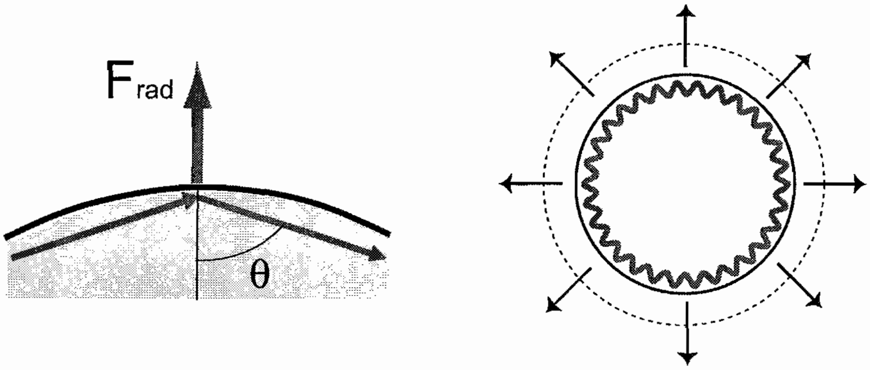

Figure 3.2: The momentum change of a photon circulating inside a cavity exerts a radiation pressure force proportional to the intracavity power on the surface of a microsphere. By symmetry, the force is in the radial direction on the equatorial plane.

where the first term $\Delta\omega = \omega_L - \omega_c$ is the laser detuning and the second term is the phase shift due to the mechanical vibration. ω_L and ω_c are the angular frequency of the excitation laser and the optical resonance, respectively, and R is a WGM radius, which is nearly the same as a microsphere radius. These two coupled differential equations, Eq.(3.10) and Eq.(3.11), govern the optomechanical coupling due to the radiation pressure force.

With an explicit time dependence, $e^{i\omega_m t}$, the radial displacement can be rewritten as,

$$r(t) = \frac{1}{2} x_m e^{i\omega_m t} + \frac{1}{2} x_m^* e^{-i\omega_m t} \tag{3.13}$$

where x_m is the slowly varying amplitude. Then, using Eq.(3.13), Eq.(3.10) and Eq.(3.11), it becomes,

$$\left(\dot{x}_m + \frac{\gamma_m}{2} x_m\right) e^{i\omega_m t} - \left(\dot{x}_m^* + \frac{\gamma_m}{2} x_m^*\right) e^{-i\omega_m t} = -i \frac{\pi n^2 \epsilon_0 s}{m \omega_m} |\mathrm{E}_{cav}|^2 \tag{3.14}$$

$$\dot{\mathrm{E}}_{cav}(t) = -\left(\frac{\kappa}{2} + i\Delta\omega + i\frac{\omega_0}{2R}\left(x_m e^{i\omega_m t} + x_m^* e^{-i\omega_m t}\right)\right) \mathrm{E}_{cav}(t) + \frac{it}{T_{rt}} \Gamma \mathrm{E}_{in} \tag{3.15}$$

Here we assume $\omega_m \gg \gamma$ and $\ddot{x}_m \ll \omega_m \dot{x}_m$. ϵ_0 is the permittivity of free space, and s and E the cross sectional area and the electric field of a relevant WGM, respectively.

Assuming the Stokes and the anti-Stokes fields generating from the parametric process in a microresonator, the electric field can be decomposed as [63],

$$\mathrm{E}_{cav}(t)e^{i\Delta\omega t} = \mathrm{E}_p(t)e^{i\Delta\omega t} + \mathrm{E}_s(t)e^{i\Delta\omega_s t} + \mathrm{E}_{as}(t)e^{i\Delta\omega_{as} t} \tag{3.16}$$

with

$$\Delta\omega_s = \Delta\omega - \omega_m \tag{3.17}$$

$$\Delta\omega_{as} = \Delta\omega + \omega_m \tag{3.18}$$

where p, s and as denote a pump, Stokes and anti-Stokes, respectively. Inserting Eq.(3.16) into Eq.(3.14) and Eq.(4.7), and sorting these equations by each electric field component, we reach four coupled equations, as follows,

$$\dot{\mathrm{E}}_p = \left(-\frac{\kappa}{2} + i\Delta\omega\right)\mathrm{E}_p + \frac{\omega_0}{2R}\left(x_m\mathrm{E}_s + x_m^*\mathrm{E}_{as}\right) + \frac{it}{T_{rt}}\Gamma\mathrm{E}_{in} \tag{3.19}$$

$$\dot{\mathrm{E}}_s = \left(-\frac{\kappa}{2} + i\Delta\omega_{as}\right)\mathrm{E}_s + \frac{\omega_0}{2R}x_m^*\mathrm{E}_p \tag{3.20}$$

$$\dot{\mathrm{E}}_{as} = \left(-\frac{\kappa}{2} + i\Delta\omega_s\right)\mathrm{E}_{as} + \frac{\omega_0}{2R}x_m\mathrm{E}_p \tag{3.21}$$

$$\dot{x}_m = -\frac{\gamma_m}{2}x_m - \frac{i\pi n^2\epsilon_0 s}{m\omega_m}\left(\mathrm{E}_p^*\mathrm{E}_{as} + \mathrm{E}_p\mathrm{E}_s^*\right) \tag{3.22}$$

Assuming $\mathrm{E}_s, \mathrm{E}_{as} \ll \mathrm{E}_p$, we solve for E_s and E_{as} in terms of E_p from Eq.(3.19) $\sim$ Eq.(3.21) in steady-state. Then, by inserting the solutions into Eq.(3.22), the equation of x_m is now put into a simple form as,

$$\dot{x}_m = \left(-\frac{\gamma_m + \Gamma_c}{2} + i\Delta\omega_m\right)x_m \tag{3.23}$$

This equation describes the harmonic motion with the effective damping rate, $\gamma_{eff} = \gamma_m + \Gamma_c$, and the effective resonance frequency, $\omega_{eff} = \omega_m + \Delta\omega_m$, where the radiation pressure induced damping rate Γ_c and frequency shift $\Delta\omega_m$ are found [35],

$$\Gamma_c = \frac{8}{mR^2}\frac{\omega}{\omega_m \kappa}\frac{\Gamma^2 \kappa_c P_{in}}{\kappa^2 + 4\Delta\omega^2}\left(\frac{\kappa^2}{\kappa^2 + 4(\Delta\omega + \omega_m)^2} - \frac{\kappa^2}{\kappa^2 + 4(\Delta\omega - \omega_m)^2}\right) \quad (3.24)$$

and

$$\Delta\omega_m = \frac{8}{mR^2}\frac{\omega}{\omega_m \kappa}\frac{\Gamma^2 \kappa_c P_{in}}{\kappa^2 + 4\Delta\omega^2}\left(\frac{\kappa(\Delta\omega + \omega_m)}{\kappa^2 + 4(\Delta\omega + \omega_m)^2} - \frac{\kappa(\Delta\omega - \omega_m)}{\kappa^2 + 4(\Delta\omega - \omega_m)^2}\right) \quad (3.25)$$

where κ_c is the cavity loss associated with excitation of a WGM.

As shown in Eq.(3.24), the Stokes or the anti-Stokes process can be resonantly enhanced when the relevant sideband is resonant with the cavity resonance. For blue detuning, $\Delta\omega > 0$, the Stokes process overwhelms the anti-Stokes process and the optomechanical damping rate Γ_c is negative. In this case, radiation pressure leads to an overall amplification of the mechanical oscillation. Conversely, for red detuning, $\Delta\omega < 0$, the optomechanical damping rate is positive and radiation pressure leads to an overall cooling of the mechanical oscillation. In Fig. 3.3, the effective damping rate is normalized to an intrinsic damping rate and the vibration frequency shift is plotted as a function of laser detuning for different ratios between ω_m and κ. Two extremes near $\Delta\omega/\omega_m = \pm 1$ in Fig. 3.3(a) are due to the enhanced Stokes or the anti-Stokes emission. For large ω_m/κ, i.e, in the resolved-sideband limit, the resonant peak on each side is sharpened and its linewidth approaches the cavity linewidth κ. On the other hand, $\Delta\omega$ features a unique response as the laser detuning changes. Theoretical evaluation of $\Delta\omega$ and γ_{eff} predicts a way to manifest the radiation pressure effect on the mechanical vibrations. Note that, at zero laser detuning, both γ_{eff} and $\Delta\omega_m$ are

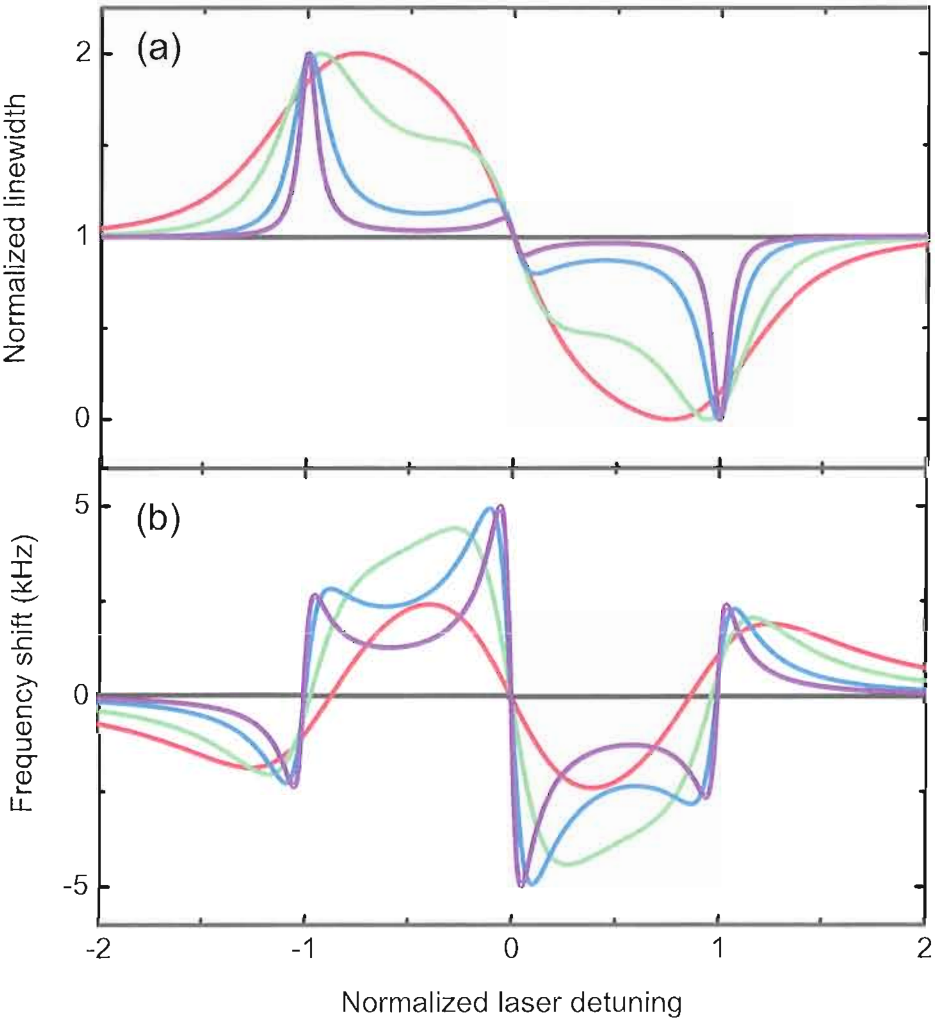

Figure 3.3: Theoretical calculation of (a) the effective linewidth normalized to the intrinsic linewidth and (b) the mechanical frequency shift as a function of laser detuning normalized to the mechanical frequency. Different ratios $\omega_m/\kappa = 1$, 2, 5 and 10 are plotted in red, green, blue and purple lines. The input power is set to the threshold power for parametric instability. Dynamic responses of γ_{eff}/γ_m and $\Delta\omega$ are the signature of radiation pressure induced optomechanical coupling.

equal to the values of the intrinsic mechanical linewidth and mechanical frequency, respectively, because of the complete balance between the Stokes and the anti-Stokes in the optomechanical parametric process.

Fig. 3.4 shows the input power dependence of the effective damping rate and the frequency shift as a function of laser detuning for $\omega_m/\kappa = 4$. Both γ_{eff}/γ_m and $\Delta\omega_m$ grow linearly with input power. For blue laser detuning, γ_{eff} can be zero at a certain input power where radiation pressure induced gain overcomes the intrinsic mechanical damping, resulting in great enhancement in the vibration amplitude along with a narrow linewidth. The threshold power for the parametric oscillation is, from $\gamma_{eff} = 0$, found as,

$$P_{th} = \gamma_m \frac{mR^2}{8} \frac{\omega_m \kappa^2}{\omega_0} \frac{\kappa^2 + 4\Delta\omega^2}{\Gamma^2 \kappa_c \kappa} \left(\frac{\kappa^2}{\kappa^2 + 4(\Delta\omega - \omega_m)^2} - \frac{\kappa^2}{\kappa^2 + 4(\Delta\omega + \omega_m)^2} \right)^{-1} \tag{3.26}$$

This expression shows that P_{th} is proportional to the inverse of the mechanical quality factor and has a size dependence of $\sim R^2$ with an assumption of $\omega_m \sim 1/R$. A high optical Q-factor reduces the threshold power, but the exact dependence varies with κ_c and the ratio of ω_m/κ. Using Eq.(3.26) for P_{th}, the effective damping rate can be rewritten as,

$$\gamma_{eff} = \gamma_m \left(1 - \frac{P_{in}}{P_{th}(\Delta\omega)} \right) \tag{3.27}$$

This shows that γ_{eff} decreases (or increases) linearly with the input power with a slope of γ_m/P_{th} for blue detuning (or red detuning). Note that γ_m and P_{th} are experimentally measurable parameters. In the resolved-sideband limit, with $\Delta\omega = \omega_m$, the threshold power is simplified as,

$$P_{th,side} = \gamma_m \frac{mR^2}{2} \frac{\omega_m^3}{\omega_0} \frac{1}{\Gamma^2 \kappa_c / \kappa} \tag{3.28}$$

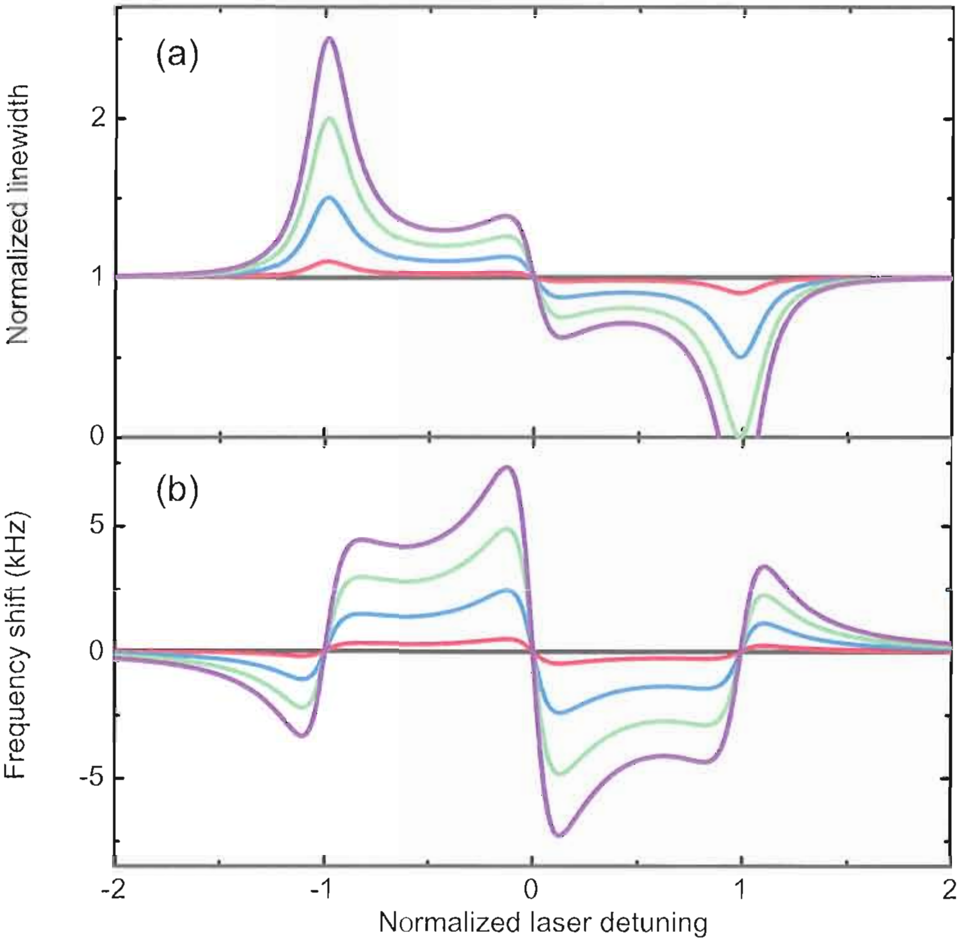

Figure 3.4: Theoretical calculation of input power dependence of (a) the effective linewidth normalized to the intrinsic linewidth and (b) the vibration frequency shift as a function of laser detuning normalized to the mechanical freqeuncy. Different ratios $P_{in} = 0.2P_{th}, 0.5P_{th}, 1P_{th}\text{and}, 1.5P_{th}$ are plotted in red, blue, green and purple lines. Both γ_{eff} and $\Delta\omega$ linearly increase with the input power. $\gamma_{eff} < 0$ is the regime of the parametric oscillation.

Under the influence of the radiation pressure force, by replacing γ_m and ω_m in the dominator with $\gamma_{eff} = \gamma_m + \Gamma_c$ and $\omega_{eff} = \omega_m + \Delta\omega$, respectively, in Eq.(3.3), the power spectral density of the radial displacement is obtained as,

$$x^2(\omega) = \frac{4k_BT}{m}\frac{\gamma_m}{(\omega^2 - \omega_{eff}^2)^2 + \gamma_{eff}^2\omega^2} \tag{3.29}$$

Note that ω_{eff} is nearly the same as ω_m owing to $\Delta\omega_m \ll \omega_m$. From the equipartition theorem, the effective temperature of the mechanical oscillator is calculated as,

$$T_{eff} = \frac{m\omega_m^2 x^2}{k_B} = \frac{m\omega_m^2}{k_B}\int x^2(\omega)\frac{d\omega}{2\pi} = \frac{\gamma_m}{\gamma_m + \Gamma_c}T \tag{3.30}$$

Therefore, the effective temperature is simply determined by the ratio between the effective and the intrinsic damping rate. For red detuning, T_{eff} is proportional to the inverse of the input power because of $\Gamma_c \propto P_{in}$. For a given Γ_c, the effective temperature depends only on γ_m for a given bath temperature, implying the crucial role of high mechanical quality factor for the optomechanical cooling. Figure 3.5 schematically shows the change of the displacement spectrum when the mechanical vibration is cooled or heated. Cooling results in the area reduction and the linewidth widening of the displacement spectrum, while heating results in the area enhancement and the linewidth narrowing.

3.4 Quantum Mechanical Description of Optomechanical Cooling

The quantum mechanical Hamiltonian of the optomechanical system is [59, 64, 65],

$$H = H_{cav} + H_m + H_{int} + H_{drive} \tag{3.31}$$

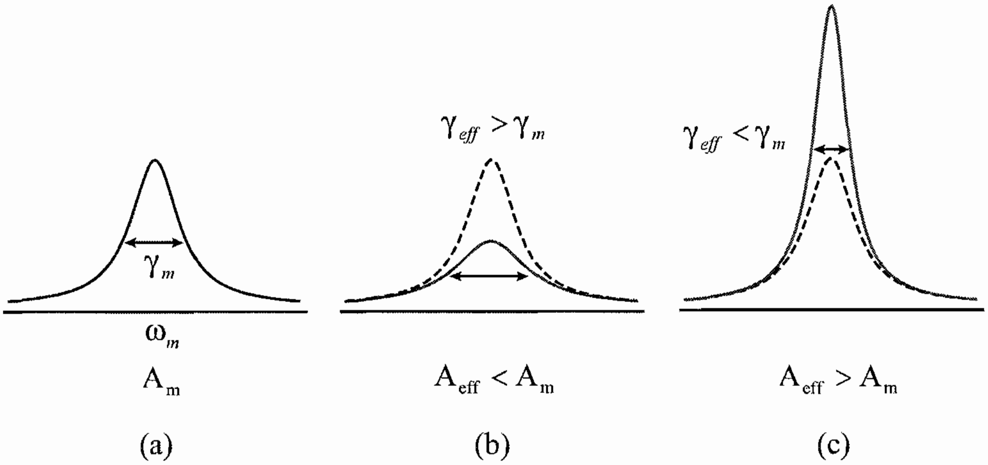

Figure 3.5: Schematic description of the displacement spectrum upon cooling or heating. (a) Intrinsic displacement spectrum. (b) Cooling of mechanical motion reflected in the area reduction along with linewidth broadening. (c) Heating of mechanical motion reflected in the area amplification along with linewidth narrowing. A_m and A_{eff} are intrinsic and effective spectral areas, respectively.

where

$$\begin{aligned} H_{cav} &= \hbar\omega_c a^\dagger a && (3.32)\\ H_m &= \hbar\omega_m a_m^\dagger a_m && (3.33)\\ H_{int} &= -\frac{\hbar\omega_c}{L}x = -\frac{\hbar\omega_c}{L}\sqrt{\frac{\hbar}{2m\omega_m}}(a_m^\dagger + a_m)a^\dagger a && (3.34)\\ H_{drive} &= \hbar E(a e^{i\omega_L t} + a^\dagger e^{-i\omega_L t}) && (3.35) \end{aligned}$$

H_{cav} and H_m describe the energy of the optical cavity mode and the mechanical mode, respectively. $a(a_m)$ and $a^\dagger(a_m^\dagger)$ are lowering and raising operators for the cavity (mechanical) mode, with $[a, a^\dagger] = [a_m, a_m^\dagger] = 1$. H_{int} is the optomechanical interaction term with an effective cavity length L. This length corresponds to an actual cavity length for a Fabry-Perot resonator and to a radius for a microsphere resonator. H_{drive} describes the cavity driving field with $E = \sqrt{\frac{\kappa P}{\hbar\omega_L}}$ where P is the input power.

By inspecting the interaction term, the radiation pressure coupling rate is given by $g_m = \omega_c \frac{\Delta x_0}{L}$, where Δx_0 is the zero-point amplitude. The smallness of $g_m \sim 10^3 (\ll \omega_c,\ \omega_m)$ in a microsphere optomechanical system allows us to treat the interaction term as a perturbation coupled to the system reservoir. For solving the quantum Hamiltonian of an optomechanical system, the master equation approach can be used in order to derive the evolution equation of the density matrix of the optomechanical system, where the optical cavity losses and the mechanical dissipation are included in the Lindblad form.

In steady-state, $\langle a_m^\dagger a_m \rangle_{SS}$ yields the final average phonon occupation number of a mechanical vibration [28, 29],

$$N_f = \frac{\gamma_m N_i + \Gamma_c N_Q}{\gamma_m + \Gamma_c} \tag{3.36}$$

with

$$N_Q = -\frac{4(\Delta\omega + \omega_m)^2 + \kappa^2}{16 \Delta\omega\ \omega_m} \tag{3.37}$$

N_i is the phonon occupation number determined by bath temperature, and for $N_i \gg 1$ Eq.(3.36) reduces to the classical regime where thermal dissipation of mechanical vibration is dominant. On the other hand, for small dissipation or high cooling rate, the final occupation reduces to N_Q, the shot noise limited phonon occupation number. The fluctuation of the intracavity power leads to the randomness of the radiation pressure force, and thus the mechanical motion is effectively heated. This random noise can arise from classical laser noise such as phase or intensity noise, but, in ideal conditions, the quantum nature of light is eventually responsible for this noise, which is referred to as quantum backaction. Note that N_Q is independent of the input power.

3.5 Resolved-Sideband Cooling

In Fig. 3.6(a), N_Q is plotted as a function of the laser detuning for different ratios of ω_m/κ, showing the minimum reachable phonon occupation number. When the detuning approaches zero, the occupation rapidly increases due to the increase in intracavity power. By differentiating Eq.(3.37) with respect to $\Delta\omega$, the minimum value of N_Q is obtained as,

$$N_Q = \frac{1}{2}\left(\sqrt{1+\frac{\kappa^2}{4\omega_m^2}}-1\right) \tag{3.38}$$

with a laser detuning $\Delta\omega_m = -\sqrt{\omega_m^2+\kappa^2/4}$. Depending on the ratio ω_m/κ, this expression falls into two regimes,

$$N_Q \approx \begin{cases} \dfrac{\kappa^2}{4\omega_m^2} \ll 1 & \text{for} \quad \omega_m \gg \kappa \\ \dfrac{\kappa}{4\omega_m} \gg 1 & \text{for} \quad \omega_m \ll \kappa \end{cases} \tag{3.39}$$

For $\omega_m \ll \kappa$ in the adiabatic limit, the final occupation prohibits from reaching the ground state cooling, yielding the effective temperature $T_{eff} \approx \dfrac{\hbar\kappa}{4k_B}$. This regime can be compared to the Doppler cooling limit of laser cooling of atoms. On the other hand, for $\omega_m \gg \kappa$ in the resolved-sideband limit, the final occupation number can be well below one, indicating that the quantum ground state can indeed be achieved. Figure 3.6(b) plots the photon occupation number as a function of effective damping rate. By increasing the effective damping rate or the input power, the occupation number starts to deviate from the classical regime where thermal dissipation is dominant, and finally converges to the quantum backaction limit Q_N, which is essentially well below one in the resolved-sideband limit.

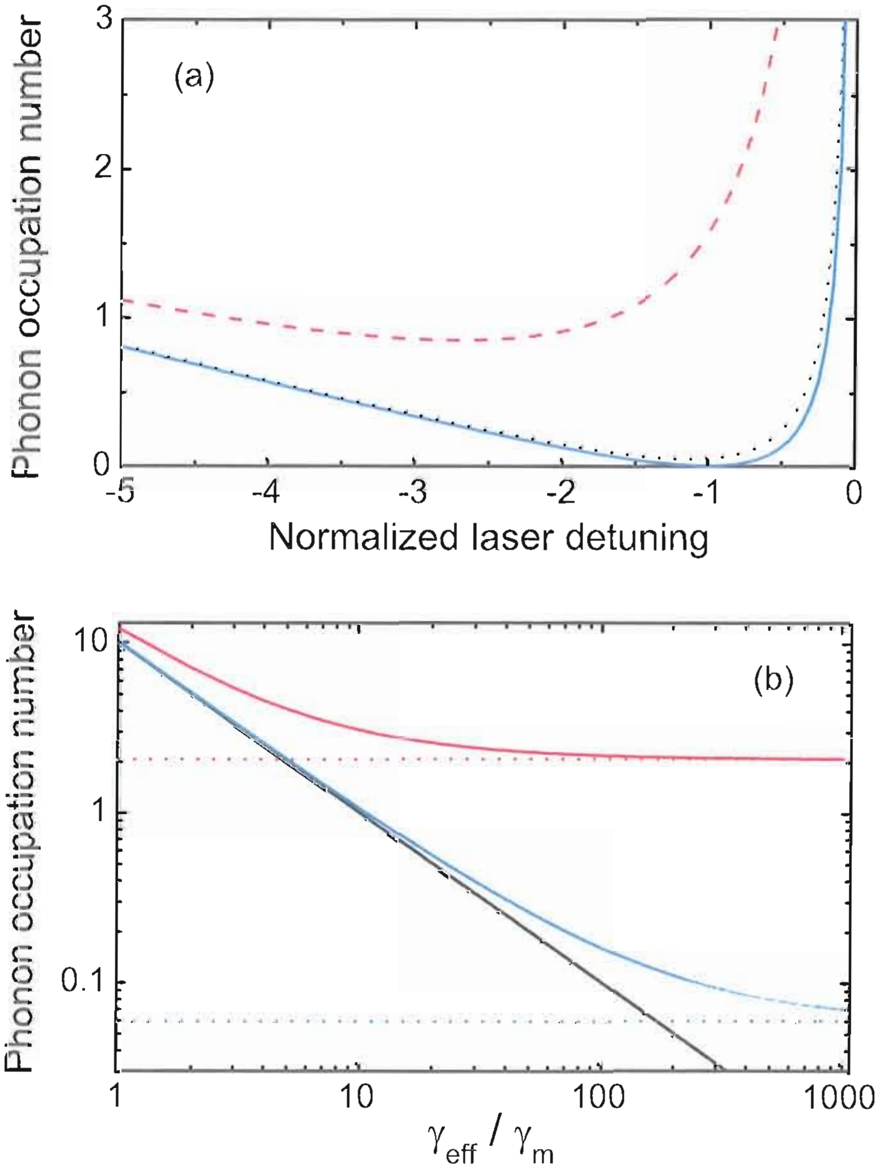

Figure 3.6: Average phonon occupation number achievable by radiation pressure cooling. (a) Quantum backaction limited final occupation number as a function of $\Delta\omega/\omega_m$ for different ratios of $\omega_m/\kappa = 0.2$, 1 and 5, from the top to the bottom curves. (b) Final phonon occupation N_f is plotted as a function of the effective damping rate, showing the transition from the classical region in the black line to the quantum region, $\omega_m/\kappa = 1$ in blue and $\omega_m/\kappa = 0.1$ in red. Only in the resolved-sideband limit, $N_f \ll 1$ is in principle achievable. A black curve represents the classical limit and dotted lines are asymptotic lines.

Although quantum theory predicts that ground state cooling is possible in the resolved-sideband cooling limit, it is only reachable when the classical limit is suppressed well below one, i.e, $N_i\gamma_m/\gamma_{eff} \ll 1$. Upon satisfying this condition, the final occupation can be arbitrarily small for large detuning $|\Delta\omega| = \omega_m \gg \kappa$. All we need to do is to increase the input power to keep a constant radiation pressure force. Large laser detuning has another benefit regarding to the absorption of the intracavity power, which is one of the heating sources which needs to be suppressed.

CHAPTER IV

EXPERIMENTAL TECHNIQUES AND CHARACTERIZATION

For experimental studies of the radiation pressure induced optomechanical coupling, which is theoretically described in the previous chapter, we develop and utilize a unique technique, the free-space evanescent excitation of WGMs in a deformed silica microsphere. While the incident angle of a WGM is conserved in regular microspheres, it no longer remains constant in deformed microspheres, leading to the changes in the emission pattern of WGMs. Compared to very weak and isotropic far-field emission of WGMs in regular microspheres, a deformed microsphere has unique properties of directional evanescent escape near the regions where the angle of incidence is close to the critical angle for the total internal reflection [66, 67]. Utilizing this fact, WGMs in deformed microspheres can be evanescently excited in free space, providing a simple, but useful way of WGM excitation [50, 68].

The scheme of free-space excitation of WGMs can be used simultaneously for high sensitivity homodyne detection of mechanical vibrations of the optomechanical resonator [44]. According to the equipartition theorem, the radial vibration amplitude of a silica microsphere with a 15 μm radius is about 10^{-14} m at room temperature, which is four orders of magnitude smaller than the atomic Bohr radius. Thus, studies of optomechanical cooling of the thermal vibrations require extremely high readout sensitivity of the mechanical displacement [69] as well as efficient cooling mechanism.

For light circulating in a WGM, thermal mechanical vibrations induce a phase shift, which is proportional to the mechanical displacement. The optical interferometric measurements of the induced phase shift provide a highly sensitive measure of the mechanical displacement. In the free-space excitation configuration, the part of the excitation laser beam that is not coupled to WGMs provides a local oscillator for the homodyne interferometric detection of the mechanical displacement [41, 44].

For the calibration of the measured displacement spectrum, the excitation laser is phase-modulated in order to mimic the phase shift induced by mechanical vibration [27]. This phase modulation generates a reference spectral peak, providing direct comparison between phase shifts due to the mechanical vibration and the phase-modulated laser. The cavity emission and the local oscillator take the same optical path to the detector in free-space configuration and thus this calibration scheme is independent of the cavity decay rate, the mode matching efficiency and the free-space excitation efficiency.

In this chapter, we will discuss the free-space evanescent excitation of WGMs in a deformed microsphere. Based on this scheme, we will discuss the homodyne detection and the calibration of mechanical vibrations of a silica microsphere resonator, both in theory and experiment. We will also present and discuss the experimental observations of the radiation pressure induced optomechanical cooling and heating, including parametric instabilities in our optomechanical system. Radiation pressure effects will be further manifested by detailed studies about the dependence of the effective mechanical frequency and linewidth on the laser detuning as well as the input power.

4.1 Free-Space Excitation of WGMs

4.1.1 Launching of Whispering Gallery Modes

Although the WGMs in a microsphere feature excellent optical properties such as ultrahigh optical Q-factor and small mode volume, excitation of WGMs is not trivial. In the case of a Fabry-Perot resonator, the excitation laser is aligned along the axis connecting centers of two mirrors, which normally makes the excitation beam mode-matched with the optical modes. However, in a microsphere, the light that enters the resonator should leave from the microsphere by refraction. Although it is not impossible to excite a WGM by focusing a laser beam near the microsphere surface, this excitation scheme is not effective. This fact, on the other hand, explains the ultrahigh optical Q-factor in the WGMs. However, in an asymmetric microsphere, free-space coupling efficiency can be profoundly improved.

WGMs can be efficiently excited by generating an evanescent field near the microsphere, which is mode-matched to the relevant WGM [62]. For this purpose, an optical coupler, such as a high index prism [53] or a tapered fiber is normally used [70]. As shown in Fig. 4.1(a), light can propagate from the prism into the microsphere across a sub-μm gap via the frustrated total internal reflection. By changing the incident angle of the prism, different radial modes can be selectively excited. Another way to excite the WGMs is to use a tapered fiber of a few μm in size, which is fabricated by stretching a single mode optical fiber while applying a torch or a CO_2 laser. When light propagates through the tapered fiber, a large portion of light overfills the fiber waveguide, generating an evanescent field. In this configuration, the mode-matching between the excitation and a WGM is almost perfect, and the WGM can be excited with nearly 100 % efficiency [71]. For both a high index prism and a tapered fiber, the gap between the microsphere surface and the coupler should be

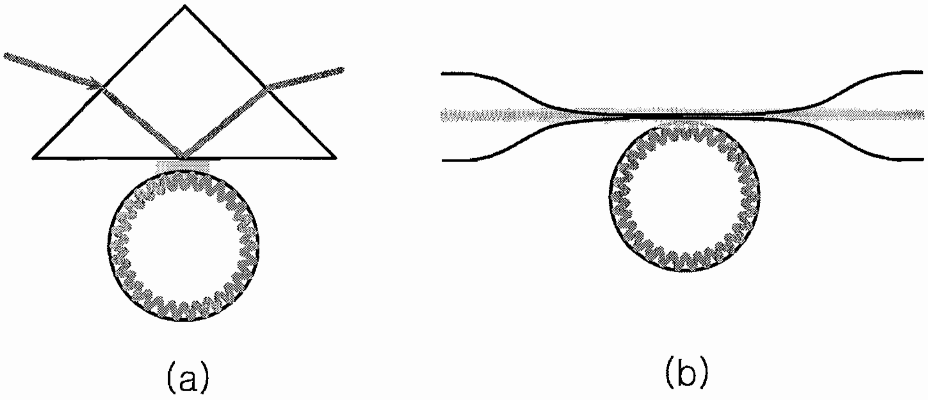

Figure 4.1: Excitation of WGMs in a microsphere. (a) The frustrated total internal reflection in a high index prism and (b) the spatial extension of a single mode near a tapered fiber are used to generate an evanescent field near the microsphere for the excitation of the WGMs.

within a wavelength because the evanescent field decays exponentially beyond the coupler's boundary.

High efficiency of coupling-in also means high efficiency of coupling-out from the resonator, leading to optical energy loss in WGMs. Considering the loss due to the coupling, the total Q-factor, Q_{tot}, becomes,

$$Q_{tot}^{-1} = Q_0^{-1} + Q_c^{-1} \tag{4.1}$$

where Q_0 is an intrinsic quality factor and Q_c is the quality factor associated with the coupling. Because the coupling efficiency is sensitive to the gap in a prism or a tapered fiber coupling, Q_c and accordingly Q_{tot} have a strong dependence on the gap.

In order to describe the coupling efficiency of the WGMs, impedance matching should be considered. This terminology originates from the issue of power transfer in an electrical circuit. When two electrical devices have the same impedance, the electrical power can be effectively transferred without reflection or loss. In excitation of the WGMs, the mode-matched optical field can be completely coupled into the microsphere when the intrinsic loss is matched with the coupling loss. In this case, the resonance dip in optical transmission can go to zero, and the optical power coupled into the resonator dissipates within the resonator. This is called critical coupling, which has been demonstrated with a tapered fiber coupler. The fractional dip in the optical transmission, K, is given by [62],

$$K = 4\Gamma^2 \frac{Q_0 Q_c}{(Q_0 + Q_c)^2} \tag{4.2}$$

where Γ is a mode matching coefficient. When $Q_0 = Q_c$, K is equal to 1 with $\Gamma = 1$.

4.1.2 Evanescent Escape in a Deformed Microsphere

When a ring resonator is deformed, the angle of incidence is no longer conserved during the propagation along the circumference. Optical properties of an asymmetric resonator have been extensively studied both in theory and experiment, including a deformed silica microsphere. One of the unique properties is directional cavity emission when the incident angle is close to the critical angle for total internal reflection.

Figure 4.2 shows the scanning electron microscope (SEM) images of a deformed microsphere taken along three orthogonal directions. On the equatorial plane, one axis is elongated, showing a reflection symmetry about each axis. The deformation of a deformed microsphere, ϵ, is defined as,

$$\epsilon = \frac{a - b}{a} \tag{4.3}$$

where a and b are the long and short axis on the equator plane, respectively, as shown in Fig. 4.2(d). In fabrication, which will be discussed in detail later, the deformation,

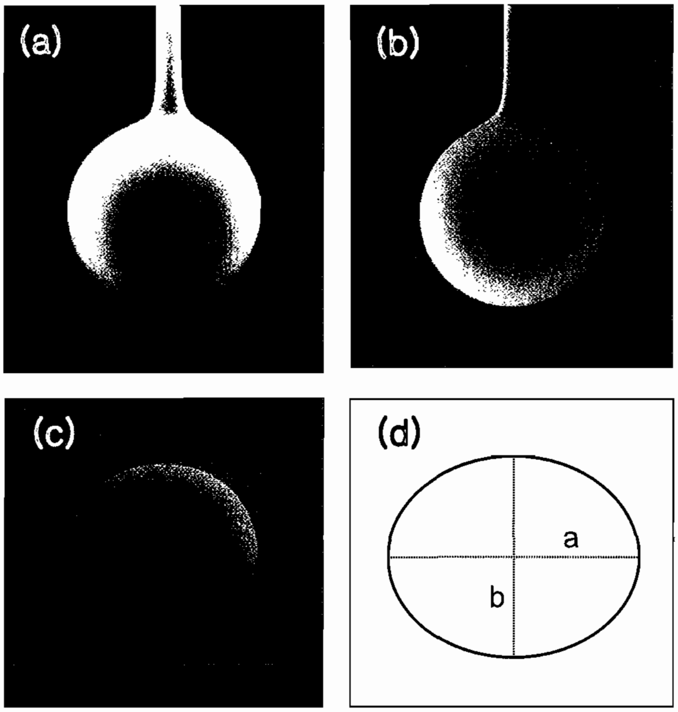

Figure 4.2: (a) $\sim$ (c) Scanning electron microscope images of a deformed microsphere taken along three orthogonal directions. Average diameter is 32.6 μm and deformation is $\epsilon = 4.9$ %. (d) A long axis a and a short axis b in an elliptical shape.

ranging from 1 % to 10 %, is precisely controlled with 1 % accuracy by repeated heating with a CO_2 laser.

Previous studies [66, 67] have shown that there are two different regimes for the directional emission in deformed microspheres, depending on the deformation. For large deformation, the WGMs with low optical Q-factors escape refractively when the angle of incidence is smaller than the critical angle. However, for a small deformation below 2 %, the evanescent escape is dominant with high optical Q-factors. This behavior can be explained by the effective potential of WGMs. When the angle of incidence approaches the critical angle, the potential barrier gets relatively thinner, and the chances that a WGM field tunnels through this barrier grows exponentially.

Theoretical works show that the regions with minimal incident angles in the deformed microspheres are located near 45 degrees away from a long or short axis. In these regions, WGMs can evanescently escape along with ultrahigh Q-factors.

4.1.3 Free-Space Evanescent Excitation of WGMs in a Deformed Microsphere

By utilizing directional evanescent escape, the WGMs in deformed silica microspheres can be effectively excited in free space without using any coupler [50, 52]. A light path is reversible. Thus, a laser beam can be evanescently coupled into the microsphere resonator through the evanescent escape regions. In order to demonstrate free-space excitation, a laser beam is focused near one of these regions 45 degrees away from a short or a long axis, as schematically shown in Fig. 4.3. The relative position between a focused beam and a microsphere surface is precisely adjusted in order to obtain the optimal excitation.

For the excitation of WGMs, we use two lasers, a diode laser (New Focus 6316) and a Ti:sapphire ring laser (Coherent 899-21), operating near $\lambda \sim 800\,nm$. The diode laser with a scan range over 20 nm is used to test excitation of WGMs and locate WGM resonances in free-space coupling. In order to resolve the ultrahigh Q-factor WGMs, the ring laser whose frequency is stabilized with an external reference cavity is used. These two lasers are aligned such that they are easily switched with a single flipping mirror.

Free-space excitation of WGMs relies not only on the fabrication of the deformed microspheres, but also on beam focusing. For optimal focusing, the laser beam is expanded and collimated with two different focal length lenses in order to fill the entire objective aperture. a high magnification lens can provide a focused spot size down to a refraction limit, but for the practical reasons when using a cryogenic

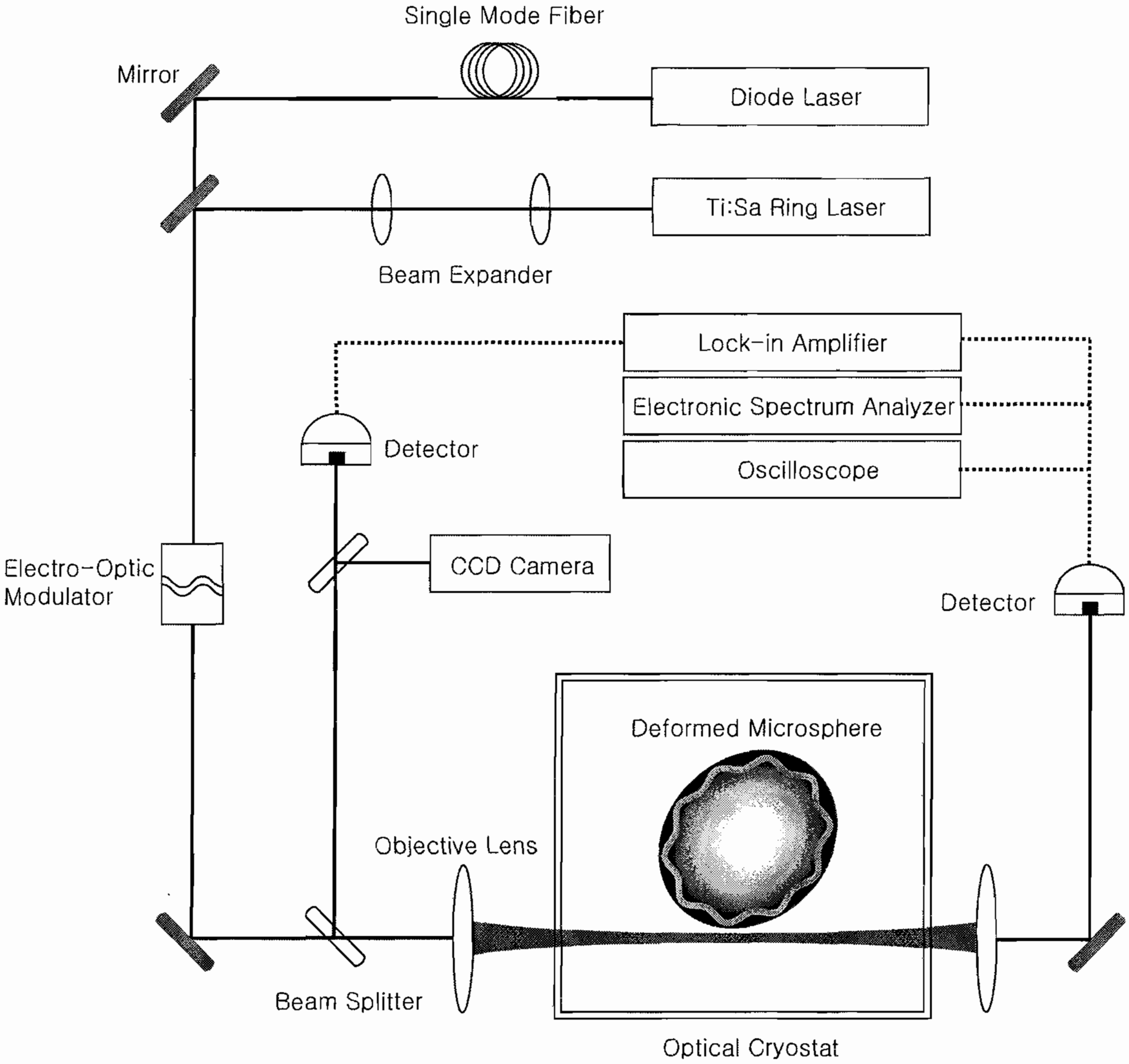
Single Mode Fiber
Mirror
Diode Laser
Ti:Sa Ring Laser
Beam Expander
Lock-in Amplifier
Electronic Spectrum Analyzer
Oscilloscope
Detector
Electro-Optic Modulator
CCD Camera
Detector
Deformed Microsphere
Objective Lens
Beam Splitter
Optical Cryostat

Figure 4.3: Experimental setup of free-space evanescent excitation of WGMs and optical detection of mechanical vibrations of a deformed microsphere. An electro-optic modulator is used for the calibration of mechanical displacement and a liquid helium cryostat is used for cryogenic operation.

system, a lens with a long walking distance must be used. A 10× objective lens with 33.5 *mm* working distance is chosen to focus the excitation laser and has been used throughout this dissertation.

The Microsphere is imaged along the direction of incoming laser onto a CCD camera through the same focusing lens followed by a beamsplitter. With this imaging system, the position of the focused beam near the microsphere is adjusted for optimal excitation of WGMs, and the free-space evanescent excitation of the WGMs are monitored. This also allows us to monitor degradation of optical Q-factor due to any contamination.

In order to measure WGMs, the optical transmission is collected with another objective lens after the microsphere, and focused onto a silicon photodiode. For lock-in detection, the excitation laser is modulated with a mechanical chopper which provides a reference frequency to the Lock-in amplifier. When an excitation laser scans over a WGM, the optical transmission decreases, resulting in a dip with an inverse Lorentzian lineshape. WGMs are also measured in the backward direction through the same focusing lens. In this case, the backscattered modes are measured nearly background free by isolating the optical emission with a spatial filter consisting of one pair of lenses and a pin hole.

Experimental setup for free-space evanescent excitation of WGMs in deformed microspheres can be simultaneously used for studies of optomechanical coupling. For the measurement of the mechanical vibrations, the optical transmission is collected and focused onto a photodiode in the same way as when measuring WGMs, but without modulation of the excitation power. Because of the ultrasonic frequencies above 100 MHz for the mechanical vibrations in a silica microsphere, a high speed photodetector (NewFocus Model 1801, AC-coupled) with a 125 MHz bandwidth is used. The photodetector output is sent either to an electric spectrum analyzer

(0.1 MHz – 1.5 GHz) to measure the mechanical spectrum or to an oscilloscope to measure the mechanical vibration in the time domain.

The optical images in Fig. 4.4 show the onset of a WGM in a deformed microsphere through the free-space excitation. When the laser is on the cavity resonance, a strong emission of the WGM in Fig. 4.4(a) appears on the microsphere surface. For comparison, the image shown in Fig. 4.4(b) is taken when the laser is off-resonant with a WGM. Due to the finite size of a focused beam, a small portion of the excitation laser is scattered by the deformed microsphere, resulting in a weak light-scattering on the opposite side of the focused beam.

The behavior of free-space evanescent excitation is similar to the evanescent excitation of WGMs with a tapered fiber except for two main differences. First of all, the free-space excitation process does not lead to additional degradation of the optical Q-factor. Secondly, the free-space excitation efficiency is in part limited by the imperfect mode matching between the incident laser beam and the relevant WGM. Figure 4.5(a) shows the transmission spectra obtained near a WGM resonance for a deformed microsphere with $D = 30$ μm and deformation near 4 %. The background level for each distance changes due to the diffraction of the excitation laser by a microsphere. The top curve in Fig. 4.5(a) is obtained when the microsphere is completely out of the focused beam. It shows no transmission dip, implying no excitation of a WGM. Note that the linewidth of the resonance remains unchanged for different distances between the laser spot and the microsphere surface. This fact indicates that the free-space excitation induces no degradation on the optical Q-factor, as expected. However, the relative depth or the fractional dip of the transmission resonance depends sensitively on the position of the laser focal spot. The fractional dip with respect to background level with no coupling is measured as a function of the distance in Fig. 4.5(b). The maximum fractional dip observed exceeds 50 % [44].

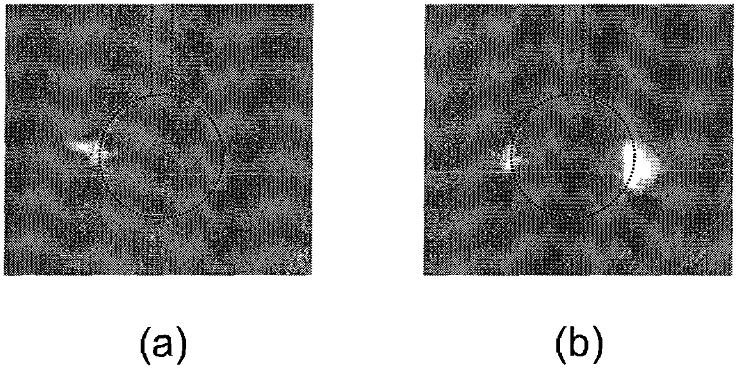

Figure 4.4: Free-space evanescent excitation of WGMs in a deformed microsphere. Optical images of a WGM excitation taken when the laser is (a) off-resonant and (b) on-resonant. These images are taken with the same objective lens used for focusing the excitation laser. A small portion of excitation laser scattered by a microsphere is observed on the left-side of the microsphere. Dotted lines representing a deformed microsphere and a fiber stem are a guide for the eye.

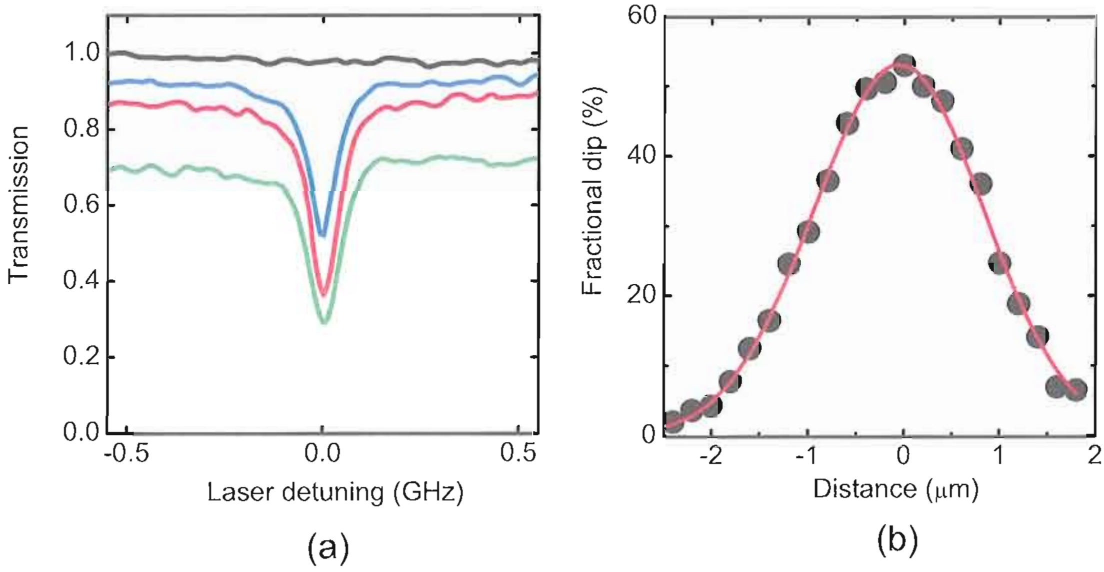

Figure 4.5: (a) Transmission spectrum near a WGM resonance obtained with free-space excitation for different distances between the focused beam and the microsphere surface. From top to bottom, the distance are $-2.4\ \mu m$, $-0.6\ \mu m$, $0\ \mu m$ and $0.6\ \mu m$, respectively. (b) Fractional dip obtained from the transmission spectrum as a function of distance. The solid line is a Gaussian fit, showing a full width at half maximum of $1.8\ \mu m$. Note that we set the position of maximum fractional dip as the zero distance.

The full width at half maximum of the gauss fit in Fig. 4.5(b) implies the focused beam spot of $1.8\ \mu m$ assuming that the skin depth of the WGMs beyond the surface is much smaller than the focused spot size.

The optical Q-factors of the WGMs in deformed microspheres via the free-space evanescent excitation can be expressed as,

$$Q^{-1} = Q_0^{-1} + Q_d^{-1} \tag{4.4}$$

where Q_0 is the intrinsic optical quality factor and Q_d is associated with the coupling in a deformed microsphere. Through the free-space excitation, the optical Q-factors in a deformed microsphere are observed to be in the range of $Q = 10^6 \sim 10^8$, depending on the deformation. If we assume that the cavity loss is entirely due to output coupling along the four emission directions, perfect mode matching between the incident laser beam and the relevant WGM should lead to a fractional dip of 75 %. A mode matching coefficient of 0.6 will lead to a fractional dip near 50 %. For silica microspheres with smaller deformation, the fractional dip observed is considerably smaller. For these spheres, cavity losses other than those due to the output coupling become important.

Fig. 4.6 shows the structure of WGM spectra obtained via free-space excitation. Figure 4.6(a) and (b) are wide range spectra scanned with a diode laser, and Fig. 4.6(c) is a high resolution spectrum scanned with a frequency-stabilized ring laser. Its spectral linewidth is $\leq$ 0.5 MHz. A coarse scan clearly reveals the free spectral range of 4.9 nm, which gives a microsphere diameter of $D = 28\ \mu m$ from Eq.(2.15). Within each free spectral range, a series of spectral peaks are observed. These equally spaced peaks arise from azimuthal symmetry breaking and each WGM has nearly the same optical Q-factor. A single WGM is further resolved in Fig. 4.6(c) and the linewidth from a Lorentz fit is 4 MHz, which is corresponding to $Q = 1.2 \times 10^8$. The WGM spectra in Fig. 4.6 are measured by detecting the counterclockwise modes that arise due to the backscattering. These modes are monitored through a focusing lens followed by a beam splitter and can be measured nearly background free.

The free-space evanescent excitation of the WGMs provides a unique tool for experimental studies with a silica microsphere resonator in a cryogenic environment. Although the silica microsphere or microtoroid features the best optical properties among the microresonators, these resonators have been rarely used at low temperature because of technical difficulties in implementing the microresonator and in controlling the distance between the resonator and the coupler. By utilizing free-space excitation, we have been able to carry out deformed microsphere based experimental studies at cryogenic temperature, including cavity-QED and optomechanical cooling.

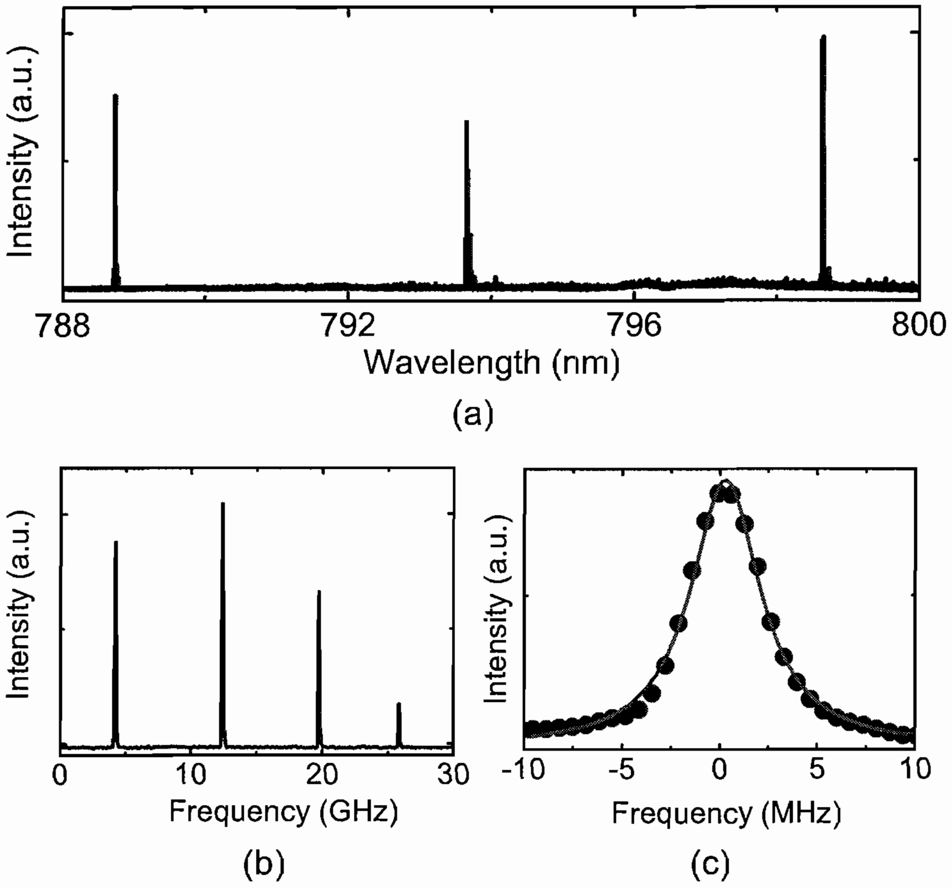

Figure 4.6: WGM structure of a deformed microsphere obtained from free-space excitation. (a) A wide range scan reveals the free spectral range of 4.9 *nm*, which corresponds to a microsphere diameter of 28 μm. (b) A series of spectral peaks within one spectral range are due to the azimuthal symmetry breaking. Spectral separation is about 8.2 GHz. (c) A fine scan resolves the ultrahigh optical Q-factor of a WGM. A Lorentz fit (solid line) gives a linewidth of 4 MHz, which yields $Q = 1.2 \times 10^8$.

4.1.4 Fabrication of Silica Microspheres

Silica microspheres are fabricated by melting an optical fiber with a CO_2 laser [72]. We have used a multimode fiber with a core refractive index $n = 1.457$, a 200 μm diameter and the attenuation below 10 dB/km at $\lambda = 800$ nm. In order to have uniform refractive index through the whole microsphere, only the core of the multimode fiber has been used for fabrication. After removing the fiber jacket, the optical fiber is installed into a fiber chuck, and then a small weight is attached to one end of the fiber. The fiber chuck is mounted on a 3D stage for fine positioning. A CO_2 laser is focused with a 1 inch focal length ZnSe lens. A CCD camera is placed at a right angle with respect to the CO_2 laser beam path, and a 50× objective lens is used for monitoring the fabrication process. When the focused CO_2 laser is brought toward the optical fiber, the heated part of fiber starts to be melted and stretched due to the weight. Once the desired length and diameter of stretched fiber is obtained, the weight is cut easily by increasing laser power or bringing the beam focus further more into the optical fiber. The remaining part of the optical fiber is now heated with a relatively high laser power and becomes spherical through surface tension. The stem size is usually kept less than one fifth of the microsphere diameter, but for the optomechanical cooling experiment it is kept as small as one tenth in order to achieve high mechanical quality factors. Although fabricated microspheres are very close to spherical in shape, they are slightly elongated along the vertical direction due to the fiber stem and the gravitational pulling.

For the fabrication of deformed microspheres, we have tested two different methods; fusing two microspheres [66] and pulsing a CO_2 [68] laser on a single microsphere. For the fusing method in Fig. 4.7, two regular microspheres of similar size are separately fabricated by following the procedure as described above. Then,

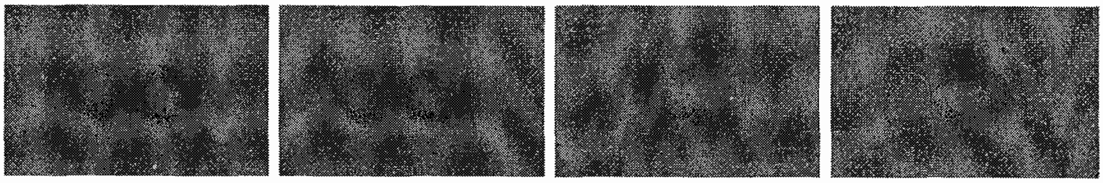

Figure 4.7: Fabrication procedure of a deformed microsphere by fusing two regular microspheres with similar sizes. The final deformation is controlled by repeated heating.

two microspheres each mounted on a 3D stage are brought together to slightly make contact near equator planes. The first microsphere is placed upward, while the second microsphere is in the normal position. The line connecting the centers of two microspheres should be aligned along the direction of the CO_2 laser. By applying slight heat, the regions in contact are fused and then the stem of the second microsphere is cut by using the laser beam. Now, relatively high laser power is applied to fuse them together until they are completely immersed in each other. The deformation is controlled by repeated heating.

For the pulsing method, a single microsphere is prepared first. Then, a CO_2 laser pulse with a high power but a short duration time is applied onto the microsphere. The pulsing of a CO_2 laser is externally controlled with a function generator. Because of the short duration time, about a few μs, the absorbed heat melts only the one side that is exposed to the laser. At the same time, the laser beam pressure also pushes this side, resulting in a deformed curvature. After a 180 degree rotation of the microsphere, applying another pulse leads to a deformed microsphere with two symmetric axes. In the pulsing method, it is important to have a microsphere exactly in the center of the beam path to prevent any distortion due to misalignment.

Both methods for the fabrication of deformed silica microspheres work nicely. However, we usually find that the excitation of the WGMs in the free-space coupling is more efficient for the microspheres fabricated with the fusing method than with the pulsing method. Because of the need of the control on the deformation as well as high coupling efficiency, the fusing of two microspheres method has been used through all the experimental studies of optomechanical coupling.

4.2 Homodyne Interferometric Detection of Mechanical Vibrations

4.2.1 Direct Homodyne Detection

In the free-space excitation configuration, as shown in Fig. 4.8, the part of excitation laser beam that is not mode-matched with the relevant WGM passes by the deformed microsphere without coupling into the resonator. The uncoupled laser beam provides a local oscillator for interferometric homodyne detection of the mechanical displacement. In this direct homodyne detection, the relative phase between the cavity emission and the local oscillator remains unchanged after the microsphere because both beams travel the same optical path all the way to the photodiode.

Consider a simple harmonic motion of the radial displacement in the equatorial plane with well-defined phase and amplitude $r = r_0 \sin \omega_m t$ with a radial amplitude, r_0, and a mechanical vibration frequency, $\omega_m/2\pi$. Then, the equations for the intracavity field E_{cav} and the transmission field E_{out} are, respectively,

$$\begin{aligned} \frac{d}{dt}E_{cav} &= \left[-\frac{\kappa}{2} + i\left(\Delta\omega - \frac{r_0\omega_0}{R}\sin\omega_m t\right)\right]E_{cav} + \frac{it}{T_{rt}}\Gamma E_{in} && (4.5) \\ E_{out} &= rE_{in} + itE_{cav} && (4.6) \end{aligned}$$

where κ is a cavity decay rate, it and r are the transmission and the reflection coefficient, respectively. $T_{rt} = 2\pi nR/c$ is a round-trip time, R is a microsphere radius, n is the refractive index of silica, c is the speed of light in vacuum, and $\Delta\omega = \omega_L - \omega_c$ is a laser detuning. ω_L and ω_c are angular frequencies of the incident

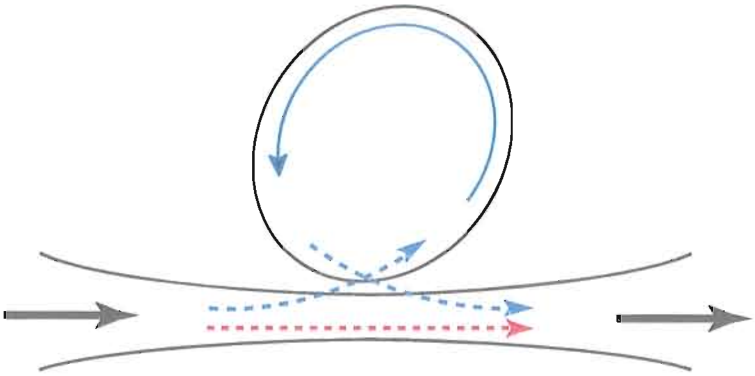

Figure 4.8: Schematic of interferometric homodyne detection of mechanical displacement in free-space evanescent excitation of WGMs in a deformed microsphere. The uncoupled part (red dash) of excitation beam that provides a local oscillator is recombined with the cavity output (blue dash) after the microsphere.

laser and the cavity resonance, respectively. $\Gamma(\leq 1)$ is a mode-matching coefficient, which is equal to 1 for perfect mode-matching such as a tapered fiber coupling. In free-space excitation, the value of Γ can be higher than 0.6 as discussed before. However, in studies of optomechanical cooling in the resolved-sideband limit, this value is about a few percent due to the low excitation efficiency accompanied by the ultrahigh Q-factor.

Eq.(4.5) is an ordinary first order differential equation and the solution can be formally found as,

$$E_{cav}(t) = \frac{C_1}{\mu(t)} \int \mu(t) dt \tag{4.7}$$

with

$$\mu(t) = C_2 e^{(\frac{\kappa}{2} - i\Delta\omega)t - i\alpha \cos \omega_m t} \tag{4.8}$$

where C_1 and C_2 are constants, and $\mu(t)$ is called an integration factor. In order to perform the integration in Eq.(4.7), it is convenient to expand the exponential term,

$e^{i\alpha\cos\omega_m t}$, as a series of Bessel function (J_n) by using Jacobi-Anger expansion,

$$e^{iz\cos\theta} = \sum_{n=-\infty}^{\infty} i^n J_n(z) e^{in\theta} \tag{4.9}$$

This identity is equivalent to the expansion of a plane wave in a series of cylindrical waves. The integration in Eq.(4.7), with a help of Eq.(4.9), yields an analytic form of $E_{cav}(t)$ as [27],

$$E_{cav}(t) = \frac{it\Gamma E_{in}}{T_{rt}} \sum_{n=-\infty}^{\infty} \sum_{m=-\infty}^{\infty} \frac{i^{-n+m} J_n(\alpha) J_m(\alpha)}{\frac{\kappa}{2} - i(\Delta\omega - n\omega_m)} e^{i(n+m)\omega_m t} \tag{4.10}$$

where we use a dimensionless parameter $\alpha = \dfrac{r_0\omega_c}{R\omega_m}$, which is usually found to be $< 10^{-3}$ for a microsphere optomechanical system. Due to the smallness of α, by including the leading terms, to the first order of α in the Bessel expansion, Eq.(4.10) becomes,

$$\begin{aligned} E_{cav}(t) \simeq \frac{it\Gamma E_{in}}{T_{rt}} \Bigg[& \frac{1}{\kappa/2 - i\Delta\omega} + \frac{\alpha^2/4}{\kappa/2 - i(\Delta\omega - \omega_m)} + \frac{\alpha^2/4}{\kappa/2 + i(\Delta\omega - \omega_m)} \\ & + \left(\frac{i\alpha/2}{\kappa/2 - i\Delta\omega} - \frac{i\alpha/2}{\kappa/2 - i(\Delta\omega - \omega_m)} \right) e^{i\omega_m t} \\ & + \left(\frac{i\alpha/2}{\kappa/2 - i\Delta\omega} - \frac{i\alpha/2}{\kappa/2 - i(\Delta\omega + \omega_m)} \right) e^{-i\omega_m t} \Bigg] \end{aligned} \tag{4.11}$$

Here, $J_0(\alpha) \simeq 1$ and $J_1(\alpha) \simeq \dfrac{\alpha}{2}$ for $\alpha \ll 1$, and $J_{-n} = (-1)^n J_n$ are used for the calculation. By putting $E_{cav}(t)$ in Eq.(4.11) into Eq.(4.6), we can directly obtain $E_{out}(t)$. After some algebra, the transmitted optical power $P_{out}(t)$ normalized by the input power P_{in} is calculated as,

$$\frac{P_{out}}{P_{in}} = \left|\frac{E_{out}}{E_{in}}\right|^2 = \left|1 - \frac{t^2\Gamma/T_{rt}}{\kappa/2 - i\Delta\omega}(1 + H(\Delta\omega;t))\right|^2 \tag{4.12}$$

$$H(\Delta\omega;t) \equiv \frac{\alpha\omega_m}{2}\left(\frac{e^{-i\omega_m t}}{\kappa/2 - i(\Delta\omega + \omega_m)} - \frac{e^{i\omega_m t}}{\kappa/2 - i(\Delta\omega - \omega_m)}\right) \tag{4.13}$$

up to the first order of α in $H(\Delta\omega;t)$. The laser detuning dependence appeared in the denominator of $H(\Delta\omega;t)$ implies the resonant response of the $P_{out}(t)$ at $\Delta\omega = \pm\omega_m$ as a result of parametric optomechanical process. Now, it is convenient to separate the optical transmission spectrum into two parts, a stationary part (DC) and a modulated part (AC) oscillating at a frequency $\omega_m/2\pi$, which are, respectively,

$$P_{out,DC} = P_{in}\left(1 - \frac{4\kappa^2}{\kappa^2 + \Delta\omega^2}(\eta - \eta^2)\right) \tag{4.14}$$

$$P_{out,AC} = P_{in}\frac{4\kappa^2}{\kappa^2 + \Delta\omega^2}\left((2\eta^2 - \eta)\mathrm{Re}H(\Delta\omega;t) + 2\eta\frac{\Delta\omega}{\kappa}\mathrm{Im}H(\Delta\omega;t)\right) \tag{4.15}$$

Here, we introduce a coupling coefficient of the free-space excitation defined as $\eta \equiv \Gamma T^2/T_{rt}\kappa$. Note that T^2/T_{rt} is a coupling loss($= \kappa_c$) associated with the microsphere deformation. The DC part in Eq.(4.14) represents a transmission dip near a cavity resonance that provides a measure of the coupling coefficient through a relation, $K = 4\eta(1-\eta)$, where K is a fractional dip. The linewidth of the transmission dip gives a total cavity decay rate. When $\eta = 1/2$, the fractional dip reaches one, implying a critical coupling. However, the maximum fractional dip obtainable will be limited to 0.75 assuming four symmetric emissions in a deformed microsphere. The AC part describes the intensity modulation in the transmission due to the mechanically induced phase change. In Eq.(4.15), higher harmonic terms in ω_m are neglected.

In Fig. 4.9, the AC amplitude normalized to input power is plotted as a function of laser detuning for different ratios of ω_m/κ. We assume there is no heating or cooling effect due to optomechanical coupling and thus the radial amplitude r_0 remains constant. The AC response is symmetric for blue and red detuning, and goes to zero at zero detuning where the Stokes and the anti-Stokes emission are completely balanced. For a small ratio of ω_m/κ in the top graph in Fig. 4.9, the AC response is optimized at $\Delta\omega \simeq \pm\kappa/2$ and gradually decreases for a large laser detuning. As the ratio of ω_m/κ increases, additional peaks in the AC response appear at $\Delta\omega \simeq \pm\omega_m$. These peaks are resonantly enhanced emissions of the Stokes for blue detuning and the anti-Stokes for red detuning. Although the laser detuning is completely off-resonance in the bottom graph in Fig. 4.9, the AC response at sideband detuning is as high as that at $\Delta\omega \simeq \pm\kappa/2$. The ratio of $\omega_m/\kappa = 10$ indicates that only less than 1% of input power is coupled into the microresonator at $\Delta\omega \simeq \pm\omega_m$. The width of these peaks is the same as a cavity linewidth. This behavior of AC response indicates that, for the resolved-sideband cooling of a microresonator, the excitation laser should be detuned at $\Delta\omega = -\omega_m$ for the maximum cooling and at the same time for the maximum readout sensitivity.

4.2.2 Measurement Sensitivity

Displacement readout obtained from the AC response in transmission shows a strong dependence on the laser detuning. In the resolved-sideband limit, which is our focus, the AC amplitude in Eq.(4.15) with a laser detuning $\Delta\omega = \pm\omega_m$ yields,

$$P_{out,AC} = 8\eta \frac{r_0\omega_c}{R\omega_m} \frac{1}{4 + (\kappa/\omega_m)^2} P_{in} \tag{4.16}$$

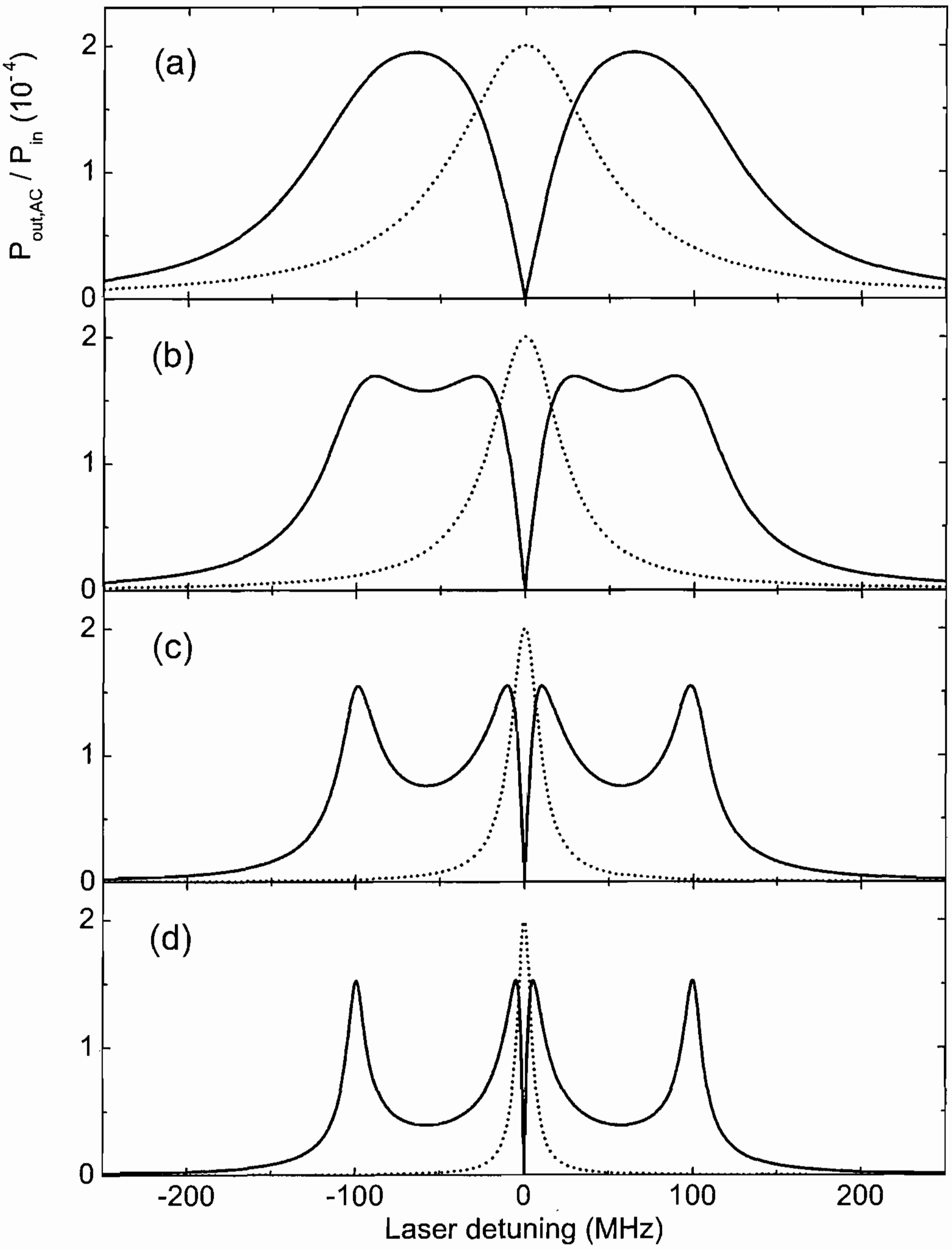

Figure 4.9: Theoretical calculations of the AC amplitude normalized (Solid lines) to the input power as a function of laser detuning with $\omega_m/2\pi = 100$ MHz. Dotted lines denote cavity resonance with different linewidths (a) $\kappa/2\pi = 100$ MHz, (b) $\kappa/2\pi = 50$ MHz, (c) $\kappa/2\pi = 20$ MHz and (d) $\kappa/2\pi = 10$ MHz. Values for $r_0 = 10^{-14}$ m, $R = 15$ μm, $\lambda = 790$ nm and $\eta = 0.03$ are used for this calculation.

Due to the small coupling efficiency and the off-resonance laser detuning in the resolved-sideband limit, the input laser power sets the shot noise level as $\sqrt{2\hbar\omega_c P_{in}}$. Therefore, assuming shot noise overwhelms any other noises in electric equipments, the measurement sensitivity is calculated as,

$$r_{min} = \frac{R\omega_m}{8\eta\omega_c}\sqrt{\frac{2\hbar\omega_c}{\eta_D P_{in}}}\left(4 + (\kappa/\omega_m)^2\right) \tag{4.17}$$

where η_D is a detector efficiency. For the parameters of $R = 15\ \mu m$, $\omega_m/2\pi =$ 120 MHz, $\eta = 0.03$, $\lambda = 790\ nm$, $\eta_D = 0.5$ and $P_{in} = 1\ mW$, the sensitivity of the displacement measurement reaches $r_{min} = 2.2 \times 10^{-18}\ m/\sqrt{Hz}$. This corresponds to a minimal detectable amplitude $\approx 2.2 \times 10^{-16}\ m$ for a mechanical vibration with $Q_m = 10,000$.

4.2.3 Observation of Mechanical Vibrations

The power spectrum of the optical transmission, in which mechanical vibrations are imprinted, is measured through free-space excitation. An excitation far below the threshold input power P_{th} for parametric instability is used and thus any heating or cooling from optomechanical coupling is negligible. Figure 4.10 shows an example of the noise power spectrum of the mechanical vibrations taken by an electronic spectrum analyzer. The three discrete peaks observed originate from fundamental mechanical vibrations of a deformed microsphere, and there are no other sources that can give rise to ultrasonic frequencies in the experimental setup. By comparing the observed spectrum with finite element analysis, these modes are identified as the first three radial breathing modes with $(n, l) = (1, 2)$, $(1, 0)$ and $(1, 4)$, respectively. These modes are optically visible because their vibration spatial shapes modulate cavity path length in the equatorial plane. The insets show the corresponding vibration

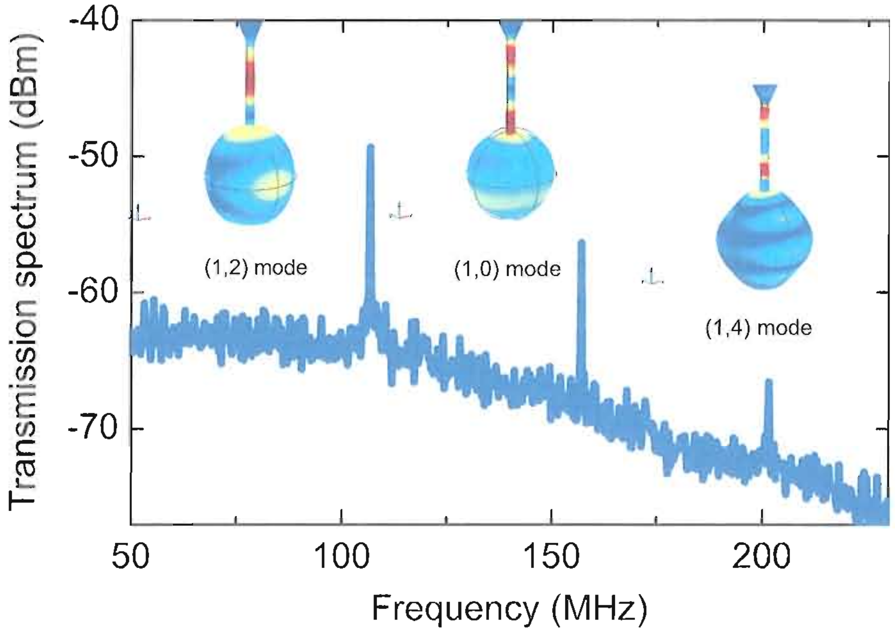

Figure 4.10: Power spectrum of optical transmission taken by an electric spectrum analyzer showing the three lowest radial breathing modes of a microsphere. Insets are corresponding vibration shapes simulated with finite element analysis. From left to right, $(l, m) = (1, 2)$, $(1, 0)$ and $(1, 4)$ modes.

mode shape. We have also observed a mechanical mode splitting in the range of $0.2 \sim 0.4$ MHz for the $(1, 2)$ mode caused by the small deformation and imperfect symmetry.

The size dependence of the mechanical vibration frequencies for the $n = 1$ mode is plotted with diameters ranging in $25 \sim 40$ μm in Fig. 4.11 [52]. The observed mechanical resonance frequency is inversely proportional to the microsphere diameter and agrees very well with the theoretical expectation based on the free sphere model, implying that the effect of the fiber stem is insignificant to the eigenfrequency. The size dependence further confirms that the resonance peaks in the spectrum arise from mechanical vibrations of the microsphere. Note that the modes with odd number of l represented with dashed lines in Fig. 4.11, are not optically observable because these modes do not change the optical path length of the WGMs.

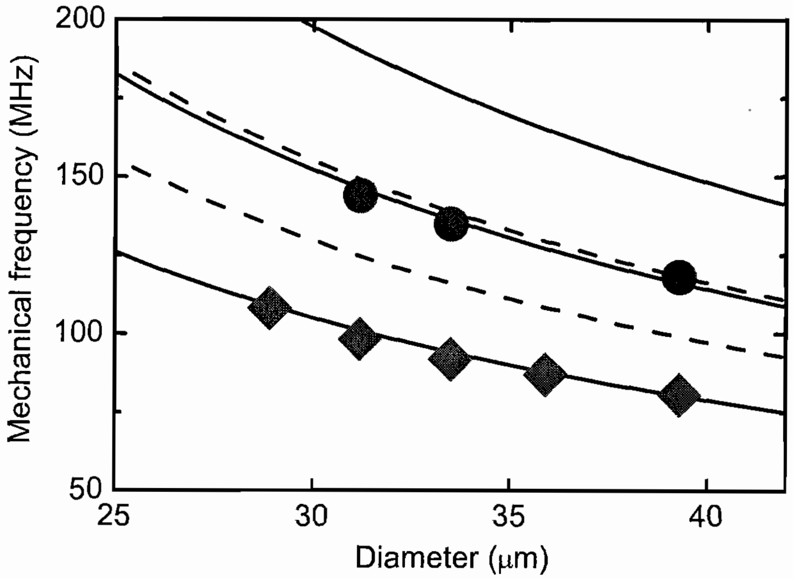

Figure 4.11: Size dependence of Mechanical vibration modes. Mechanical vibration frequencies are plotted as a function of a microsphere diameter. Dots are experimental data and curves are theoretic calculation based on the free sphere model. Mechanical vibrations are observed proportional to the inverse of a diameter. Solid lines present $(n, l) = (1, 2)$, $(1, 0)$ and $(1, 4)$, and dashed lines present $(1, 1)$ and $(1, 3)$ mode, from bottom to top.

In order to verify the homodyne scheme in free-space excitation, we have measured the spectral response of the optical transmission in free-space excitation as shown in Fig. 4.12. For ensuring the complete spatial overlapping between the cavity emission and the local oscillator, a collection lens is placed right after the deformed microsphere to enforce both beams to the same path. An independent test with a single mode optical fiber shows no significant difference in terms of spatial overlapping. Thus, the relative phase between the signal and the local oscillator is totally determined in the microsphere resonator. The DC response is measured with a lock-in detection and the AC response is measured with an electric spectrum analyzer. Figure 4.12(b) shows a cavity linewidth of $\kappa/2\pi = 54$ MHz from a Lorentz fit, and a mechanical frequency is $\omega_m/2\pi = 148$ MHz in a $(1, 0)$ mode. In Fig. 4.12(a),

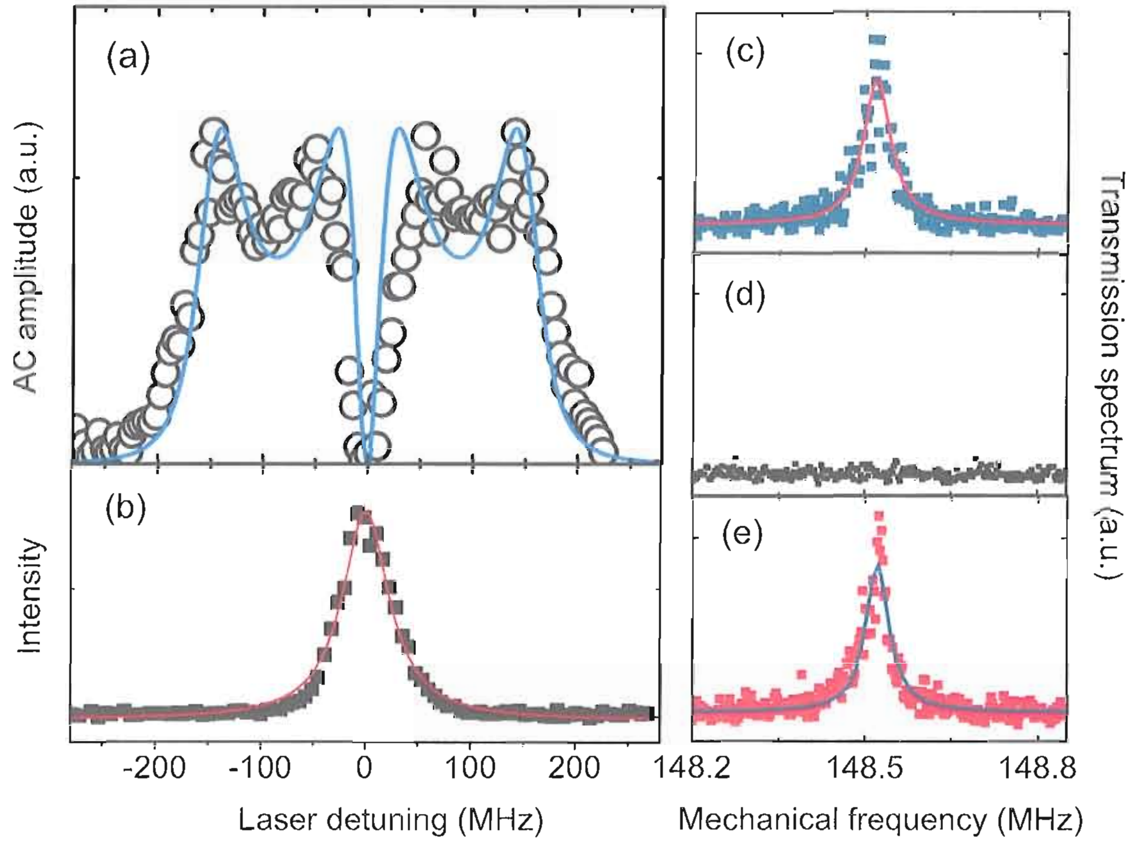

Figure 4.12: Homodyne detection of mechanical displacement in the free-space excitation scheme. (a) The AC part and (b) the DC part of the optical transmission are plotted as a function of laser detuning. Dots are experimental data and a theoretic curve based on the experimental parameters is added for comparison in (a). A curve in (b) is a Lorentz fit of the cavity spectrum. Measured optical spectra are shown for three different laser detunings: (c) $\Delta\omega = -\omega_m$, (d) $\Delta\omega = 0$ and (e) $\Delta\omega = \omega_m$. Mechanical frequency is 148 MHz of a $(1, 0)$ vibration mode and the cavity linewidth is 54 MHz.

the amplitude of the measured optical power spectrum, the AC part, is plotted as a function of laser detuning. The input power was weak so that optomechanical cooling or heating is negligible in this measurement. The observed laser detuning dependence of spectral amplitudes agree very well with theoretic calculation, confirming the homodyne detection scheme in the free-space excitation configuration. Figure 4.12 (c)~(d) show representative optical power spectra measured at $\Delta\omega = -\omega_m$, 0 and $+\omega_m$, respectively. Note that, at zero laser detuning, there is no AC response due to balanced Stokes and anti-Stokes emission. With increasing input power, we have also observed the enhancement in peak amplitude for blue detuning and the suppression for red detuning. This asymmetric response in the AC part indicates the cooling or the heating of the mechanical vibration, depending on laser detuning.

4.2.4 Calibration of Mechanical Vibrations

Interferometric homodyne detection provides a highly sensitive method for the observation of the mechanical displacement spectrum that is embedded in the optical transmission. However, the optical power spectrum may include spectral noises from the experimental environment, such as a laser noise, other than the mechanical vibrations of a microsphere resonator. Thus, proper calibration procedures should be followed by the detection in order to completely recover the mechanical displacement spectrum.

The possible vibration sources other than mechanical vibrations of a silica microsphere in the optomechanical experiment are the mechanical vibrations of an optical table and a ring laser system pumped by a solid-state laser. The former is easily ruled out because of its very slow motion at a rate of few ~ Hz. The mechanical vibrations of laser mirrors mounted in the ring laser are known to range up to a few

MHz. Therefore, we can assume that there is no spectral source in the frequency ranges interested other than the mechanical vibrations of a microsphere.

In measured optical power spectrum, the linewidth and the resonance frequency directly give the damping rate and vibration frequency of the mechanical motion, but the amplitude that results from the transduction process in direct homodyne detection should be properly calibrated to obtain an accurate mechanical vibration amplitude. Even though it is in principle possible to calibrate the peak amplitude of the measured power spectrum by considering the excitation, detection efficiency and all the electrical conversions, it would involve many uncertainties arising from the optical and electrical measurement. One way to calibrate the spectrum amplitude is to use the effective mass obtained from finite element analysis via the equipartition theorem. But, the validity of simulated values should be examined experimentally.

A robust way to calibrate the measured spectrum is to introduce a phase modulation in the excitation laser beam with an electro-optic modulator (EOM). This phase modulation mimics the phase shift induced by the mechanical vibration. With phase modulation, the incident optical field is described by,

$$E_{in} \longrightarrow E_{in}\, e^{i\beta \sin \Omega_{ph} t} \tag{4.18}$$

where β and $\Omega_{ph}/2\pi$ are the depth and the frequency of phase modulation, respectively. The modulation frequency is chosen to be close to the mechanical vibration frequency being observed. The modulation depth β is determined from a separate measurement of the relative intensity distribution of modulated laser taken by an optical spectrum analyzer. With the phase-modulated input laser, following the same steps as direct homodyne detection in free-space excitation scheme discussed in the previous section, the transmission output after the microsphere resonator becomes,

$$\frac{P_{out}}{P_{in}} = \left|\frac{E_{out}}{E_{in}}\right|^2 = \left|e^{i\beta\sin\Omega_{ph}t} - \frac{\eta\kappa}{\kappa/2 - i\Delta\omega} - \eta\kappa I(\Delta\omega;t)\right|^2 \tag{4.19}$$

$$I(\Delta;t) \equiv -\frac{\beta}{2}\left(\frac{e^{-i\Omega_{ph}t}}{\kappa/2 - i(\Delta\omega+\Omega_{ph})} - \frac{e^{i\Omega_{ph}t}}{\kappa/2 - i(\Delta\omega-\Omega_{ph})}\right) \tag{4.20}$$

up to the first order in β. We separate the output power into the DC response and the AC response oscillating at $\Omega_{ph}/2\pi$. The DC part is,

$$P_{out,DC} = P_{in}\left(1 - \frac{4\kappa^2}{\kappa^2+\Delta\omega^2}(\eta-\eta^2)\right) \tag{4.21}$$

This equation, which is independent of Ω_{ph}, is exactly same as Eq.(4.15). On the other hand, the AC part is,

$$\begin{aligned} P_{out,AC} &= -2\eta\kappa\mathrm{Re}\{I\} \\ &\quad - \frac{2\eta\kappa}{(\kappa/2)^2+\Delta\omega^2}\left(-\Delta\omega\sin\Omega t - \frac{\eta\kappa^2}{2}\mathrm{Re}\{I\} + \eta\kappa\Delta\omega\mathrm{Im}\{I\}\right) \end{aligned} \tag{4.22}$$

We can easily check that $P_{out,AC}$ goes to zero at zero detuning $\Delta\omega = 0$ where $\mathrm{Re}\{I\} = \Delta\omega\mathrm{Im}\{I\}=0$. In Fig. 4.13, we plot the AC response at modulation frequency $\Omega/2\pi$ as a function of laser detuning for different ratios of ω_m/κ. Overall behavior of the AC response due to the phase-modulated laser is nearly close to the AC response due to mechanical vibrations of a microsphere. For a large ω_m/κ, a laser detuning $\Delta\omega = \pm\Omega_{ph}$ leads to the resonantly enhanced amplitude of AC response. In the resolved-sideband limit and with $\Delta\omega = \pm\Omega_{ph}$, Eq.(4.22) becomes,

$$P_{out,AC} = 2\eta\beta P_{in}\cos\Omega_{ph}t \tag{4.23}$$

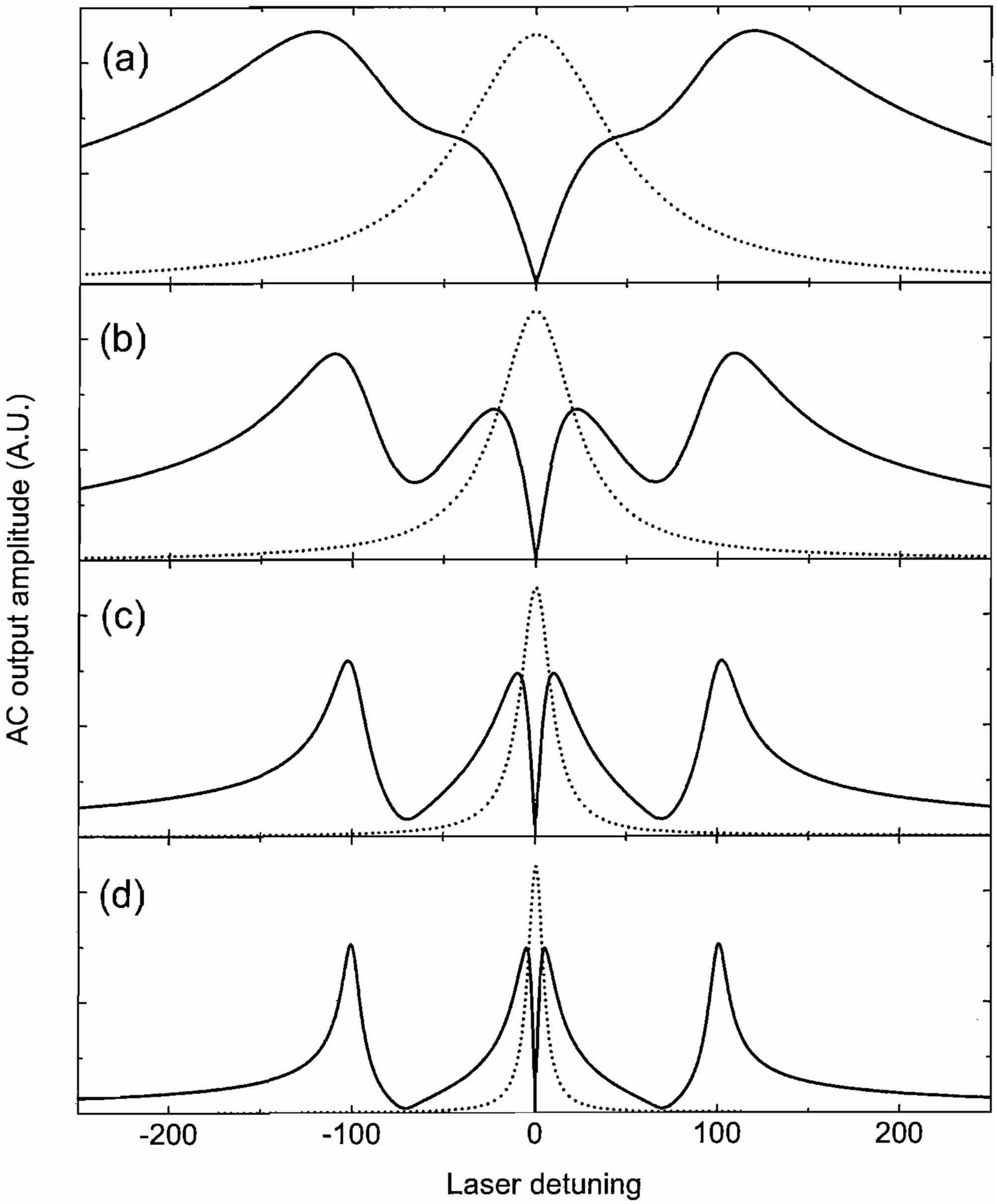

Figure 4.13: Theoretic calculation of AC amplitude normalized to the input power as a function of laser detuning for phase-modulated excitation with $\Omega_m/2\pi = 100$ MHz. Dot lines denotes cavity resonance for different linewidths (a) $\kappa/2\pi = 100$ MHz, (b) $\kappa/2\pi = 50$ MHz, (c) $\kappa/2\pi = 20$ MHz and (d) $\kappa/2\pi = 10$ MHz. Values of $\beta = 0.05$ and $\eta = 0.03$ are used for this calculation.

By comparing Eq.(4.23) to Eq.(4.16), we find that, in the resolved-sideband limit, a mechanical vibration with amplitude r_0 leads to the same signal as a phase modulation with amplitude,

$$\beta = \frac{4\omega_c r_0}{\omega_m R} \tag{4.24}$$

where we have also assumed $\omega_m \approx \Omega_{ph}$ and $\Delta\omega = \pm\omega_m$. The calibration is independent of the cavity decay rate, the mode matching efficiency, and the free-space excitation efficiency. This fact makes the calibration with the phase-modulated input robust as well as convenient. Note that this result is the same as the homodyne detection with $\Delta\omega = 0$ in the Hansch-Couillaud configuration.

Fig. 4.14 shows the noise power spectrum obtained with a phase-modulated excitation laser beam. A resonance due to the phase modulation at $\Omega_{ph}/2\pi$ = 100.9 MHz appears along with the resonance associated with the $(1,2)$ mechanical mode, $\omega_m/2\pi$ = 100.98 MHz. Comparing these two peak amplitudes, we find the vibration amplitude $r_0 = 1.6 \times 10^{-14}\ m$ for the observed $(1,2)$ mechanical mode at room temperature. The y-axis scale in Fig. 4.14 is accordingly calibrated. Using the equipartition theorem, we also determine that the effective mass of the mechanical mode is approximately 41 ng and the corresponding effective mass coefficient is 1.16, which is within 5 % of the theoretical value calculated with finite element analysis.

4.3 Observations of Optomechanical Coupling

4.3.1 Optomechanical Effects on Mechanical Linewidths and Frequencies

As the input power increases, the mechanical vibrations no longer remain the same due to dynamical backaction of the radiation pressure force. The effects of the optical spring and the optomechanical damping are reflected in the effective frequency

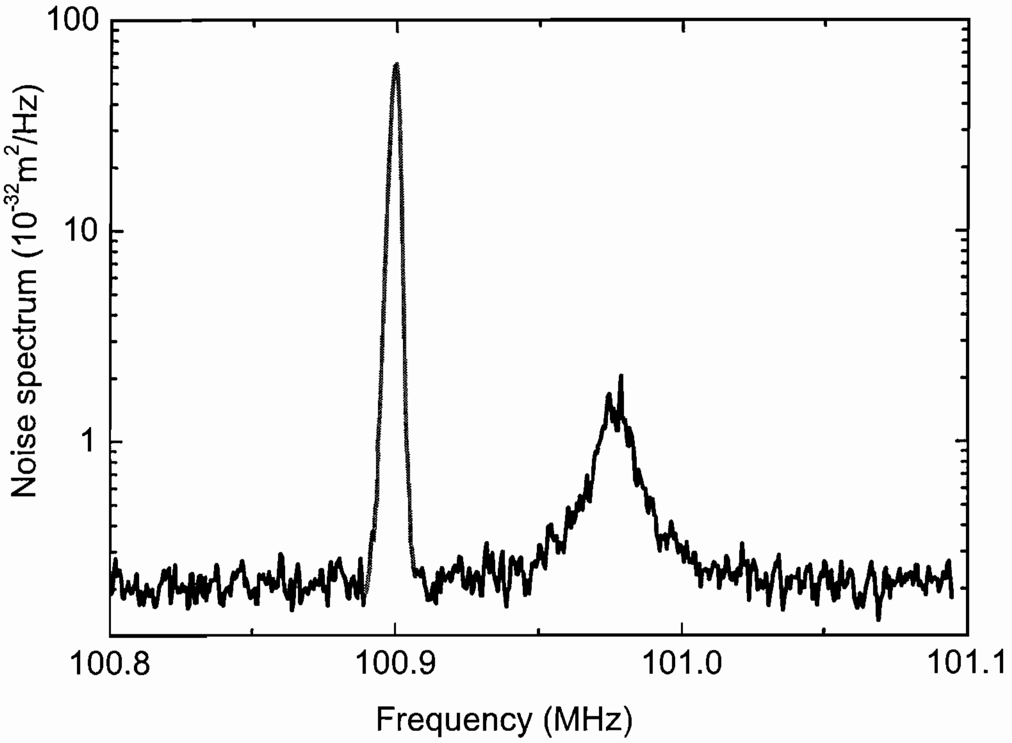

Figure 4.14: Calibration of mechanical displacement with a phase-modulated excitation. Left peak is due to the phase-modulation at 100.9 MHz with a depth $\beta = 0.01$ and right peak at 100.98 MHz is a $(1, 2)$ mechanical vibration mode. Cavity linewidth is 25 MHz and the fractional dip in transmission is ~ 0.05.

and the effective linewidth. Figure 4.15(a) and (b) show the measured power spectra of a $(1, 2)$ mechanical breathing mode obtained for different laser detunings, $\Delta\omega$, with red detuning in Fig. 4.15(a) and with blue detuning in Fig. 4.15(b). An optical pumping power of $0.85P_{th}$ is used where P_{th} is the threshold power for parametric oscillation. For the microsphere used in this measurement, the intrinsic mechanical frequency and linewidth are 87.2 MHz and 7.5 kHz, respectively, and the optical cavity linewidth is 80 MHz. For red detuning, the measured linewidths of power spectra are greater than the intrinsic linewidth, indicating cooling of the vibration motion. In contrast, for blue detuning, the measured linewidths are smaller than the intrinsic linewidth, indicating heating of the mechanical motion. The effective frequency

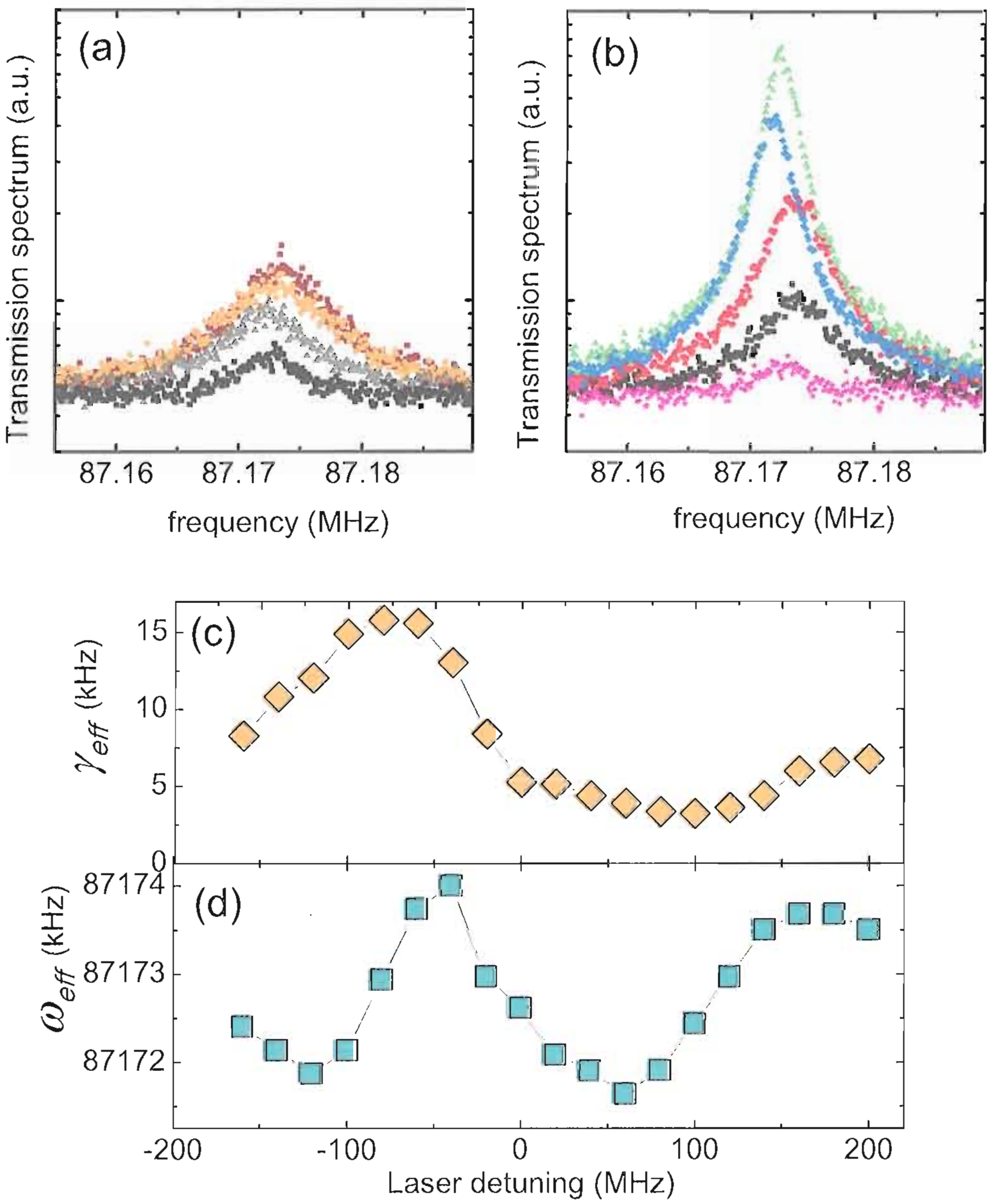

Figure 4.15: Measured optical transmission spectra with red detuning in (a) and blue detuning in (b). In (a), a laser is detuned to $\Delta\omega = -160$ MHz (black), -120 MHz (brown), -80 MHz (yellow) and -40 MHz (gray). In (b), a laser is detuned to $\Delta\omega = 20$ MHz (pink), 60 MHz (blue), 100 MHz (green), 140 MHz (red) and 200 MHz (black). Measured effective mechanical linewidth in (c) and frequency in (d) are plotted as a function of laser detuning. Data are obtained from a Lorenzian fit to observed transmission spectra. The dynamic response of effective linewidth and frequency is the signature of dynamical backaction optomechanical coupling. The cavity linewidth is 80 MHz, and the input power is 0.85 P_{th}.

also changes with laser detuning, which is the signature of the optical spring effect. The amplitudes of the measured spectra are closely related with the measurement sensitivity in the free-space excitation scheme. The observed dynamic response of the effective linewidth and frequency with laser detuning is the manifestation of dynamical backaction optomechanical coupling.

In Fig. 4.15(c) and (d), the effective linewidths γ_{eff} and the effective frequencies ω_{eff} that are obtained from Lorentzian fits to measured spectra are plotted as a function of laser detuning. The cooling and heating of mechanical motion with varying laser detuning are obviously observed from the measured mechanical linewidths. The maximum cooling and heating occur at $\Delta\omega = -\omega_m$ and at $\Delta\omega = +\omega_m$, respectively. ω_{eff} shows a delicate response with laser detuning, crossing the intrinsic frequency at $\Delta\omega = 0, \pm\omega_m$. For large detuning on both sides, γ_{eff} and ω_{eff} converge to each intrinsic value. The unique behavior of γ_{eff} and ω_{eff} agree very well with the theoretical calculation, confirming these effects are caused purely by the radiation pressure force.

We have also measured the input power dependence of the effective linewidth with laser detuning $\Delta\omega = \pm\omega_m$ in Fig. 4.16. While the effective linewidth increases linearly with increasing input power at $\Delta\omega = -\omega_m$, it decreases linearly with $\Delta\omega = +\omega_m$, approaching $\gamma_{eff} = 0$ at the input power for the parametric oscillation. For weak excitation power, the linewidths measured on both sides converge to the intrinsic linewidth of 11 kHz.

4.3.2 Radiation Pressure Induced Parametric Oscillation

With a laser detuned on the blue side of a WGM resonance, the mechanical damping rate decreases due to the optomechanically induced negative damping. With

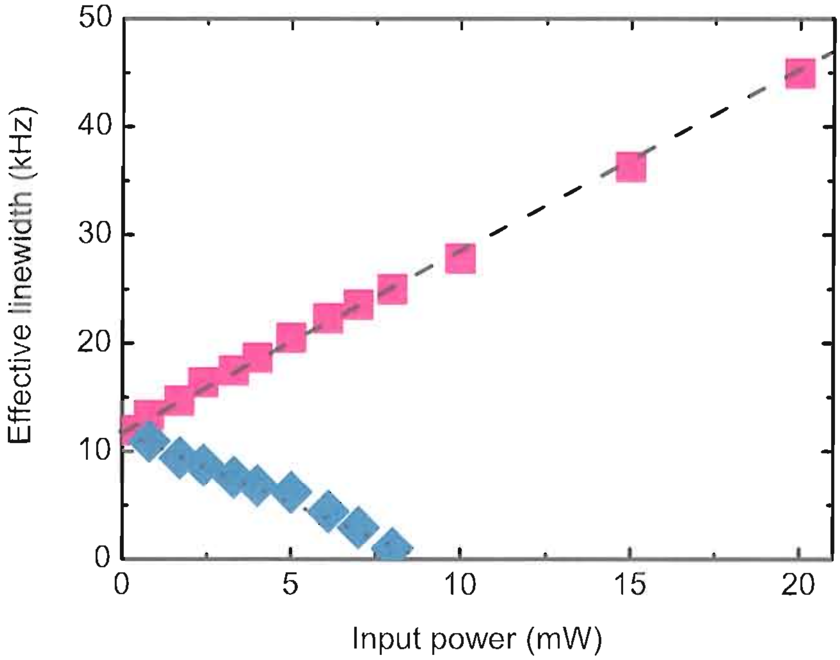

Figure 4.16: Power dependence of measured effective linewidth with $\Delta\omega = -\omega_m$ in red squares and with $\Delta\omega = +\omega_m$ in blue diamonds. Intrinsic mechanical linewidth and frequency are 11 kHz and 116 MHz, respectively, and cavity linewidth is 30 MHz.

increasing input power, the net damping rate can be zero, resulting in the parametric oscillation of the mechanical vibration. Figure 4.17(a) shows the observed power spectrum below and above the threshold power. For this measurement, the mechanical frequency and cavity linewidth are $\omega_m/2\pi = 113$ MHz for the $(1, 2)$ mechanical mode and $\kappa/2\pi = 25$ MHz, respectivley, and the laser is detuned to $\Delta\omega = \omega_m$. Above the threshold power, the enhancement of mechanical vibration shows a signal to noise ratio of more than 40 dB along with a spectral linewidth < 1 kHz. This leads to the strong periodic oscillation in the optical transmission from the WGM with an oscillation period of $(\omega_m/2\pi)^{-1} = 9$ ns, as shown in Fig. 4.17(b). Note that by setting the appropriate amount of laser detuning, parametric oscillations of either the $(1, 0)$ or $(1, 2)$ mode can be selectively realized in a single microsphere.

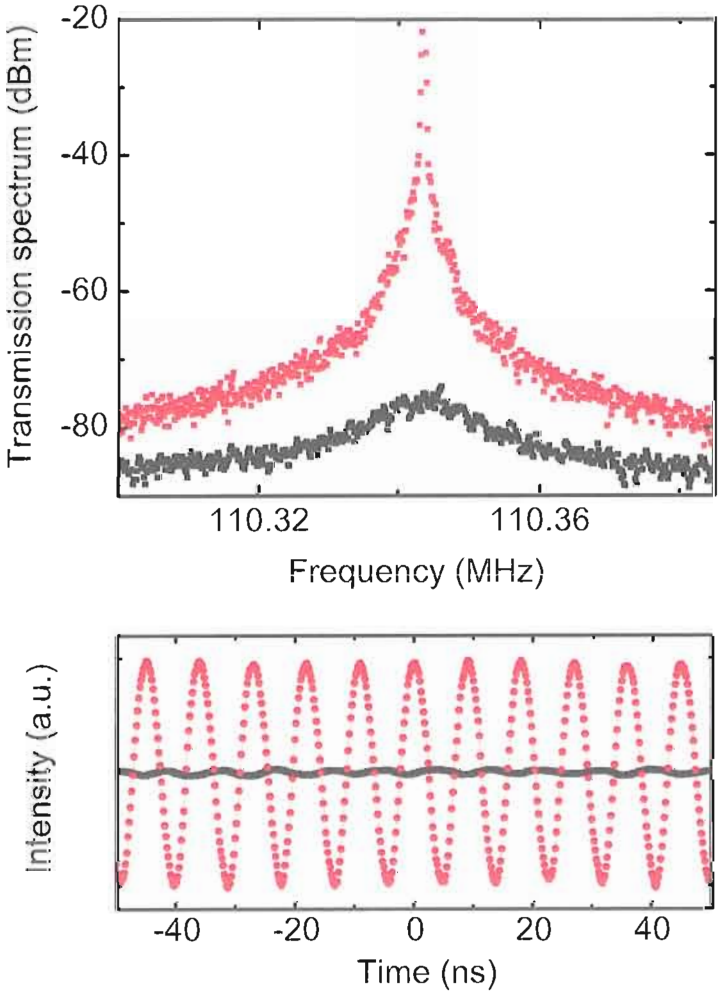

Figure 4.17: Measured parametric oscillation of mechanical vibration denoted with red dots (a) in frequency domain and (b) in time domain. Black dots represent the thermal motion below the threshold power. Significant enhancement in vibration amplitude is observed in the regime of parametric instability.

From theoretical calculations, the threshold power for the parametric oscillation in the resolved-sideband limit has a dependence in the form,

$$P_{th} \propto \frac{R^2}{Q_m \Gamma^2} \tag{4.25}$$

This implies that P_{th} can be further lowered by improving mechanical quality factor with a smaller sized microsphere as well as by increasing WGM excitation efficiency. The result shown in Fig. 4.17 demonstrates that radiation pressure induced mechanical oscillations can be realized with free-space evanescent excitation. The simplicity, the robustness and the relatively high coupling efficiency of the free-space coupling approach should enable explorations and applications of radiation pressure induced optomechanical effects under a variety of environments, for example, for carrying out optomechanical studies in a cryogenic environment for the cooling of a macroscopic mechanical oscillator toward its quantum ground state.

4.4 Mechanical Quality Factors

The mechanical quality factor, Q_m, is defined as,

$$\begin{aligned} Q_m &= 2\pi \frac{\text{total mechanical energy}}{\text{dissipated energy for one cycle}} \qquad (4.26) \\ &= \frac{\omega_m}{\gamma_m} \qquad (4.27) \end{aligned}$$

where ω_m and γ_m are the angular mechanical frequency and intrinsic damping rate that can be measured from the mechanical displacement spectrum. The mechanical quality factor describes how well a mechanical system is isolated from its environment. Q_m-factors or the damping rates depend on the intrinsic material properties as well as on the external factors. The mechanical loss of a silica microsphere-stem system can be decomposed as,

$$\gamma_m = \gamma_G + \gamma_C + \gamma_{TED} + \gamma_{UA} \tag{4.28}$$

where γ_G, γ_C, γ_{TED} and γ_{UA} represent collision loss, clamping loss, thermoelastic loss and ultrasonic attenuation, respectively [73–77]. The mechanical quality factors of deformed microspheres are routinely obtained $\sim 10,000$ or higher for the $(1,2)$ radial breathing mode at room temperature, limited mainly by the clamping loss. Figure 4.18 shows the measured mechanical displacement spectrum, which features $Q_m = 18,000$ for a $(1,2)$ mode in vacuum.

Collision loss [73] is due to random impact by the surrounding gases and usually decreases with decreasing pressure or bath temperature. We normally observe that the spectral linewidth of a mechanical mode of a silica microsphere, which is surrounded by helium gas, is reduced by approximately 2 kHz when the gas pressure decreases below one mTorr from one atmosphere. This difference indicates a collision loss limited mechanical quality factor $Q_m \sim 50,000$. The collision loss contribution to the total damping rate will be further decreased at cryogenic temperature due to the reduced kinetic energy of surrounding gases.

Clamping loss is unavoidable, but can be reduced by carefully designing the resonator-support structure. For example, a LIGO mirror is normally supported at a position of vibration node with a lossless fiber string [73]. In a microsphere-stem system, it is technically difficult to adjust the relative position, but the stem size and length can be controlled to minimize the clamping loss. In fabrication, the diameter of the fiber stem is usually kept $\sim 1/10$ of the microsphere diameter. We believe that the clamping loss in the microsphere-stem system is a dominant factor because the motion of the radial breathing modes is longitudinal with respect to the stem direction in the proximity of the microsphere pole. In order to investigate the effects

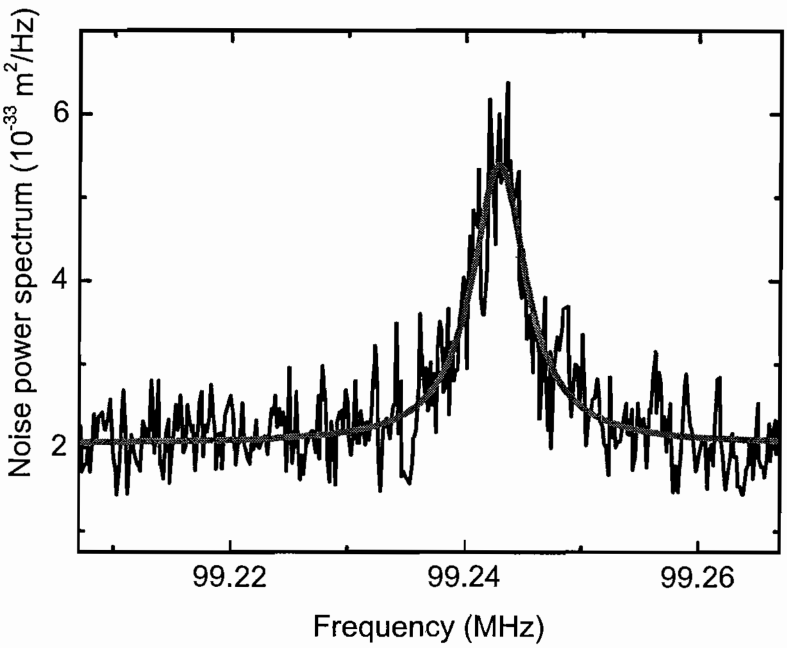

Figure 4.18: Mechanical displacement spectrum of the (1, 2) radial breathing mode measured in vacuum, showing a 5.7 kHz linewidth and the corresponding mechanical quality factor $Q_m = 18,000$ with a vibration frequency 99.24 MHz. The ratio between the microsphere diameter and the stem length is approximately 10.

of the fiber stem, the mechanical quality factors are measured with different stem parameters as shown in Fig. 4.19. In this measurement, the microsphere deformation is kept $\epsilon \sim 2$ %. We find that mechanical quality factors increase with smaller diameter and longer length of the fiber stem. Although the stem diameter and the length separately affect the mechanical quality factor, Fig. 4.19(c) and (d) suggest that these two parameters should be considered together for the better description of the stem effect.

Thermoelastic loss [74] originates from the irreversible heat flow, which is known as a dominant loss mechanism for silicon nanomechanical oscillators. When an object vibrates, while some parts collapse, some parts also expand, resulting in a temperature gradient over the object. Due to the nonuniformity of temperature

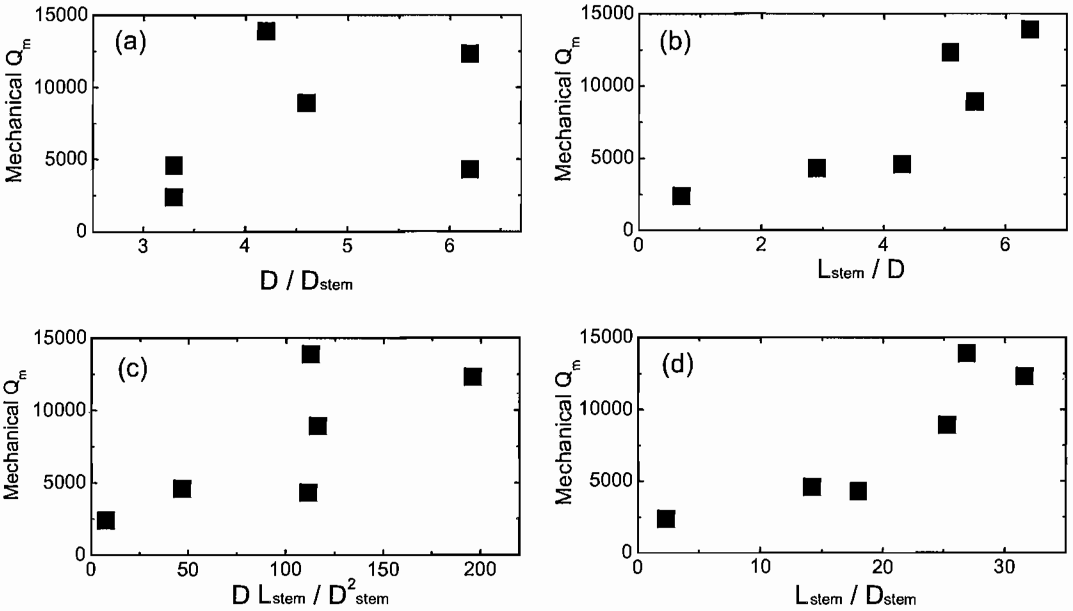

Figure 4.19: The effects of a fiber stem on the mechanical quality factor for a $(1,2)$ radial breathing mode. Measured mechanical quality factors are displayed as a function of (a) D/D$_{stem}$, (b) L$_{stem}$/D, and their combinations in (c) and (d). D$_{stem}$, L$_{stem}$ and D are the diameter and the length of a fiber stem and a microsphere diameter, respectively. Deformation of the microspheres used in this measurement is ~ 2 %.

distribution, a net heat flow occurs across the object, causing mechanical energy dissipation. However, for fused silica possessing a poor thermal conductivity, the thermoelastic loss is negligible because the thermal response time is three orders of magnitude smaller than the mechanical vibration period. The mechanical quality factor limited by thermoelastic loss is estimated to be as high as $Q_m \sim 10^9$ with finite element analysis.

We observe that mechanical quality factors of deformed microspheres also depend on the deformation. Figure 4.20 shows that the mechanical quality factor of the $(1,2)$ radial breathing mode increases rapidly with decreasing deformation. In order to have high Q_m, the deformation needs to be kept below 2 %. However, relatively low Q_m with small deformation, as marked with red circles in Fig. 4.20,

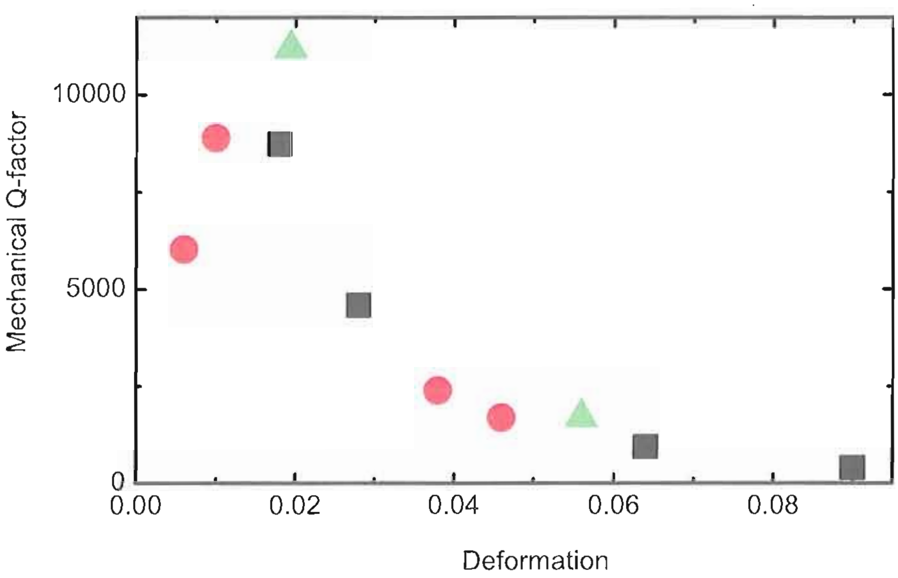

Figure 4.20: Deformation dependence of mechanical quality factors of silica microspheres for the $(1, 2)$ radial breathing mode. Each symbol denotes mechanical Q_m factor measured from the same microsphere with varying deformation. Diameters of deformed microspheres used in this measurement are about 30 μm on average. Values of length-diameter of a fiber stem are 340 μm − 3.8 μm for square, 250 μm − 6.4 μm for circle and 100 μm − 12 μm for triangle. The increase in mechanical quality factors with small deformation can be explained by a small vibration amplitude at the pole of the microsphere.

implies that there is another competing factor, which can one prevent from achieving high mechanical quality factors. The possible explanation of deformation dependence is the increase in vibration amplitude with increasing deformation. Due to the oval-like vibration shape of the $(1, 2)$ mode, a higher vibration amplitude in the equatorial plane accompanies higher amplitude at the microsphere poles, to which the fiber stem is attached. Therefore, the vibration motion with higher deformation causes more stress on the joint between the fiber stem and the microsphere, resulting in more mechanical loss. Systematic control of size and deformation in the deformed microsphere system will provide a better explanation of the deformation induced clamping loss.

4.4.1 Ultrasonic Attenuation in Fused Silica

Ultrasonic attenuation [75] arises from the acoustic damping in an amorphous solid such as silica glass. This effect is negligible at room temperature, but becomes very important below room temperature, playing a crucial role in optomechanical cooling at low temperature. Fig. 4.21(a) shows the temperature dependence of the intrinsic mechanical linewidth $\gamma_m/2\pi$ for the $(1, 2)$ mode from room temperature to 1.4 K. Starting with $\gamma_m/2\pi$ near 10 kHz (corresponding to $Q_m \sim 11,500$) at room temperature, $\gamma_m/2\pi$ increases with decreasing temperature, peaks near a bath temperature of 50 K and then decreases with decreasing temperature with a plateau at temperatures between 10 and 4 K. At $T_{bath} = 1.4$ K, the intrinsic linewidth is approximately 35 kHz and correspondingly Q_m recovers to $3,700$. If we can assume the ultrasonic attenuation is negligible at room temperature, the contribution of the residual acoustic damping at 1.4 K is approximately 25 kHz, which corresponds $Q_m \approx 4,500$, the upper bound limit set by the ultrasonic attenuation. Ultrasonic attenuation depends strongly on the vibration frequency. For the higher the mechanical frequency, the damping rate is larger and the drop-off below 10 K occurs relatively higher temperature.

In an amorphous solid where the molecular structure is irregular rather than periodic, ultrasonic attenuations can occur through thermally activated relaxation processes for $T_{bath} > 10$ K. Below 5 K, interactions of phonons with two-level tunneling defects become important. These behaviors are theoretically explained in the frame of a double-well potential model [78, 79]. In this model, an oxygen atom in a Si-O-Si bond thermally scatters between adjunct potentials, whose barrier and depths are a function of the temperature as illustrated in Fig. 4.21(b). The temperature dependence shown in Fig. 4.21(a) is in good agreement with extensive

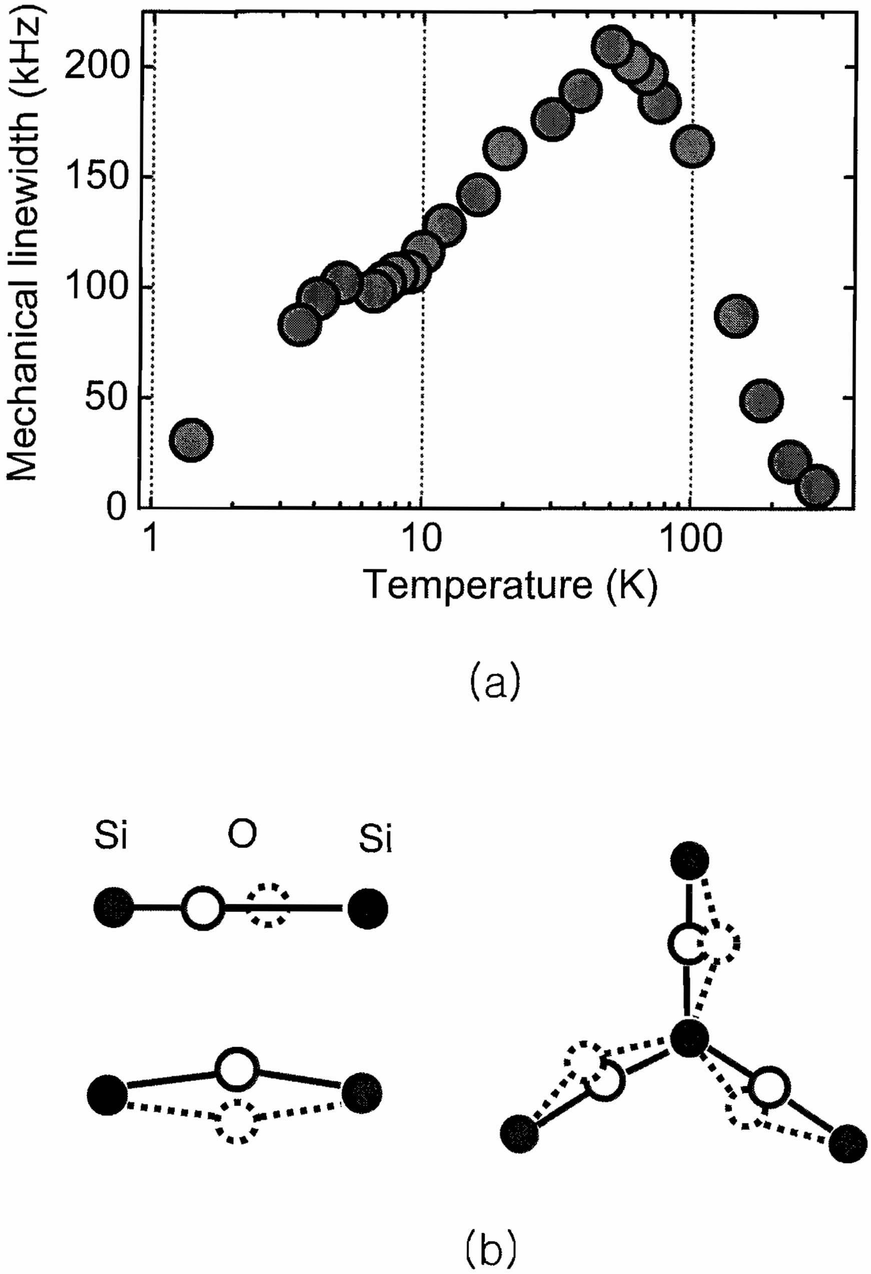

Figure 4.21: (a) Measured mechanical linewidth of a $(1,2)$ vibration mode are plotted as a function of bath temperature. The increase in the intrinsic damping rate below room temperature is attributed to the ultrasonic attenuation in amorphous solids. (b) Illustration of possible Si-O-Si bond configurations. An oxygen atom is placed in a double-well potential in fused silica.

earlier studies, indicating that Q_m should recover to the room-temperature value when the temperature is lowered to a few hundred mK.

CHAPTER V

OPTICAL BISTABILITY OF WGMS AT LOW TEMPERATURE

When the temperature of a silica microsphere changes, a WGM resonance shift is induced by the thermal expansion of the resonator and the thermo-optic effet, i.e. temperature-dependent refractive index. This thermal nonlinearity causes a red-shift of the WGM resonance at room temperature. The optical Kerr effect, the intensity-dependent refractive index, also induces the red-shift, but its magnitude is negligible compared with thermal effect at room temperature.

However, the fact that the thermal expansion coefficient becomes negative below 200 K can lead to the cancelation between thermo-optic effect and the effect of negative thermal expansion [80, 81]. This results in a diminishing optical thermal nonlinearity near 20 K and induces a blue-shift of the WGM resonance with decreasing temperature below 20 K. Interestingly, the much reduced thermal nonlinearity can become comparable in magnitude but opposite in sign with the Kerr nonlinearity. The competition between these two nonlinearities, which are characterized by very different timescales, leads to distinct regenerative pulsation in the transmission of the WGMs excited by a continuous wave laser at low temperature [82]. The characteristic frequency of regenerative pulsation ranges up to only a few MHz, which is far below ultrasonic mechanical vibration of a microsphere.

In this chapter, we will discuss thermal bistability of WGMs both at room and low temperature. We will also present the experimental observation and the theoretical description of the regenerative pulsation at low temperature.

5.1 Thermal Bistability of WGMs in a Silica Microsphere

When a WGM is excited in a microsphere, a part of circulating power is absorbed and thus the microsphere temperature is increased. The thermal absorption not only causes the direct change in the cavity path length due to the thermal expansion, but also changes the thermo-optic effect, the temperature dependence of the refractive index [83]. The thermal effects together with the optical Kerr effect can lead to the shift of the WGM resonance. These optical and thermal effects can be described in a single expression by introducing the effective refractive index, which can be defined as,

$$n_{eff} = n_0 \left[1 + \left(\alpha + \frac{1}{n_0} \frac{dn}{dT} \right) \Delta T + \frac{n_2}{n_0} I \right] \tag{5.1}$$

where n_0 is the refractive index of silica, $\alpha = \frac{1}{R}\frac{dR}{dT}$ is the thermal expansion coefficient, $\frac{dn}{dT}$ is the thermo-optic coefficient [84] and n_2 is an optical Kerr constant. ΔT and I are the temperature change and optical field intensity, respectively. For fused silica with $n_0 = 1.45$, a thermal expansion coefficient $\alpha = 0.55 \times 10^{-6}/\mathrm{K}$ and thermo-optic coefficient $\frac{dn}{dT} = 8.7 \times 10^{-6}$. This yields the thermally induced WGM resonance shift −2.5 GHz/K at room temperature with $\lambda = 800\ nm$. At room temperature, the thermo-optic effect is about one order higher than the effect from thermal expansion and the optical Kerr effect is negligible compared to thermal effects. In Fig. 5.1, a measured WGM spectrum shows a resonance shift as an excitation laser

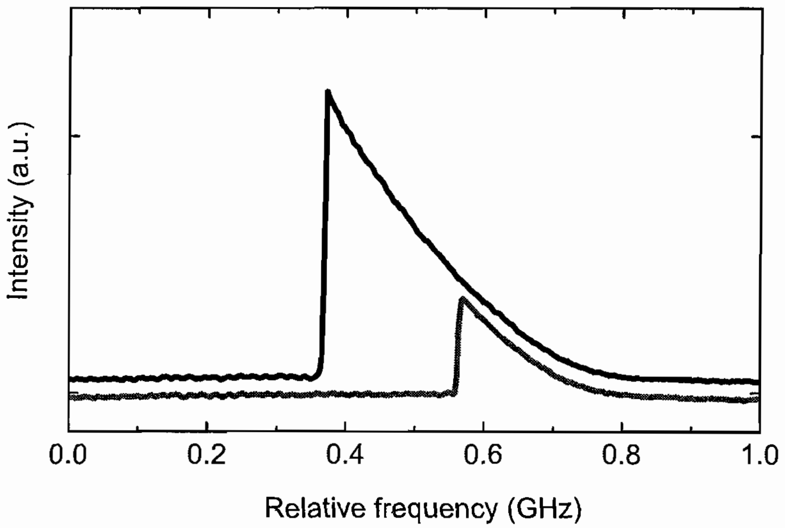

Figure 5.1: Thermal bistability of a WGM resonance at room temperature. The absorbed heat pushes the WGM resonance away when excitation laser is scanned from high to low frequency, resulting an asymmetric spectrum. When scanned from low to high frequency, a WGM resonance is pulled toward laser frequency, resulting in a sudden increase of the intensity in the WGM. The input power of 120 μW in free-space coupling is used, and cavity linewidth with weak excitation is 30 MHz at $\lambda = 800\ nm$.

with relatively a high power is scanned over the WGM resonance. The asymmetric WGM is attributed to the absorption of intracavity power. Scanning the laser from high to low frequency, the absorbed heat pushes the WGM resonance away from excitation laser frequency until it passes the dragged resonance, leaving a sudden quenching of a WGM (Top curve in Fig. 5.1). On the other hand, with scanning the laser from low to high frequency, the absorbed heat pulls the WGM resonance toward the laser frequency, leading to a sudden increase of the intensity (Bottom curve in Fig. 5.1).

WGMs in a microsphere are measured at low temperature through free-space coupling. To overcome the poor thermal conductivity of the fused silica, a cryogenic system with static exchange helium gas in direct contact with the microsphere in the sample chamber is used. Figure 5.2 shows the temperature dependence of the WGM

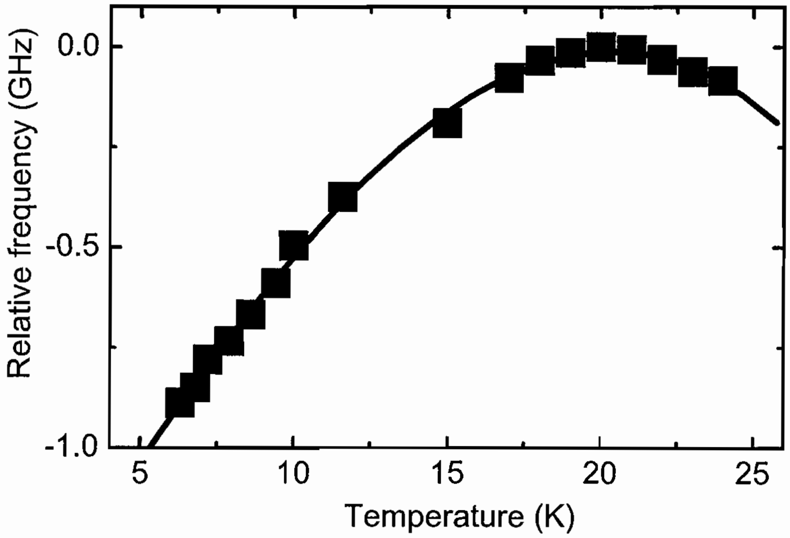

Figure 5.2: Solid squares show the relative frequency of a WGM resonance $\lambda \sim 632\,nm$ as a function of temperature. The solid line is a guide to the eyes. Zero crossing of the slope of the temperature dependence occurs near 20 K. Below 20 K, thermal nonlinearity induces a blue-shift of the WGM resonance oppose to a red-shift at room temperature.

resonance in a temperature range between 5 and 25 K. As shown in Fig. 5.2, the slope of the temperature dependence features a zero crossing near 20 K. Below 20 K, the slope becomes positive and is approximately +0.1 GHz/K at 10 K. In contrast to the red-shift of the WGM resonance due to thermal nonlinearity, the positive slope means that the thermal nonlinearity leads to a blue-shift of the WGM resonance. Note that the positive slope at low temperature will also avoid the optical bistability that hinders or complicates room temperature experiments on radiation pressure cooling of mechanical vibrations.

As shown in an earlier study, $\frac{dn}{dT}$ decreases monotonically but remains positive as the temperature decreases from room temperature to 4 K. However, below 200 K, the thermal expansion coefficient becomes negative. In this case, the red-shift induced by the thermal optical effect can be compensated by the blue-shift induced by the thermal optical expansion. Figure 5.2 indicates that exact cancelation occurs near

20 K. Below 20 K, thermal expansion becomes the leading contribution to temperature dependent frequency shift of the WGM resonance.

5.2 Regenerative Pulsation

Fig. 5.3 shows the WGM transmission as a function of time at 18.5 K. An input laser power of 2 mW and 4.5 mW is used for Fig. 5.3(a) and (b), respectively. For these studies, frequency-stabilized tunable dye laser (Coherent 899-21) with $\lambda \sim$ 632 nm was used. In the weak excitation limit, the spectral linewidth of the WGM resonance is given by $\kappa/2\pi = 30$ MHz, and the fractional dip in the optical transmission through the free-space evanescent excitation is estimated to be 17 %. The pulsation occurs when the continuous-wave single-frequency excitation laser beam is tuned to below the WGM resonance. The top curves in Fig. 5.3 (a) and (b) were obtained with a greater red detuning ($\Delta\omega = -0.7\kappa$) than the bottom curves ($\Delta\omega = -0.3\kappa$), where $\Delta\omega$ is the detuning between laser beam and the WGM resonance in the weak excitation limit.

The temporal behavior of the WGM transmission shown in Fig. 5.3 features highly distinctive regenerative pulsation. The top part of the pulse is inclined. The turn-on and turn-off of the pulse occur in a timescale much faster than the pulsation period. The pulsation period and the duration of the pulse increase with input laser power and decrease with the weak-field detuning between the excitation laser beam and the WGM resonance. The onset of regenerative pulsation takes place at an input excitation laser power of the order of 1 mW. The regenerative pulsation can be observed at temperature between 18 K and 20 K. Note that the stable cavity emissions were obtained when the input power was below the threshold for regenerative pulsation.

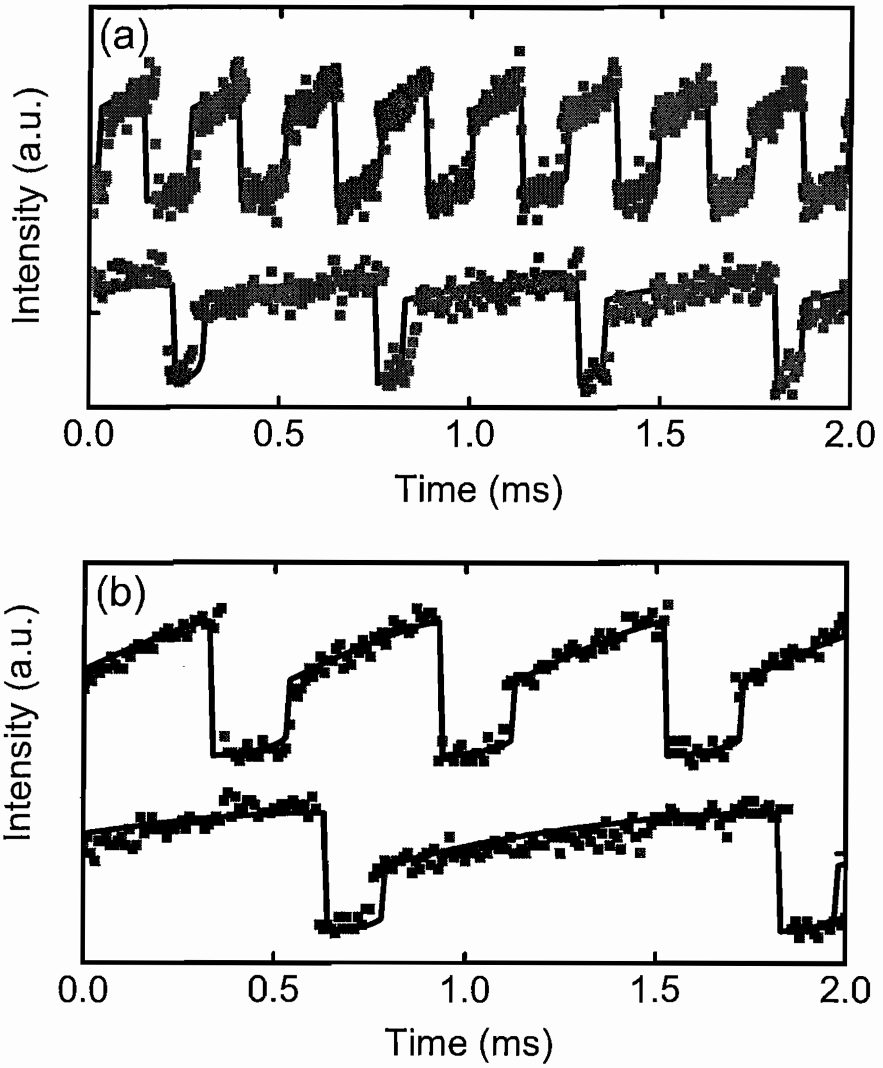

Figure 5.3: Optical transmission as a function of time at $T = 18.5$ K when a WGM is excited by a continuous-wave laser beam. Square dots, experimental data; solid lines, theoretical calculation. The excitation power used is 2 mW for (a) and 4.5 mW for (b). For both (a) and (b), the top and bottom curves were obtained with $\Delta\omega = -0.7\kappa$ and $\Delta\omega = -0.3\kappa$, respectively. For the theoretical calculation, the thermal relaxation rate is used as an adjustable parameter with $\gamma_T = 7.72$ kHz, $\gamma_T = 7.36$ kHz, $\gamma_T = 6.62$ kHz, and $\gamma_T = 6.78$ kHz from the top to bottom curves, respectively.

Distinctive regenerative pulsation similar to those shown in Fig. 5.3 had been observed in earlier studies of optical bistability [85], in which there were two competing nonlinear optical mechanisms with comparable magnitude, opposite sign, but with very different timescales. We attribute the regenerative pulsation in silica microspheres to the competition between the Kerr nonlinearity [86] and the much reduced thermal nonlinearity near 20 K. Due to the optical absorption of silica, excitation of WGMs in a microsphere raises the temperature within the effective mode volume, leading to thermal nonlinearity. The heat generated can be dissipated through the rest of the microsphere and through the surrounding environment with a timescale ranging from a few μs to a few ms [87]. In contrast, the refractive index change induced by the optical Kerr effect follows instantaneously the optical intensity in the cavity mode. At room temperature, the Kerr nonlinearity is two orders of magnitude weaker than the thermal nonlinearity. However, at low temperature, the two nonlinearities can become comparable in magnitude due to the diminishing of the thermal nonlinearity, as we have discussed above.

The regenerative pulsation consists of four dynamic stages. Here we assume that the input laser power is above the threshold for the onset of the regenerative pulsation. As illustrated in Fig. 5.4, when the cavity resonance in slightly above the laser frequency, a redshift induced by the Kerr nonlinearity pulls the cavity resonance toward the laser frequency. The corresponding increase in the intracavity power, $P_{cav}(t)$, leads to an instability, resulting in a rapid rise of $P_{cav}(t)$ and a large redshift of the cavity resonance. At the end of this first stage, the cavity resonance is below the laser frequency. In the second stage, the effect of thermal nonlinearity becomes important. A blueshift induced by the thermal effect slowly pulls the cavity resonance back toward the laser frequency, leading to a further gradual rise of $P_{cav}(t)$. The thermal effect eventually shifts the cavity resonance to above the laser frequency. In

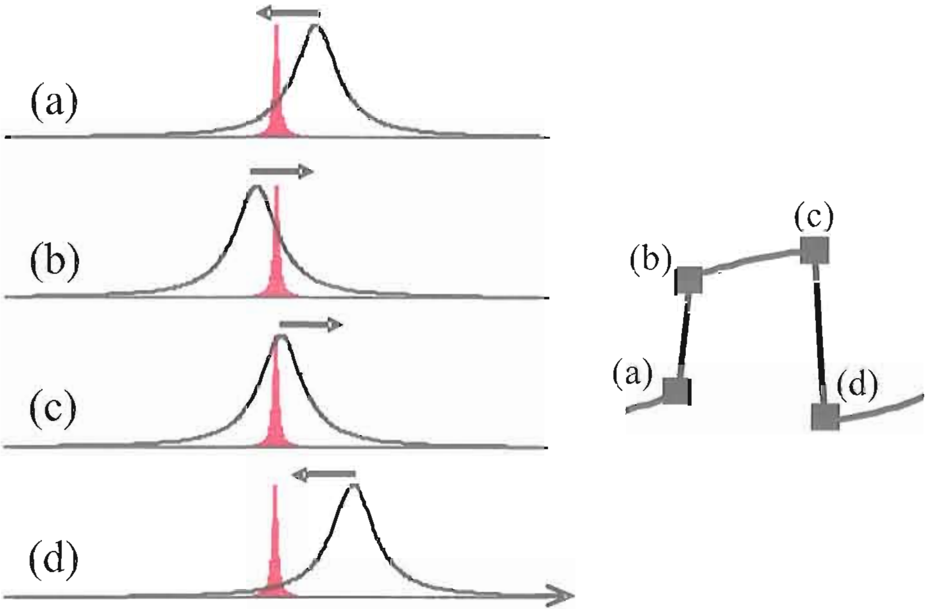

Figure 5.4: Schematic illustrates the shift of the cavity resonance with respect to the laser frequency through the four dynamic stages of regenerated pulsation. On the left side, the peak in red denotes laser detuning and the cavity resonance is described by the black curve.

the third stage, the decrease in $P_{cav}(t)$ and the corresponding reduction in Kerr effects leads to another instability, in which $P_{cav}(t)$ drops rapidly and the cavity resonance shifts further above the laser frequency. In the fourth stage, the resonator cools down and the cavity resonance experience a gradual redshift toward laser freqeuncy. The whole process repeats itself, resulting in the regenerative pulsation.

For a detailed theoretical analysis of the experimental results, we assume that to the first order of $P_{cav}(t)$ and the induced temperature change within the cavity mode volume, $\Delta T(t)$, the cavity resonance frequency, $\omega_c(t)$, can be written as,

$$\omega_c(t) = \omega_c \left[1 - \left(\alpha + \frac{1}{n_0}\frac{dn}{dT}\right)\Delta T(t) - \frac{n_2}{n_0}\frac{P_{cav}(t)}{S}\right] \tag{5.2}$$

where S is the effective cross-sectional area of the relevant WGM. The dynamic equations governing the induced temperature change and the intracavity field are,

$$\begin{aligned}\frac{d\Delta T(t)}{dt} &= -\gamma_T \Delta T(t) + \frac{\alpha_{abs}}{C_p \rho S} P_{cav}(t) & (5.3)\\ \frac{dE_{cav}(t)}{dt} &= -\left(\frac{\kappa}{2} + i\Delta\omega(t)\right) E_{cav}(t) + \frac{it\Gamma E_{in}}{T_{rt}} & (5.4)\end{aligned}$$

where γ_T is the effective thermal relaxation rate, ρ is the mass density of silica, α_{abs} and C_p are the absorption coefficient and the heat capacity of silica, respectively. Γ is a mode-matching coefficient, it is a transmission coefficient to the microsphere deformation, T_{rt} is the cavity round time, E_{in} is the input field, and $\Delta\omega(t) = \omega_L - \omega_c(t)$, with ω_L being the frequency of the external field.

We compare directly in Fig. 5.3 the experimental result and the calculated WGM transmission as a function of time, where we have used $n_0 = 1.45$, $n_2 = 2.5 \times 10^{-16}\ cm^2/W$, $\rho = 2.2\ g/cm^3$, $C_p = 30\ \text{J/kg} \cdot K$ [88], $\alpha = -0.6 \times 10^{-6}/\text{K}$, $\kappa = 2\pi \cdot 30$ MHz, $\Gamma = 0.15$, $\alpha_{abs} = 0.00018\ /m$ at $\lambda = 630\ nm$, and $dn/dT = 0.811 \times 10^{-6}/\text{K}$. We have taken γ_T as an adjustable parameter in the calculation. Figure 5.3 shows a good agreement between theory and experiment, including the dependence of the pulsation on the input power and on the detuning between the cavity resonance and the input laser field. The range of the effective thermal relaxation rates used is also in general agreement with earlier studies. Note that the pulsation frequency decreases with increasing input power, since it takes a longer time for the thermally induced blueshift to compensate the larger redshift induced by the Kerr effect.

While the diminishing of the thermal nonlinearity at low temperature in a silica microresonator is expected to be beneficial for important applications such as cavity QED and radiation pressure cooling, these experimental studies have shown that the competition between Kerr effects and the much reduced thermal effects can lead to the unusual nonlinear optical behavior of regenerative pulsation. For applications of silica microresonators at low temperature, it is important to take into account the regenerative nonlinear optical process.

CHAPTER VI

RESOLVED-SIDEBAND COOLING OF A SILICA MICROSPHERE

Dynamical backaction of a radiation pressure force can lead to the cooling of a microresonator's mechanical vibrations when a laser is detuned to the red side of the cavity resonance. With increasing intracavity intensity, the cooling by the radiation pressure lowers the effective temperature of a mechanical vibration. At the same time the random fluctuation of the radiation pressure force, i.e. the quantum backaction, also increases, leading to the heating of the motion. Thus, the final phonon occupation will be eventually limited by the quantum nature of the cooling light. The ground-state cooling is in principle achievable in the resolved-sideband limit, where the cavity photon lifetime in a microresonator is comparable to, or longer than, the mechanical vibration period. In this regime, with a laser detuning $\Delta\omega = -\omega_m$, the anti-Stokes (cooling process) falling on the cavity resonance is resonantly enhanced, while the Stokes (heating process) falling further away from the cavity resonance is strongly suppressed. The final average phonon occupation is given by $N_Q = \kappa^2/4\omega_m^2 \ll 1$ in the resolved-sideband limit, which is independent of the circulating power.

Although theoretical work predicts that ground-state cooling by the radiation pressure is possible, the phonon occupation achieved thus far still remains more than $1,000$ in optomechanical systems, because the thermal dissipation induced by bath temperature overwhelms the radiation pressure cooling power. Thermal dissipation due to the environment can be considerably reduced by lowering the bath temperature with the use of a cryogenic system. Thus, resolved-sideband cooling together with cryogenic precooling will further reduce the phonon occupation toward the quantum ground state. Technical difficulties involved in implementation and control of a microresonator at low temperature should be overcome in order to realize a cryogenic optomechanical system.

In this chapter, we will discuss experimental studies of the resolved-sideband cooling of a silica microsphere resonator carried out both at room temperature and in a cryogenic environment through the free-space excitation of WGMs. We will also discuss the ultrasonic attenuation of fused silica that limits the obtainable phonon occupation at low temperature.

6.1 Resolved-Sideband Cooling at Room Temperature

We have carried out radiation pressure cooling of a silica microsphere at room temperature in the free-space excitation scheme. The resolved-sideband condition is realized in a deformed microsphere optomechanical system by improving the cavity linewidth to < 30 MHz with a small deformation $\epsilon < 2$ %. The fractional dip in optical transmission is normally measured to be about $5 \sim 10$ %. For the cooling experiment, the excitation laser is dutuned on the redside with $\Delta\omega = -\omega_m$ throughout all experiments. At this detuning, both the optomechanically induced cooling rate and the measurement sensitivity are maximized in the resolved-sideband limit. Figure 6.1(a) shows the measured displacement spectra of a $(1, 2)$ mechanical mode for two different input powers. With a weak excitation of $P_{in} = 0.1\ mW$, the spectrum, the top curve in Fig. 6.1(a) shows the intrinsic linewidth $\gamma_m = 2\pi \cdot$

11 kHz and corresponding mechanical quality factor $Q_m = 11,200$. The measured cavity linewidth and the mechanical vibration frequency are 38 MHz and 115 MHz, respectively, which put this optomechanical microresonator into the resolved-sideband condition with $\omega_m/\kappa = 3.0$. In this condition, the shot noise limited average phonon occupation is $N_Q \simeq 0.07$, which is well below one. With an input power of $P_{in} = 50\ mW$, the effective linewidth is measured $\gamma_{eff} = \gamma_m + \gamma_c = 2\pi \cdot 270$ kHz as shown in the lower curve in Fig. 6.1(a). The linewidth broadening along with the area reduction in the noise spectrum is clearly observed, which is the manifestation of the cooling of the mechanical motion. In this measurement, resolved-sideband cooling leads to the effective temperature of $T_{eff} = 11$ K and the corresponding average phonon occupation of $N_f \simeq 2,000$, approximately 27 times reduction in the thermal energy of the mechanical vibration mode being cooled. The spectra in Fig. 6.1 are calibrated based on the effective mass simulated with finite element method. The spectrum obtained with a higher input power in Fig. 6.1 shows that the measurement sensitivity below $5 \times 10^{-18}\ m/\sqrt{\text{Hz}}$ is achieved.

The effective linewidth is plotted as a function of input excitation power in Fig. 6.1(b) and shows the linear dependence on the input power, as expected from theoretic calculation. Assuming that there is no other heating effects, the corresponding effective temperature determined via the equipartition theorem is also displayed together with effective linewidth. Optomechanically induced cooling ratio can be further increased by improving the quality of the optomechanical system, such as the WGM excitation efficiency and the mechanical quality factor. However, the final phonon occupation achieved at room temperature is mainly limited by the thermal dissipation to the environment. This suggests the necessity of carrying out the cooling experiment at lower bath temperature, combined with a cryogenic precooling.

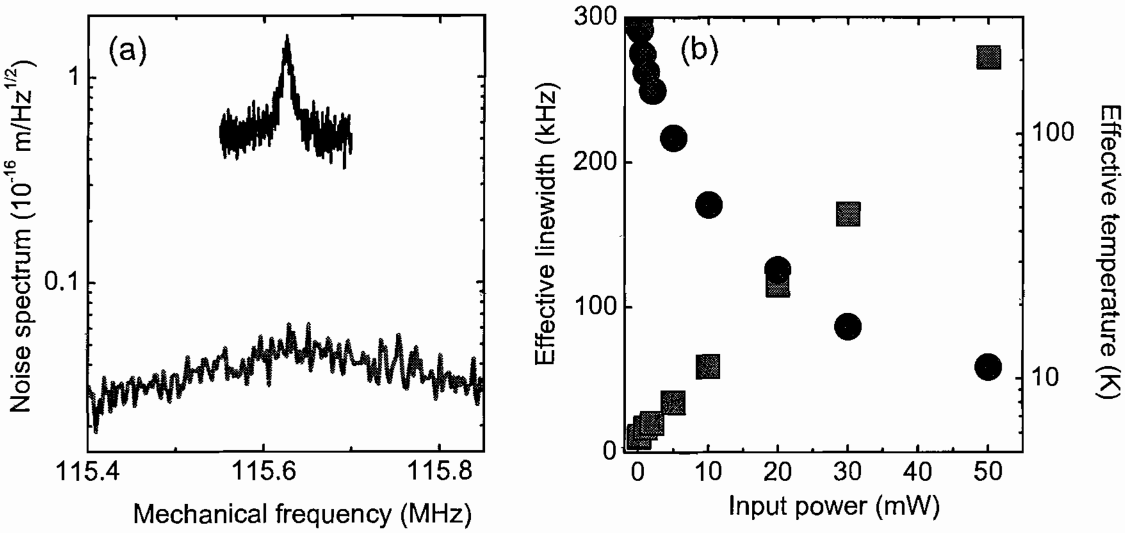

Figure 6.1: Resolved-sideband cooling at room temperature. (a) Measured displacement spectra for two different input powers: $P_{in} = 0.1\ mW$ in black and $P_{in} = 50\ mW$ in green. (b) Measured effective mechanical linewidth and the corresponding effective temperature are plotted as a function of input power. The intrinsic mechanical linewidth $\gamma_m = 2\pi \cdot 11$ kHz and the cavity linewidth $\kappa = 2\pi \cdot 38$ MHz are measured. The final effective temperature $T_{eff} = 11$ K is achieved via the resolved-sideband cooling at room temperature.

6.2 Cryogenic Precooling

For the low temperature experiments, we have been able to combine the optomechanical cooling with the cryogenic cooling through the free-space excitation technique. We have used liquid helium optical cryostats where a microsphere is placed in direct contact with either static exchange helium gas or vapors from a pumped helium reservoir in order to compensate the bad thermal conductivity of silica glass. The relative position change in focused beam between room temperature and low temperature is easily adjusted by precise control of objective lens that is outside cryostat. A 7 mm diameter objective lens with a 5 mm focal length is placed after microsphere to collect the optical transmission. Other experimental setups remain the same as in the room temperature measurement.

Fig. 6.2 shows the temperature dependence of both the vibration frequency $\omega_m/2\pi$ and the mechanical quality factor for the $(1,2)$ mode from room temperature to 1.4 K. Figure 6.2(a) shows a weak temperature dependence < 1 % of mechanical frequency $\omega_m = 2\pi \cdot 115.6$ MHz of a $(1,2)$ vibration mode. The sign reversal in the slope of the temperature dependence reflects a sign change of the thermal expansion coefficient for fused silica near 100 K. The mechanical quality factor strongly depends on the bath temperature. Starting with a mechanical quality factor of $Q_m \sim 11,500$ at room temperature, Q_m decreases with decreasing temperature, reaches minimum near a bath temperature of $T_{bath} = 50$ K, and then increases with decreasing temperature. Q_m recovers to $3,700$, $T_{bath} = 1.4$ K. As explained in Chapter IV, the degradation of Q_m observed below room temperature is attributed to the ultrasonic attenuation in amorphous solid, such as fused silica. The temperature dependence indicates that Q_m should recover to the room-temperature value when the temperature is lowered to a few hundred mK.

In order to make sure that the complete thermalization of a microsphere resonator with the bath temperature, we have measured the displacement spectrum of a mechanical vibration while lowering the bath temperature. The spectrally integrated area of a mechanical resonance in the displacement power spectrum is proportional to the temperature of the mechanical mode. In the limit that temperature dependent variations in the mechanical frequency and the effective mass are negligible, relative changes in the spectrally integrated area provide a direct measure of relative changes in the effective temperature of the mechanical mode. Figure 6.3(b) shows the spectrally integrated area for the $(1,2)$ mode as a function of T_{bath} after subtraction of the shot-noise-limited background. The area is normalized to that obtained at $T_{bath} =$ 150 K. The solid line is the calculated area assuming that the mechanical oscillator is fully in thermal equilibrium with the bath. The integrated area exhibits a linear

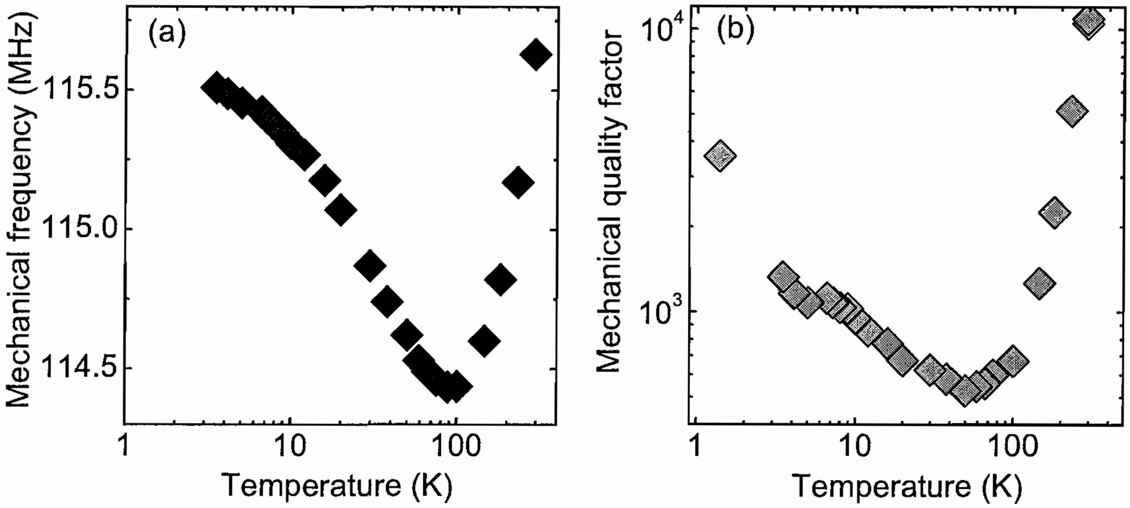

Figure 6.2: (a) Measured mechanical frequency and (b) mechanical quality factor of a $(1,2)$ vibration mode are plotted as a function of bath temperature. Frequency shift is due to the change in thermal expansion coefficient of fused silica, and the bouncing-off near 100 K results from the sign change of thermal expansion of fused silica. The decrease in the mechanical quality factor below room temperature is attributed to the ultrasonic attenuation in amorphous solids.

dependence on T_{bath}, in spite of the strong temperature dependence of Q_m (or $\gamma_m/2\pi$) shown in Fig. 6.2(b), confirming that in the absence of dynamical backaction, the mechanical oscillator is in thermal equilibrium with the bath. During the measurement, no noticeable change in the optical Q-factor and the transmission is observed.

6.3 Resolved-Sideband Cooling at Cryogenic Temperature

We have carried out resolved-sideband cooling on the $(1,2)$ mode at $T_{bath} =$ 3.6 K [44]. A deformed microsphere with $\omega_m/\kappa = 5.4$, $\omega_m/2\pi = 123.4$ MHz, $\gamma_m/2\pi = 12.5$ kHz and $D = 25.5$ μm was prepared at room temperature and cryogenically precooled to 3.6 K, at which point $\gamma_m/2\pi = 80$ kHz. The mechanical quality factor changes from $Q_m \sim 10,000$ at room temperature to $Q_m = 1,540$ at 3.6 K. Figure 6.4(a) shows the displacement power spectrum obtained at various

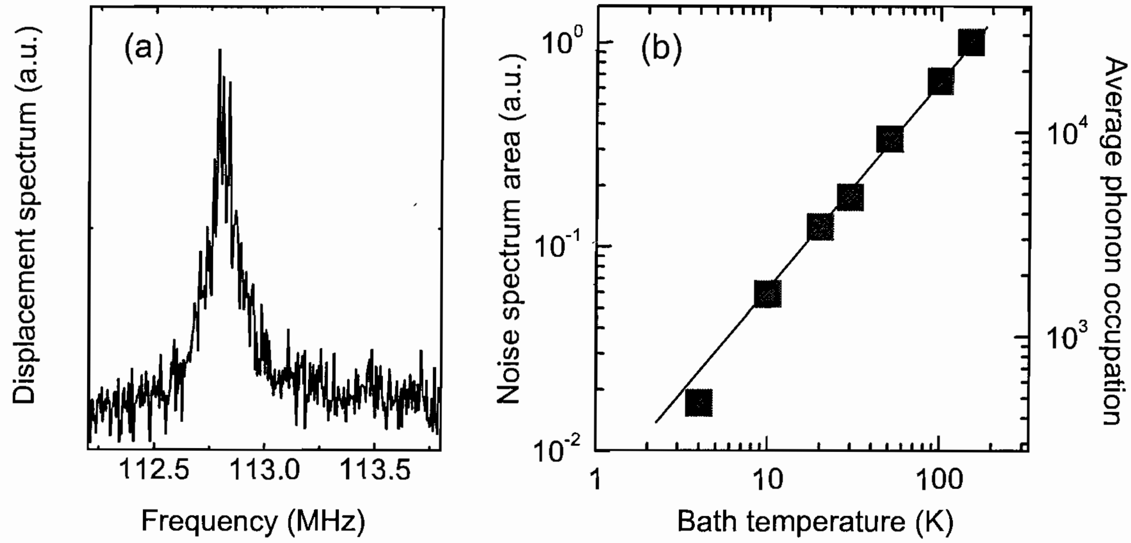

Figure 6.3: (a) Displacement spectrum obtained at $T_{bath} = 20$ K. The spectral area after subtracting shot noise is proportional to the vibration amplitude, which is a measure of vibration mode temperature. (b) Spectrally integrated area is plotted as a function of bath temperature. The linearity ensures that the vibration mode temperature is completely in equilibrium with bath temperature.

incident laser powers with an input laser detuned at $\Delta\omega = -\omega_m$. The spectrally integrated area of the mechanical resonance decreases with increasing laser power, accompanied by an increase in the effective damping rate of the mechanical mode. This behavior of the displacement spectrum is the signature of the radiation pressure cooling of the mechanical vibration. Note that although the incident laser power in these experiments can approach 100 mW, the laser power coupled into the WGM is well below 50 μW owing to the large laser detuning and the small free-space coupling efficiency, which is about a few per cent.

In order to characterize the resolved-sideband cooling process, we plot in Fig. 6.4(b) and (c), the ratio $\gamma_{eff}/\gamma_m = (\gamma_m + \Gamma_c)/\gamma_m$ and the mechanical frequency shift, $\Delta\omega_m/2\pi$, induced by the optomechanical coupling as a function of the laser detuning, $\Delta\omega$. Near $\Delta\omega = -\omega_m$, the mechanical linewidth is maximized while the

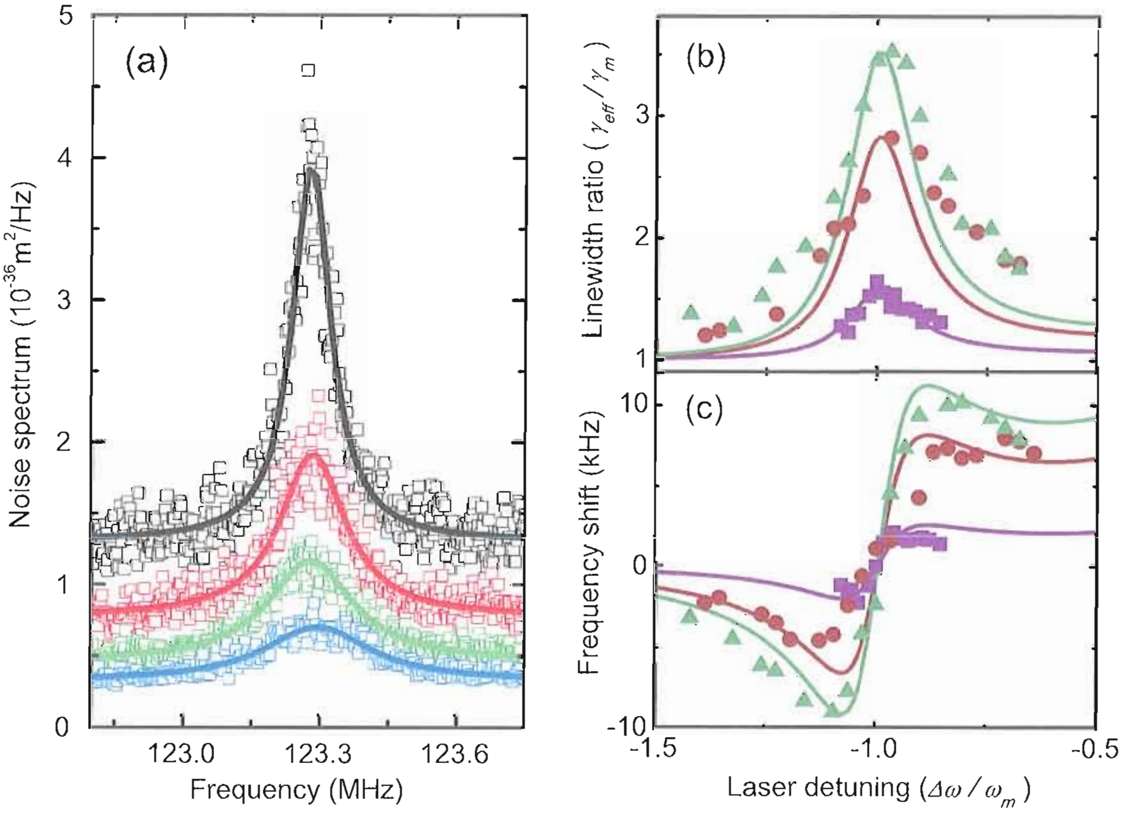

Figure 6.4: Resolved-sideband cooling at cryogenic temperature. Displacement power spectrum obtained at T_{bath} = 3.6 K and $\Delta\omega/\omega_m = -1$. The incident laser power is, from top to bottom, 10 mW, 40 mW, 60 mW and 83 mW, respectively. The solid lines are Lorentzian fits. γ_{eff}/γ_m in (b) and the mechanical frequency shift in (c) induced by optomechanical coupling are plotted as a function of laser detuning obtained at three incident laser powers: 20 mW in blue, 60 mW in purple and 83 mW in olive. The solid lines are the results of the theoretical calculation.

mechanical frequency shift crosses zero. For large laser detuning, both the mechanical linewidth and frequency converge to the intrinsic values determined by the bath temperature. Theoretically, as derived in Chapter III, for resolved-sideband cooling we have,

$$\Gamma_c = \gamma_m \frac{P_{in}}{P_{th}} \frac{4\omega_m^2}{\kappa^2 + 4\Delta\omega^2} \left(\frac{\kappa^2}{\kappa^2 + 4(\Delta\omega + \omega_m)^2} - \frac{\kappa^2}{\kappa^2 + 4(\Delta\omega - \omega_m)^2} \right) \tag{6.1}$$

$$\Delta\omega_m = \frac{P_{in}}{P_{th}} \frac{4\omega_m^2}{\kappa^2 + 4\Delta\omega^2} \left(\frac{\kappa(\Delta\omega + \omega_m)}{\kappa^2 + 4(\Delta\omega + \omega_m)^2} + \frac{\kappa(\Delta\omega - \omega_m)}{\kappa^2 + 4(\Delta\omega - \omega_m)^2} \right) \tag{6.2}$$

where P_{in} is the incident laser power and P_{th} is the threshold incident power for parametric instability when $\Delta\omega = \omega_m$. As shown in Fig. 6.4(b) and (c), the observed Γ_c and $\Delta\omega_m$ are in good agreement with the calculation, for which $P_{th} = 35\ mW$, determined in a separate experiment, is used and there are no adjustable parameters. We have also observed that large deviations between the experiment and calculation occur when the laser is tuned to near the WGM resonance. In this case, heating arising from optical absorption of the circulating light in silica becomes important and optical bistability can also occur. It should be added that at $T_{bath} < 5$ K, no bistability is observed with $\Delta\omega/\omega_m = -1$.

A reliable measure of the effective temperature of a mechanical mode is the spectrally integrated area of the mechanical resonance in the displacement power spectrum. The spectrally integrated area includes contributions from all heating mechanisms, including optical absorption in silica and fluctuations of the laser or the WGM frequency. Figure 6.5 shows the spectrally integrated area, derived from the Lorentzian curve fitting such as those shown in Fig. 6.4(a), as a function of the incident laser power. At $T_{bath} = 3.6$ K and $P = 83\ mW$, radiation-pressure cooling leads to a reduction in the area by a factor of 3.5, indicating $T_{eff} \simeq 1.0$ K and an average final phonon occupation $N_f \simeq 170$. In the limit that optomechanical

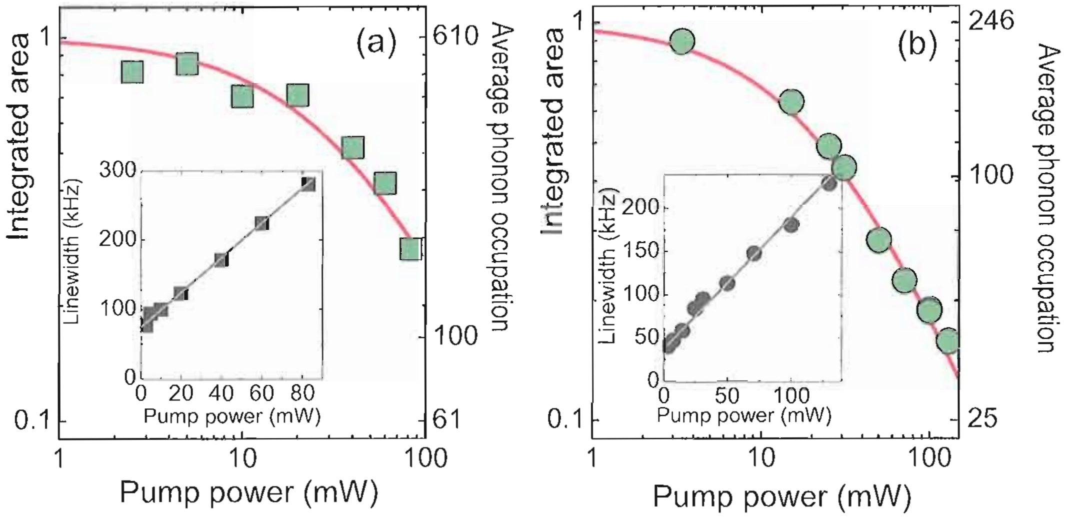

Figure 6.5: Spectrally integrated area of the (1, 2) mode obtained at different bath temperatures from the displacement noise spectrum and the corresponding effective mechanical linewidth in insets as a function of the incident laser power with $\Delta\omega/\omega_m = -1$. The area is normalized to that when the incident laser power approaches zero. The solid curves are the calculated area using the slope of the linear power dependence obtained from the inset.

coupling induces no extra heating, the ratio γ_{eff}/γ_m can also be used to determine the effective temperature, with $T_{eff} = (\gamma_m/\gamma_{eff})T_{bath}$. The inset of Fig. 6.5(a) shows $\gamma_{eff}/2\pi$ as a function of the incident laser power, yielding a maximum cooling rate of $\Gamma_c/2\pi = 200$ kHz. The solid line in Fig. 6.5(a) is the calculated area using the slope obtained from the linear power dependence in the inset of Fig. 6.5(a). The excellent agreement between T_{eff} derived from the spectrally integrated area and that derived from γ_{eff}/γ_m shows that under these experimental conditions, the incident laser beam induces negligible heating.

Resolved-sideband cooling at $T_{bath} = 3.6$ K is limited by the relatively large γ_m due to ultrasonic attenuation in silica, which should diminish at lower temperature. Within the limit of a ^{4}He cryostat, we have carried out resolved-sideband cooling for the (1, 2) mode at $T_{bath} = 1.4$ K. A deformed microshpere with $\omega_m/\kappa = 4.0$,

$\omega_m/2\pi = 118.6$ MHz, $\gamma_m/2\pi = 11.5$ kHz and $D = 26.5$ μm was prepared at room temperature. The mechanical quality factor decreases from $Q_m = 10,000$ at room temperature to $Q_m = 3,400$ at $T_{bath} = 1.4$ K. Figure 6.5(b) and its inset show the spectrally integrated area and the effective mechanical linewidth, derived from the displacement power spectra, as a function of the incident laser power. A maximum cooling rate of $\Gamma_c/2\pi = 195$ kHz, similar to that shown in the inset of Fig. 6.5(a), is obtained. As a result of the smaller γ_m, this cooling rate leads to a reduction of the temperature for the mechanical mode by a factor of 6.6, resulting in the effective temperature of $T_{eff} \sim 210$ mK and the corresponding average phonon occupation of $N_f \simeq 37$ [44]. Figure 6.5(b) also shows the excellent agreement between T_{eff} derived from the spectrally integrated area and that derived from γ_{eff}/γ_m, again indicating that the incident laser beam induces negligible heating.

6.4 Discussion of Cooling Limit

Dynamical backaction cooling in optomechanical systems with high optical finesse is less susceptible to radiation-induced heating than that in electromechanical systems. Although slightly lower average phonon occupation of $N_f \sim 25$ has been achieved in cryogenically cooled electromechanical systems, dynamical back-action cooling in these systems has been limited by heating arising from microwave radiation. Average phonon occupation demonstrated with combined cryogenic and dynamical backaction cooling in electromechanical systems is considerably higher, $N_f \sim 140$ [89]. The direct heating by the laser absorption, which is negligible in our current experimental studies, will become important as more input power is coupled into the microresonator for further cooling. This radiation-induced heating can be suppressed in the optomechanical cooling if working deeply in the resolved-sideband condition with ultrahigh optical quality factors.

Using a deformed silica microsphere, we have demonstrated the resolved-sideband cooling of a silica microsphere optomechanical system in a cryogenic environment and have reached a final average phonon occupation as low as 37 quanta. Although resolved-sideband cooling carried out at $T_{bath} = 1.4$ K is still limited by residual ultrasonic attenuation in silica, no special technical difficulty is anticipated in further lowering the precooling temperature, with a ^{3}He cryostat, to a few hundred mK, at which effects of ultrasonic attention should diminish [75, 90, 91]. The experimental results reported here thus indicate that we are tantalizingly close to realizing the ground-state cooling and reaching the quantum limit of a macroscopic optomechanical system.

CHAPTER VII

SUMMARY AND FUTURE WORK

7.1 Dissertation Summary

This dissertation presents experimental studies of radiation pressure cooling of a silica optomechanical resonator where the optical WGMs are efficiently coupled with the mechanical vibration modes. Optomechanical cooling via radiation pressure can lead to the quantum ground state of a mechanical oscillator, opening the door for exploring the quantum nature of a macroscopic system. Long photon lifetime of WGMs and ultrasonic mechanical vibration in a silica microsphere resonator enable us to carry out optomechanical cooling experiment in the resolved-sideband regime where the average phonon occupation can be well below unity.

We use a slightly deformed microsphere as an optomechanical system. By utilizing directional evanescent escape in deformed microspheres, we are able to evanescently excite the WGMs in free space by focusing a laser beam near microspheres. We demonstrate both high coupling efficiency by showing the optical transmission dip exceeding 50 % and an ultrahigh optical Q-factor up to 1.2×10^8. This unique approach overcomes the technical complexity and difficulty that are normally involved in accessing optical microresonators at low temperature. Through free-space excitation, we are able to launch WGMs in deformed microspheres with no degradation on the

Q factors at a temperature of T = 1.4 K in liquid helium cryogenic system. In terms of optomechanical cooling, cryogenic precooling helps to reduce thermal dissipation determined by the bath temperature.

In the frame work of free-space excitation, we analyze the interferometric homodyne detection of the mechanical displacement both in theory and in experiment. Due to relatively low excitation efficiency, but with ultrahigh Q factors, the part of an input laser which is not coupled into the resonator serves as local oscillator. In homodyne detection, the phase shift induced by mechanical vibration is significantly promoted by the ultrahigh optical finesse in microspheres, resulting in considerable modulation in the optical transmission. We show that the shot noise limited measurement sensitivity yields below 5×10^{-18} $m/\sqrt{Hz}$ with nominal experimental parameters, enabling us to observe thermal mechanical displacement both at room and at low temperature, with high signal-to-noise ratio.

We characterize vibration frequencies and spatial shapes of the mechanical vibrations of a microsphere-stem system with finite element analysis. Resonance frequencies range in an ultrasonic spectral band, above 100 MHz for a 30 μm diameter microsphere. Under direct homodyne scheme, we detect the mechanical vibrations that are imprinted on the optical transmission spectrum. The observed frequencies and their size dependence show excellent agreement with the numerical simulations. Displacement calibration is performed in the same free-space configuration with a phase-modulated excitation laser, which generates a reference spectral peak near the mechanical vibration mode. This method is insensitive to the optical finesse, the coupling efficiency or the noise level, and thus gives an accurate and convenient way of displacement calibration. We show that the effective mass coefficient obtained from the calibration agrees very well with a value simulated by finite element simulation.

We routinely obtain mechanical quality factors above $10,000$ for a $(1,2)$ radial breathing mode at room temperature, which is mainly limited by the clamping loss due to the longitudinal coupling of mechanical vibration to the fiber stem. However, it is well known that at low temperature ultrasonic attenuation in fused silica is dominant source of the mechanical loss. The temperature dependence of the mechanical damping rate reveals that, although the ultrasonic attenuation decreases with decreasing temperature below 50 K, the mechanical quality factors measured at 1.4 K is still limited by residual ultrasonic attenuation and remains about three times smaller than that measured at room temperature.

We study radiation pressure coupling of a silica microsphere first at room temperature in the resolved-sideband regime where a photon lifetime is comparable to or longer than the mechanical vibration period. Again, based on the direct homodyne detection, we measure dynamical behaviors of the effective mechanical frequency and the effective mechanical linewidth as a function of the detuning as well as the intensity of the input laser. For red detuning, we observe the effective linewidth larger than the intrinsic linewidth, implying cooling of mechanical vibration. On the other hand, for blue detuning we observe the effective linewidth smaller than the intrinsic linewidth, implying heating of the mechanical vibration. The experimental observation and the theoretic calculation show excellent agreements, confirming that this response in the displacement spectrum is purely due to the radiation pressure force. Radiation pressure driven parametric oscillation is also demonstrated through free-space coupling within a few mW threshold power, showing the efficient optomechanical coupling in our optomechanical system.

We carry out the resolved-sideband cooling at room temperature and are able to achieve an effective temperature of 11 K for a 118 MHz mechanical vibration of the $(1,2)$ radial breathing mode. This corresponds to average phonon occupation of

$N_f \sim 2,000$, which is mainly limited by the thermal dissipation to the environment held at room temperature.

In the free-space coupling scheme, we are able to combine the resolved-sideband cooling with cryogenic precooling. During precooling, we show the linearity between the spectral area in the displacement spectrum and the bath temperature as predicted from equipartition theorem, indicating perfect thermalization of a microsphere at bath temperature. At a 1.4 K bath temperature, we achieve an average phonon occupation as low as 37 quanta, which is limited mainly by the ultrasonic attenuation in the silica microsphere. We show that both the reduction of the spectral area and the linewidth broadening yield to same cooling ratio, implying no additional heating from the laser noise or the environment. The experimental results achieved by the resolved-sideband and cryogenic cooling indicate that we are tantalizingly close to realizing the ground-state cooling and reaching the quantum limit of a macroscopic optomechanical system.

7.2 Future Work

Resolved-sideband cooling carried out at 1.4 K is still limited by residual ultrasonic attenuation in fused silica, but no special technical difficulty is anticipated in further lowering the precooling temperature, with a ^{3}He cryostat, to a few hundred millikelvin, at which effects of ultrasonic attention should diminish. If we can assume negligible ultrasonic attenuation at 300 mK bath temperature, we expect to achieve an average phonon occupation as low as one through the resolved-sideband cooling, based on achieved optomechanically induced cooling rate Γ_c. Then, we may observe quantum behavior of a macroscopic mechanical oscillator, for example, the transition between classical and quantum mechanics of a macroscopic mechanical oscillator.

Although no significant heating from the experimental environments has been observed in our current work, the heating by the cooling laser absorption could be important in cryogenic operation at sub-Kelvin temperature and restrict the achievable phonon occupation [43]. The heat absorption can be avoided if we work deeply in the resolved-sideband limit with a high ratio of ω_m/κ. Assuming a 4 MHz cavity linewidth achieved in free-space excitation and a 120 MHz mechanical vibration frequency, the fraction coupled into the microresonator will be only 0.03 % of the mode-matched input laser power.

The precooling of mechanical vibration to a sub-Kelvin temperature will reduce the amplitude of the displacement spectrum and simultaneously diminish the ultrasonic attenuation, i.e. recovering the mechanical quality factor, resulting in the linewidth narrowing and accordingly the amplitude enhancement of the displacement spectrum. These two effects on the displacement spectrum of the thermal mechanical vibration will be nearly canceled out as we lower the bath temperature. Thus, we expect that there will be no difficulties in observing thermal mechanical vibration even at 300 mK with the current measurement sensitivity.

In this dissertation, we have demonstrated an optomechanical system where the thermal mechanical vibration is cooled by the radiation pressure force arising from the WGM in a silica microsphere [44]. We have also demonstrated a strong-coupling cavity-QED system where nitrogen vacancy (NV) centers in diamond nanocrystals are coupled to the WGM in a silica microsphere [50]. Both the cavity-QED and the cavity optomechanics can be combined in the single microsphere resonator as shown in Fig. 7.1, opening the opportunities for studying an unexplored field, for example, the coupling between the mechanical vibration of a microsphere resonator and the spin state of NV centers via the WGM.

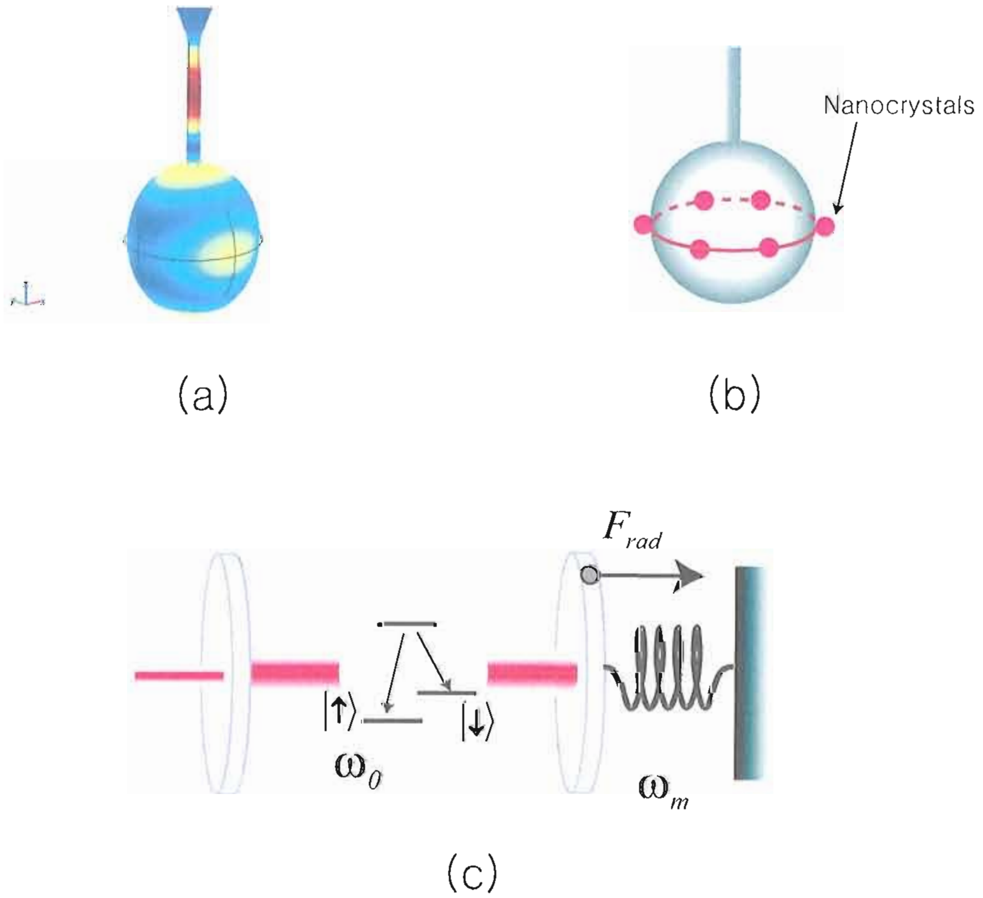
Nanocrystals
F_{rad}
$|\uparrow\rangle$
$|\downarrow\rangle$
ω_0
ω_m

(a) (b) (c)

Figure 7.1: A mechanical oscillation can be coupled to a spin excitation in a combined system of Cavity-QED and cavity optomechanics. (a) A mechanical vibration of a microsphere. (b) Cavity-QED system in a microsphere where nanocrystals are located on the path of the WGM. (c) A schematic of the combined cavity-QED and cavity optomechanics system.

BIBLIOGRAPHY

[1] S. Chu, Rev. Mod. Phys. **70**, 685 (1998).

[2] W. D. Phillips, Rev. Mod. Phys. **70**, 721 (1998).

[3] C. N. Cohen-Tannoudji, Rev. Mod. Phys. **70**, 707 (1998).

[4] D. J. Wineland and H. Dehmelt, Bull. Am. Phys. Soc. **20**, 637 (1975).

[5] T. W. Hansch and A. L. Schawlow, Opt. Commun. **13**, 68 (1975).

[6] D. J. Wineland, R. E. Drullinger, and F. L. Walls, Phys. Rev. Lett. **40**, 1639 (1978).

[7] W. D. Phillips and H. Metcalf, Phys. Rev. Lett. **48**, 596 (1982).

[8] S. Chu, J. E. Bjorkholm, A. Ashkin, and A. Cable, Phys. Rev. Lett. **57**, 314 (1986).

[9] E. L. Raab, M. Prentiss, A. Cable, S. Chu, and D. E. Pritchard, Phys. Rev. Lett. **59**, 2631 (1987).

[10] A. Aspect, E. Arimondo, R. Kaiser, N. Vansteenkiste, and C. Cohen-Tannoudji, Phys. Rev. Lett. **61**, 826 (1988).

[11] P. D. Lett, R. N. Watts, C. I. Westbrook, and W. D. phillips, Phys. Rev. Lett. **61**, 169 (1988).

[12] F. Diedrich, J. C. Bergquist, W. M. Itano, and D. J. Wineland, Phys. Rev. Lett. **62**, 403 (1989).

[13] P. R. Saulson, Phys. Rev. D **42**, 2437 (1990).

[14] A. Gillespie and F. Raab, Phys. Rev. D **52**, 577 (1995).

[15] V. B. Braginsky, S. E. Strigin, and S. P. Vyatchanin, Phys. Lett. A **287**, 331 (2001).

[16] R. Nawrodt, A. Zimmer, S. Nietzsche, M. Thurk, W. Vodel, and P. Seidel, Cryogenics **46**, 718 (2006).

[17] M. D. LaHaye, O. Buu, B. Camarota, and K. C. Schwab, Science **304**, 74 (2004).

[18] W. Marshall, C. Simon, R. Penrose, and D. Bouwmeester, Phys. Rev. Lett. **91**, 130401 (2003).

[19] D. Vitali, S. Gigan, A. Ferreira, H. R. Bohm, P. Tombesi, A. Guerreiro, V. Vedral, A. Zeilinger, and M. Aspelmeyer, Phys. Rev. Lett. **98**, 030405 (2007).

[20] T. J. Kippenberg and K. J. Vahala, Science **321**, 1172 (2008).

[21] I. Favero and K. Karrai, Nature Photon. **3**, 201 (2009).

[22] F. Marquardt and S. M. Girvin, Physics **2**, 40 (2009).

[23] K. C. Schwab and M. L. Roukes, Physics Today **58**, 36 (2005).

[24] A. Naik, O. Buu, M. D. HaHaye, A. D. Armour, A. A. Clerk, M. P. Blencowe, and K. C. Schwab, Nature **443**, 193 (2006).

[25] F. Bondu and J.-Y. Vinet, Phys. Lett. A **198**, 74 (1995).

[26] T. Briant, P.-F. Cohadon, A. Heidmann, and M. Pinard, Phys. Rev. A **68**, 033823 (2003).

[27] A. Schliesser, R. Riviere, G. Anetsberger, O. Arcizet, and T. J. Kippenberg, Nature Phys. **4**, 415 (2008).

[28] F. Marquardt, J. P. Chen, A. A. Clerk, and S. M. Girvin, Phys. Rev. Lett. **99**, 093902 (2007).

[29] I. Wilson-Rae, N. Nooshi, W. Zwerger, and T. J. Kippenberg, Phys. Rev. Lett. **99**, 093901 (2007).

[30] F. Marquardt, A. A. Clerk, and S. M. Girvin, J. Mod. Opt. **55**, 3329 (2008).

[31] P. F. Cohadon, A. Heidmann, and M. Pinard, Phys. Rev. Lett. **83**, 3174 (1999).

[32] C. H. Metzger and K. Karrai, Nature **432**, 1002 (2004).

[33] S. Gigan, H. R. Bohm, and M. Paternostro, Nature **444**, 67 (2006).

[34] O. Arcizet, P.-F. Cohadon, T. Briant, M. Pinard, and A. Heidmann, Nature **444**, 71 (2006).

[35] A. Schliesser, P. DeiHaye, N. Nooshi, K. J. Vahala, and T. J. Kippenberg, Phys. Rev. Lett. **97**, 243905 (2006).

[36] T. Corbitt, Y. Chen, E. Innerhofer, H. Muller-Ebhardt, D. Ottaway, H. Rehbein, D. Sigg, S. Whitcomb, C. Wipf, and N. Mavalvala, Phys. Rev. Lett. **98**, 150802 (2007).

[37] M. Poggio, C. L. Degen, H. J. Mamin, and D. Rugar, Phys. Rev. Lett. **99**, 017201 (2007).

[38] S. Groblacher, S. Gigan, H. R. Bohm, A. Zeilinger, and M. Aspelmeyer, Europhys. Lett. **81**, 54003 (2008).

[39] J. D. Thompson, B. M. Zwickl, A. M. Jayich, F. marquardt, S. M. Girvin, and J. G. E. Harris, Nature **452**, 72 (2008).

[40] K. Srinivasan and O. Painter, Appl. Phys. Lett. **90**, 031114 (2007).

[41] O. Arcizet, P.-F. Cohadon, T. Briant, M. Pinard, A. Heidmann, J.-M. mackowski, C. Michel, L. Pinard, O. Fransais, and L. Rousseau, Phys. Rev. Lett. **97**, 133601 (2006).

[42] S. Groblacher, J. B. Hertzberg, M. R. Vanner, G. D. Cole, S. Gigan, K. C. Schwab, and M. Aspelmeyer, Nature Phys. **5**, 485 (2009).

[43] A. Schliesser, O. Arcizet, R. Riviere, G. Anetsberger, and T. J. Kippenberg, Nature Phys. **5**, 509 (2009).

[44] Y.-S. Park and H. Wang, Nature Phys. **5**, 489 (2009).

[45] R. K. Chang and A. J. Campillo, *Optical Processes in Microcavities* (World Scientific, Singapore, 1996).

[46] G. Mie, Ann. Phys. **25**, 377 (1908).

[47] M. L. Gorodetsky, A. A. Savchenkov, and V. S. Ilchenko, Opt. Lett. **21**, 453 (1996).

[48] V. S. Ilchenko and A. B. Matsko, IEEE Journal of selected topics in quantum electronics **12**, 15 (2006).

[49] J. R. Buck and H. J. Kimble, Phys. Rev. A **67**, 033806 (2003).

[50] Y.-S. Park, A. K. Cook, and H. Wang, Nano Lett. **6**, 2075 (2006).

[51] B. Min, T. J. Kippenberg, and K. J. Vahala, Opt. Lett. **28**, 1507 (2003).

[52] Y.-S. Park and H. Wang, Opt. Express **15**, 16471 (2007).

[53] B. V. Braginsky, M. L. Gorodetsky, and V. S. Ilchenko, Phys. Lett. A **137**, 393 (1989).

[54] H. Lamb, Proc. London Math. Soc. **13**, 189 (1882).

[55] N. Nishiguchi and T. Sakuma, Solid State Commun. **38**, 1073 (1981).

[56] M. H. Kuok, H. S. Lim, S. C. Ng, N. N. Liu, and Z. K. Wang, Phys. Rev. Lett. **90**, 255502 (2003).

[57] T. J. Kippenberg, H. Rokhsari, T. Carmon, A. Scherer, and K. J. Vahala, Phys. Rev. Lett. **95**, 033901 (2005).

[58] B. S. Sheard, M. B. Gray, C. M. Mow-Lowry, and D. E. McClelland, Phys. Rev. A **69**, 051801 (2004).

[59] C. Genes, D. Vitali, P. Tombesi, S. Gigan, and M. Aspelmeyer, Phys. Lett. A **77**, 033804 (2008).

[60] R. Kubo, Rep. Prog. Phys. **29**, 255 (1966).

[61] T. Carmon, H. Rokhsari, L. Yang, T. J. Kippenberg, and K. J. Vahala, Phys. Rev. Lett. **94**, 223902 (2005).

[62] M. L. Gorodetsky and V. S. Ilchenko, J. Opt. Soc. Am. B **16**, 147 (1999).

[63] M. Hossein-Zadeh, H. Rokhsari, A. Hajimiri, and K. J. Vahala, Phys. Rev. A **74**, 023813 (2006).

[64] S. Mancini and P. Tombesi, Phys. Rev. A **49**, 4055 (1994).

[65] C. K. Law, Phys. Rev. A **51**, 2537 (1995).

[66] S. Lacey and H. Wang, Opt. Lett. **26**, 1943 (2001).

[67] S. Lacey, H. Wang, D. H. Foster, and J. U. Nockel, Phys. Rev. Lett. **91**, 033902 (2003).

[68] Y.-F. Xiao, C.-H. Dong, Z.-F. Han, G.-C. Guo, and Y.-S. Park, Opt. Lett. **32**, 644 (2007).

[69] Y. Hadjar, P. F. Cohadon, C. G. Aminoff, M. Pinard, and A. Heidmann, Europhys. Lett. **47**, 545 (1999).

[70] J. C. Knight, G. Cheung, F. Jacques, and T. A. Birks, Opt. Lett. **22**, 1129 (1997).

[71] M. Cai, O. Painter, and K. J. Vahala, Phys. Rev. Lett. **85**, 74 (2000).

[72] L. Collot, V. Lefevre-Seguin, M. Brune, J. M. Raimond, and S. Haroche, Europhys. Lett. **23**, 327 (1993).

[73] G. Cagnoli, L. Gammaitoni, J. Hough, J. Kovalik, S. McIntosh, M. Punturo, and S. Rowan, Phys. Rev. Lett. **85**, 2442 (2000).

[74] R. Lifshitz and M. L. Roukes, Phys. Rev. B **61**, 5600 (2000).

[75] R. Vacher, E. Courtens, and M. Foret, Phys. Rev. B **72**, 214205 (2005).

[76] K. Numata, K. Yamamoto, H. Ishimoto, S. Otsuka, K. Kawabe, M. Ando, and K. Tsubono, Phys. Lett. A **327**, 263 (2004).

[77] P. Mohanty, D. A. Harrington, K. L. Ekinci, Y. T. Yang, M. J. Murphy, and M. L. Roukes, Phys. Rev. B **66**, 085416 (2002).

[78] W. A. Phillips, Rep. Prog. Phys. **50**, 1657 (1987).

[79] R. Keil, G. Kasper, and S. Hunklinger, J. Non-Cryst. Sol. **164**, 1183 (1993).

[80] G. K. White, J. Phys. D **6**, 2070 (1973).

[81] G. K. White, Phys. Rev. Lett. **34**, 204 (1975).

[82] Y.-S. Park and H. Wang, Opt. Lett. **32**, 3104 (2007).

[83] V. S. Ilchenko and M. L. Gorodetskii, Laser Physics **2**, 1004 (1992).

[84] T. Toyoda and M. Yabe, J. Phys. D **16**, L97 (1983).

[85] J. L. Jewell, H. M. Gibbs, S. S. Tarng, A. C. Gossard, and W. Wiegmann, Appl. Phys. Lett. **40**, 291 (1982).

[86] F. Treussart, V. S. Ilchenko, J.-F. Roch, J. Hare, V. Lefevre-Seguin, J.-M. Raimond, and S. Haroche, Eur. Phys. J. D **1**, 235 (1998).

[87] T. Carmon, L. Yang, and K. J. Vahala, Opt. Express **12**, 4742 (2004).

[88] R. C. Zeller and R. O. Pohl, Phys. Rev. B **4**, 2029 (1971).

[89] J. D. Tuefel, J. W. Harlow, C. A. Regal, and K. W. Lehnert, Phys. Rev. Lett. **101**, 197203 (2008).

[90] O. L. Anderson and H. E. Bommel, J. Am. Ceram. Soc. **38**, 125 (1955).

[91] R. O. Pohl, X. Liu, and E. Thompson, Rev. Mod. Phys. **74**, 991 (2002).